

Science and Technology of Nuclear Installations

In-Vessel and Ex-Vessel Corium Stabilization in Light Water Reactor

Lead Guest Editor: Hwan Yeol Kim

Guest Editors: Sevostian Bechta, Jerzy Foit, and Seong Wan Hong





In-Vessel and Ex-Vessel Corium Stabilization in Light Water Reactor

Science and Technology of Nuclear Installations

In-Vessel and Ex-Vessel Corium Stabilization in Light Water Reactor

Lead Guest Editor: Hwan Yeol Kim

Guest Editors: Sevostian Bechta, Jerzy Foit, and Seong Wan Hong



Copyright © 2018 Hindawi. All rights reserved.

This is a special issue published in “Science and Technology of Nuclear Installations.” All articles are open access articles distributed under the Creative Commons Attribution License, which permits unrestricted use, distribution, and reproduction in any medium, provided the original work is properly cited.

Editorial Board

Nusret Aksan, Switzerland
Won Pil Baek, Republic of Korea
Stephen M. Bajorek, USA
George Bakos, Greece
Leon Cizelj, Slovenia
Alejandro Clausse, Argentina
Francesco D' Auria, Italy
Mark Deinert, USA
Cesare Frepoli, USA
Michel Giot, Belgium
Valerio Giusti, Italy

Tim Haste, France
Keith E. Holbert, USA
Tomasz Kozlowski, USA
Tomoaki Kunugi, Japan
H.-Y. Lee, Republic of Korea
Jiri Macek, Czech Republic
Borut Mavko, Slovenia
Oleg Melikhov, Russia
Rafa Miró, Spain
Michael I. Ojovan, UK
Domenico Paladino, Switzerland

Manmohan Pandey, India
Luca Podofillini, Switzerland
Carlo Sborchia, France
Arkady Serikov, Germany
James F. Stubbins, USA
Iztok Tiselj, Slovenia
Rizwan Uddin, USA
Eugenijus Ušpuras, Lithuania
Hidemasa Yamano, Japan
Enrico Zio, Italy
Massimo Zucchetti, Italy

Contents

In-Vessel and Ex-Vessel Corium Stabilization in Light Water Reactor

Hwan Yeol Kim , Sevostian Bechta, Jerzy Foit, and Seong Wan Hong
Editorial (3 pages), Article ID 3918150, Volume 2018 (2018)

Effect of Subcooling on Pool Boiling of Water from Sintered Copper Microporous Coating at Different Orientations

Seongchul Jun , Jinsub Kim, Seung M. You, and Hwan Yeol Kim
Research Article (9 pages), Article ID 8623985, Volume 2018 (2018)

A Conceptual Approach to Eliminate Bypass Release of Fission Products by In-Containment Relief Valve under SGTR Accident

Taeseok Kim , Wonjun Choi , Joongoo Jeon , Nam Kyung Kim , Hoichul Jung, and Sung Joong Kim 
Research Article (12 pages), Article ID 5936214, Volume 2018 (2018)

Modelling of Severe Accident and In-Vessel Melt Retention Possibilities in BWR Type Reactor

Mindaugas Valinčius , Tadas Kaliatka , Algirdas Kaliatka, and Eugenijus Ušpuras 
Research Article (14 pages), Article ID 7162387, Volume 2018 (2018)

Effect of Molten Corium Behavior Uncertainty on the Severe Accident Progress

Wonjun Choi , Taeseok Kim, Joongoo Jeon , Nam Kyung Kim , and Sung Joong Kim 
Research Article (9 pages), Article ID 5706409, Volume 2018 (2018)

Analysis of Steam Explosion under Conditions of Partially Flooded Cavity and Submerged Reactor Vessel

Sang Ho Kim , Seong-Wan Hong, and Rae-Joon Park
Research Article (12 pages), Article ID 3106039, Volume 2018 (2018)

Editorial

In-Vessel and Ex-Vessel Corium Stabilization in Light Water Reactor

Hwan Yeol Kim ¹, Sevostian Bechta,² Jerzy Foit,³ and Seong Wan Hong¹

¹Korea Atomic Energy Research Institute, Daedeok-daero 989-III, Yuseong-gu, Daejeon, Republic of Korea

²Kungliga Tekniska Högskolan, 10044 Stockholm, Sweden

³Karlsruhe Institute of Technology, P.O. Box 3640, 76021 Karlsruhe, Germany

Correspondence should be addressed to Hwan Yeol Kim; hykim1@kaeri.re.kr

Received 3 September 2018; Accepted 3 September 2018; Published 2 October 2018

Copyright © 2018 Hwan Yeol Kim et al. This is an open access article distributed under the Creative Commons Attribution License, which permits unrestricted use, distribution, and reproduction in any medium, provided the original work is properly cited.

Since the Fukushima accidents, severe accident mitigation as a last protective barrier of nuclear disasters is of a great concern for the public acceptance. A lot of efforts have been made to resolve the severe accident mitigation issues during the several decades. Corium stabilization inside and outside the reactor vessel, one of the issues with a great progress, is a key to securing the safety of Light Water Reactors from the point of view of severe accident mitigation and containment integrity.

Regarding the corium stabilization inside reactor vessel, a concept of IVMR (In-Vessel Melt Retention) is generally used for the Light Water Reactors as a most effective method. The IVMR relies on cooling of the outside surface of the reactor lower vessel by naturally circulating water so-called ERVC (External Reactor Vessel Cooling). In the ERVC, cooling water is supplied to the exterior wall of the reactor vessel in case of severe accident. This strategy was firstly used in the VVER-440 reactor and now it is adopted for a number of higher power reactor designs such as AP1000 and APRI400. For the assessment of successful IVMR, it is important how to accurately estimate the thermal heat load inside the reactor vessel and the heat removal rate outside the reactor vessel. There are several issues for the estimation: corium relocation to lower head, lower head debris bed behaviour, lower head molten pool behaviour, thermal and mechanical loadings and behaviour of structures including the lower head, and external vessel cooling rate.

If the IVMR is not maintained, failure of the reactor lower head starts as the final stage of the in-vessel accident

progression. The initial situation is characterized by a molten corium pool in the lower head. Important parameters for the assessment of lower head failure are temperature distribution of vessel wall, internal pressure, dead weight of the vessel wall and the melt pool, thermochemical attack of the corium, and mechanical behaviour of reactor vessel. If it will fail, the location and time of failure have to be evaluated. For the PWRs, ICI (In-Core-Instrumentation) penetration tubes at the reactor lower head are regarded as the most vulnerable parts. BWRs include several venerable parts such as CRGT (Control Rod Guide Tubes), ICMGT (In-Core Monitoring Guide Tubes), and drainage tubes.

Regarding the corium stabilization outside reactor vessel, there are two preferred methods used for the operating Light Water Reactors: pouring water on top of the melt pool which is discharged from the failed vessel into the normally dry cavity and discharging melt into the wet cavity which is flooded with water before the arrival of the melt. The melt should be cooled down lower than the concrete ablation temperature in order to avoid erosion of concrete leading to basemat melt-through and containment failure by generation of gases from concrete ablation. This is caused by so-called MCCI (Molten Core Concrete Interaction). Melt-water interaction is relatively small for the former method, because an insulating crust is formed all around the melt pool after the initial contact with water. For the latter method, the oxidic-ceramic melt breaks into melt particles of small sizes, which results in increase of the contacting surface area between the original melt and the water. This can lead to a steam explosion.

For the advanced reactor, a concept of core catcher is employed to cope with the corium stabilization outside reactor vessel. Ex-vessel melt is retained and cooled in the core catcher. The core catcher is currently installed for EPR and VVER-1000.

The paper “Effect of Subcooling on Pool Boiling of Water from Sintered Copper Microporous Coating at Different Orientations” presents experimental results of a subcooling effect on pool boiling heat transfer using a copper microporous coating water a comparison with those of a plain surface. A HTCMC (High-temperature Thermally Conductive Microporous Coating) was made by sintering copper powder. The nucleate boiling heat transfer did not change much with the degree of subcooling for both the HTCMC and the plain surface. However, the CHF (Critical Heat Flux) linearly increased with the similar rates of 60 kW/m^2 per degree for both surfaces, so the CHF values of the HTCMC stayed about $\sim 1,000 \text{ kW/m}^2$ higher than those of the plain surface throughout the subcooling. The results showed a possibility of using the microporous coating at an outer reactor vessel wall to enhance cooling performance and CHF when in-vessel retention through external reactor vessel wall (IVR-ERVC) strategy is applied as a severe accident mitigation methodology.

The paper “Analysis of Steam Explosion under Conditions of Partially Flooded Cavity and Submerged Reactor Vessel” presents the effects of the free-fall of corium on a steam explosion by benchmarking previous experimental cases. Two premixing experiments presenting partially flooded cavity conditions and submerged-RV conditions in the TROI (Test for Real Corium Interaction with water) facility were modelled by the TEXAS-V code. The impulse of a steam explosion under the condition of a corium jet falling into water without a free-fall height is bigger than that under a free-fall height. Larger fragmented mass of corium in an explosion phase and smaller steam production under the condition of no free-fall height resulted in bigger impulse of steam explosion. The distribution of void fractions was similar in both the experiments and simulations. The effect of a large bubble around a melt jet is an important element to be simulated well.

The paper “Effect of Molten Corium Behavior Uncertainty on the Severe Accident Progress” presents results of an uncertainty and sensitivity analysis of a severe accident progress in a Korean Optimized Power Reactor 1000 MWe (OPR1000) using the MELCOR integrated severe accident code. Uncertainty of severe accident progression phenomena, namely, the time of melt relocation, the time of lower plenum dryout, and the time of the reactor pressure vessel and containment failure in MELCOR simulations, induced by 5 selected uncertainty input parameters has been investigated. In addition, a sensitivity analysis applying a rank regression technique has been performed in order to identify those uncertain parameters, which mainly contribute to the uncertainty of the selected MELCOR results. The results of rank regression analysis showed that 2 out of 5 selected uncertain parameters, i.e., the zircaloy melt breakout temperature and molten clad drainage rate, have the largest contribution to

the uncertainty of the time of melt relocation and the time of lower plenum dryout in the MELCOR results.

The paper “A Conceptual Approach to Eliminate Bypass Release of Fission Products by In-Containment Relief Valve under SGTR Accident” presents the conceptual design of the ICRV (In-Containment Relief Valve) as effective means to mitigate the release to the environment of fission products from the SGTR (Steam Generator Tube Rupture) accident. To show the effectiveness of ICRV concept, the simulation of OPR1000 by using MELCOR code was carried out. It was assumed that the steam of the secondary system was released to the upper dome of the containment and the RDT (Ractor Drain Tank) using ICRV. The results show that the radioactive nuclides were not released to the environment even though the containment pressure increases up to 1.2 MPa. To minimize the negative effects of pressurization of the containment, the steam release by the ICRV linked to the RDT and cavity flooding was also simulated. Because the overpressurization of containment is due to heat of ex-vessel corium, it turned out that cavity flooding was effective for depressurization. Finally, authors made a conclusion that the conceptual design of the ICRV is effective to mitigate the SGTR accident.

The paper “Modelling of Severe Accident and In-Vessel Melt Retention Possibilities in BWR Type Reactor” deals with application of in-vessel melt retention, which is in use as a milestone of SAM strategy in several PWR and VVER reactors, in a BWR-5 reactor having quite different design of the lower head, in particular, a forest of control rod and instrumentation penetrations. A computer code RELAP/SCDAPSIM MOD 3.4 and a full plant model of a ~ 2000 MW thermal power BWR reactor were used to model a large break Loss of Coolant Accident (LOCA) in which total failure of cooling water injection was postulated. A full accident sequence, up to corium relocation into the lower head and molten pool formation, is calculated with a particular attention to vessel external cooling by water. In the last part, different ex-vessel heat transfer models were used and compared, and it was concluded that the implemented heat transfer correlations of the COUPLE module are more accurate than that of the RELAP5 based module. As the used code does not take into account stratified molten pool with the top metal layer, the analytical study was conducted to estimate possible focusing effect in the location of top metal layer. The results show that at prototypic corium masses and volumetric heat in the RPV lower head a significant amount of steel should be in the molten pool in order to keep the heat fluxes on the external vessel surface below CHF (1.06 MW/m^2). It was concluded that detailed evaluation of the steel mass relocated to the lower head during severe accident is not possible with the existing RELAP/SCDAPSIM models, which are recommended to be further developed in order to evaluate complex phenomena in the debris bed and to model heat and mass transfer within a molten pool having 2 or 3 immiscible layers.

The main purpose of this special issue is to provide high quality articles containing latest research achievements on in-vessel and ex-vessel corium stabilization in Light Water Reactors. We believe that interesting information on this topic will be supplied to the readers.

Conflicts of Interest

The authors declare that there are no conflicts of interest regarding the publication of this paper.

Acknowledgments

We would like to express gratitude to all those who helped us during organizing this special issue and also express sincere gratitude to the reviewers for their valuable reviews.

Hwan Yeol Kim

Sevostian Bechta

Jerzy Foit

Seong Wan Hong

Research Article

Effect of Subcooling on Pool Boiling of Water from Sintered Copper Microporous Coating at Different Orientations

Seongchul Jun ¹, Jinsub Kim,¹ Seung M. You,¹ and Hwan Yeol Kim²

¹Department of Mechanical Engineering, The University of Texas at Dallas, 800 W. Campbell Rd. Richardson, TX 75080, USA

²Korea Atomic Energy Research Institute (KAERI), Severe Accident & PHWR Safety Division, 989-111 Daedeok-Daero, Yuseong-Gu, Daejeon, Republic of Korea

Correspondence should be addressed to Seongchul Jun; seongchj@gmail.com

Received 22 March 2018; Revised 29 June 2018; Accepted 22 July 2018; Published 13 August 2018

Academic Editor: Iztok Tiselj

Copyright © 2018 Seongchul Jun et al. This is an open access article distributed under the Creative Commons Attribution License, which permits unrestricted use, distribution, and reproduction in any medium, provided the original work is properly cited.

The subcooling effect on pool boiling heat transfer using a copper microporous coating was experimentally studied in water for subcoolings of 10 K, 20 K, and 30 K at atmospheric pressure and compared to that of a plain copper surface. A high-temperature thermally conductive microporous coating (HTCMC) was made by sintering copper powder with an average particle size of 67 μm onto a 1 cm \times 1 cm plain copper surface with a coating thickness of $\sim 300 \mu\text{m}$. The HTCMC surface showed a two times higher critical heat flux (CHF), $\sim 2,000 \text{ kW/m}^2$, and up to seven times higher nucleate boiling heat transfer (NBHT) coefficient, $\sim 350 \text{ kW/m}^2\text{K}$, when compared with a plain copper surface at saturation. The results of the subcooling effect on pool boiling showed that the NBHT of both the HTCMC and the plain copper surface did not change much with subcooling. On the other hand, the CHF increased linearly with the degree of subcooling for both the HTCMC and the plain copper surface. The increase in the CHF was measured to be $\sim 60 \text{ kW/m}^2$ for every degree of subcooling for both the HTCMC and the plain surface, so that the difference of the CHF between the HTCMC and the plain copper surface was maintained at $\sim 1,000 \text{ kW/m}^2$ throughout the tested subcooling range. The CHFs for the HTCMC and the plain copper surface at 30 K subcooling were $3,820 \text{ kW/m}^2$ and $2,820 \text{ kW/m}^2$, respectively. The experimental results were compared with existing CHF correlations and appeared to match well with Zuber's formula for the plain surface. The combined effect of subcooling and orientation of the HTCMC on pool boiling heat transfer was studied as well.

1. Introduction

Subcooled boiling is an effective heat transfer mode that utilizes both single-phase and two-phase heat transfer for the cooling of high heat flux devices. One example is the cooling of an external reactor vessel wall by subcooled water when a severe accident occurs at a nuclear power plant from a natural disaster or malfunction. To protect the reactor vessel, the external reactor vessel wall must be cooled by a coolant. Heat transferred to the coolant must be maintained below the critical heat flux (CHF), which is the maximum heat flux before transitioning to the film boiling heat transfer. Others applications include high heat flux electronic chip cooling for electronic devices.

Many researchers have investigated the subcooling effect on boiling heat transfer, and some correlations have been developed for the subcooling effect on the CHF. Kutateladze

[1] was one of the earliest researchers who investigated the subcooling effect. He postulated that the CHF was reached when vapor film being generated between the heater wall and the liquid as well as the increase in the CHF at the subcooling was due to the necessity of supplying an additional amount of heat to warm the subcooled liquid around a heated surface to saturation. Then, he formulated a CHF correlation between subcooling ($q''_{\text{CHF,sub}}$) and saturation ($q''_{\text{CHF,sat}}$), starting from heat balance and dimensional analysis as

$$\frac{q''_{\text{CHF,sub}}}{q''_{\text{CHF,sat}}} = 1 + C \left(\frac{\rho_l}{\rho_v} \right)^n \frac{c_{pl}}{L_{lv}} (T_{\text{sat}} - T_1) \quad (1)$$

where C is an empirical constant, ρ_l and ρ_v are liquid and vapor density, respectively, c_{pl} is the specific heat of liquid, L_{lv} is the latent heat of vaporization, and $(T_{\text{sat}} - T_1)$ is the temperature difference between saturation (T_{sat}) and

bulk liquid temperature (T_1). The properties are based on the saturation temperatures. Next, he obtained the constant $C=0.065$ and $n=0.8$ in (1) from the experimental results of Kutateladze and Schneiderman [2] for water (1–3 atm), alcohol (1–10 atm), and isooctane (1 atm).

Ivey and Morris [3] created a correlation based on the vapor-liquid exchange mechanism developed by Engelburg-Forster and Grief [4] and Kutateladze's CHF formula (see (1)) and found the constant $C=0.1$ and $n=0.75$ in (1) by matching the experimental results of Kutateladze and Schneiderman [2]. Ivey and Morris [5] further investigated the effects of subcooling on stainless steel and Zircaloy-2 with a different diameter and wall thickness of test heaters by experiment. From their experimental results, they concluded that the CHF of subcooled boiling has a negligible difference for heater diameter and thicknesses as well as the materials for subcooling of 10–70 K.

Zuber et al. [6] developed a CHF correlation for subcooling without curve fitting with experimental results, but by postulating that additional heat flux is transferred to the subcooled liquid in addition to the same hydrodynamic crisis at saturation. The additional heat flux for the subcooled liquid to heat up to the saturation was expressed as a one-dimensional diffusion equation:

$$q'' = \frac{2k_l (T_{\text{sat}} - T_1)}{\sqrt{\pi\alpha\tau}} \quad (2)$$

where α is the thermal diffusivity and τ is the residence time that represents bubble cycle time.

The CHF for subcooled conditions is then expressed as

$$q''_{\text{CHF,sub}} = 0.131L_{lv}\rho_v \left[\frac{\sigma g (\rho_l - \rho_v)}{\rho_v^2} \right]^{1/4} + \frac{2k_l (T_{\text{sat}} - T_1)}{\sqrt{\pi\alpha\tau}} \quad (3)$$

The first term on the right hand side of (3) is the CHF at saturation, and the second term is the additional heat flux caused by subcooling. After rearranging (3) and finding τ , it can be written as the form of CHF ratio between saturation and subcooling:

$$\frac{q''_{\text{CHF,sub}}}{q''_{\text{CHF,sat}}} = 1 + 5.32 \frac{(k_l \rho_l c_{pl})^{1/2}}{\rho_v L_{lv}} \left[\frac{\rho_v^2 g (\rho_l - \rho_v)}{\sigma^3} \right]^{1/8} (T_{\text{sat}} - T_1) \quad (4)$$

where k_l is the thermal conductivity of the liquid, g is the gravitational acceleration, and σ is the surface tension. It can be seen from (4) that the CHF increases proportionally with subcooling. This correlation showed good agreement with the experimental results done by Kutateladze and Schneiderman [2] for water and ethyl alcohol. Many other correlations of the CHF between subcooling and saturation have been developed

so far, but the aforementioned three correlations are the most well-known ones, especially for water, and the current experimental results are compared with them and discussed in Section 3.

Later subcooling effects on pool boiling heat transfer of dielectric liquids were studied as a cooling method for electronics as well [7–9]. Hwang and Moran [7] conducted a subcooling experiment of FC-86 on a vertical 4.57 mm square silicon chip in the range of 2–82 K and compared it with Ivey and Morris's [3] correlation to find that the value of the constant in the correlation was $C=0.05$ and $n=0.75$, which was half of the original Ivey and Morris correlation [3]. Mudawar and Anderson [8] studied the subcooling effects of FC-72 with a subcooling of 0–35 K on a vertical 12.7 mm \times 12.7 mm flat surface and found the coefficient to be $C=0.064$ and $n=0.75$. Watwe et al. [9] investigated the subcooling effects of FC-72 on a horizontal 10 mm \times 10 mm silicon chip and found the constant to be $C=0.03$ and $n=0.75$ by curve fitting with their experimental data. Those subcooling data of dielectric liquids showed lower coefficients ($C=0.03$ – 0.065) compared to water, which was 0.1 in the Ivey and Morris correlation [3].

Rainey et al. [10, 11] investigated the subcooling effects of a plain 10 mm \times 10 mm flat copper surface in FC-72 and compared them with an ABM (aluminum particles, Devcon Brushable Ceramic epoxy, and methyl ethyl ketone) coating with a coating thickness of $\sim 50 \mu\text{m}$ at a subcooling temperature of 0–50 K. They found that nucleate boiling heat transfer was closely maintained regardless of subcooling. They observed that the CHF of the ABM coating increased at a higher rate than that of the plain copper surface as the subcooling increased. Parker and El-Genk [12] investigated the subcooling effects of a plain 10 mm \times 10 mm flat copper block and compared them with a porous graphite surface in FC-72 and reported that the CHF ratio between the porous graphite and the plain surface increased from 1.6 at saturation to 2.1 at 30 K of subcooling. El-Genk and Suszko [13] studied the effect of subcooling in PF-5060 on a dimpled surface and a plain surface and reported the rate of increase in CHF for the dimpled surface being 20% less than that of plain copper.

So far, many researchers have investigated the effects of enhanced surfaces on subcooled boiling with various fluids, but there have been few attempts to systematically investigate the effects of subcooling on pool boiling from enhanced surfaces for water. In the present study, the subcooling effect of copper microporous coatings created by sintering, called high-temperature thermally conductive microporous coatings (HTCMCs), was experimentally investigated with subcooled water of 10–30 K and compared with the results of a plain surface. Then, the experimental results of both the HTCMC and the plain surfaces were compared with the aforementioned correlations [1, 3, 6]. Finally, the combined effects of subcooling and orientation on the boiling heat transfer of the HTCMC at 30 K subcooling were investigated and compared with the previous study of orientation effects at saturation.

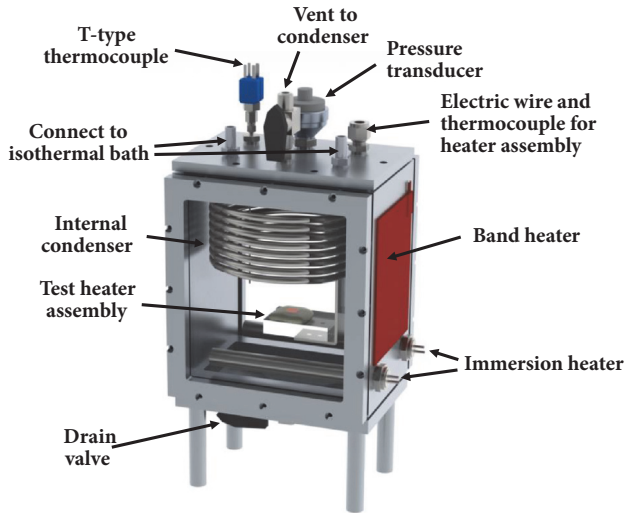


FIGURE 1: Schematic of the pool boiling chamber.

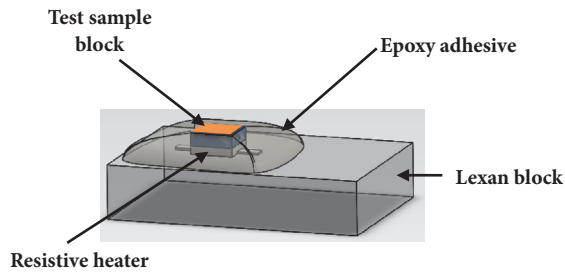


FIGURE 2: Schematic of test heater assembly.

2. Pool Boiling Experiments

2.1. Experiment Setup and Test Procedure. An aluminum chamber was used, as shown in Figure 1. It includes T-type thermocouples, a pressure transducer, internal and external condensers, band and immersion heaters, and a test heater assembly. The T-type thermocouples measured the bulk liquid temperature and the heater temperature. The pressure transducer measured the system pressure. Band and immersion heaters were attached to heat the liquid to the desired subcooling temperature and maintain the temperature during the pool boiling experiment. The stainless steel internal condenser was installed in the chamber and connected to an isothermal bath (Fisher Scientific, ISOTEMP 4100R28 Refrigerated/Heated Bath Circulators) in order to keep the bulk liquid at a constant subcooling temperature during the pool boiling tests. The test heater assembly was located on an aluminum bracket in the chamber and connected to electric wires and a T-type thermocouple.

The detailed configuration of the test heater assembly is shown in Figure 2. A test sample copper block (10 mm × 10 mm × 3 mm, $k = 401 \text{ W/mK}$), which includes the sintered HTCMC on the top, was soldered to a resistive heater. The test sample block and the resistive heater pair were bonded to a 1.27 cm thick Lexan block ($k = 0.2 \text{ W/mK}$) with a 3M epoxy adhesive. The sides of the pair were insulated using

the 3M epoxy as well. Two electrical wires were soldered on each side of the bus bar to supply electrical power to the resistive heater, and a T-type thermocouple wire was inserted in the center of the copper block from the side. The top surface temperature of the test sample block below the HTCMC was calculated by assuming one-dimensional heat conduction through the copper block from the temperature measured by the thermocouple.

The pool boiling chamber was filled with distilled water and heated to the desired subcooled temperature at atmospheric pressure using the band and immersion heaters. Once the water reached the desired subcooled temperature, the liquid was maintained at a nearly constant temperature with little temperature fluctuation ($< \pm 0.5 \text{ K}$) throughout a pool boiling test by controlling the temperature of the cooling water running through the internal condenser supplied from the isothermal bath and the band heaters operated with a temperature controller. All subcooled pool boiling experiments were conducted using the test heater assembly at various subcooled temperatures from 10 to 30 K under increasing heat flux conditions until the CHF condition was reached. During the experiment, the heat fluxes were supplied from a DC power supply (Agilent Technologies, N5771A) to the resistive heater of the heater assembly and measured by a data acquisition system (Agilent Technologies, 34980A Multifunction Switch/Measure Unit) controlled by the LabVIEW program installed on a PC. The heat fluxes were increased to the next value of the heat flux by a programmed value after they assumed a steady state if the differences between two consecutive averages of 40 data for 20 seconds each were less than 0.1 K. The CHF was declared once the instantaneous temperature jump was larger than 20 K compared to the immediately before averaged value, and the DC power supply was stopped by the program automatically. The CHF was defined as the heat flux of the last steady state plus half of the heat flux increment that was 25 kW/m^2 .

2.2. Cu-HTCMC Fabrication. In order to create the Cu-HTCMC, copper powder (Alfa Aesar, 99.5%) with an average particle size of $67 \mu\text{m}$ was used. The particle size was measured using an optical microscope, and the particle distribution is shown in Figure 3. The copper powder was mixed with a specially made thinner and spread over a $1 \text{ cm} \times 1 \text{ cm}$ copper block and dried. Then, the sample was sintered in a furnace at high vacuum ($\sim 10^{-5} \text{ hPa}$). After sintering, the sample was cleaned with 5% acetic acid by sonication and rinsed with distilled water.

The SEM image in Figure 4 shows that the HTCMC has porous structures, with a porosity (ϵ) of 0.65 ± 0.03 found by calculating the measured volume of the porous layer (V_t) and the weight of the copper powders (m_{cp}):

$$\epsilon = \frac{V_t - (m_{cp}/\rho_{cp})}{V_t} \quad (5)$$

where ρ_{cp} is the density of the copper powders (8.96 g/cm^3).

2.3. Uncertainty Analysis. The experimental uncertainties for the current study were estimated by single-sample

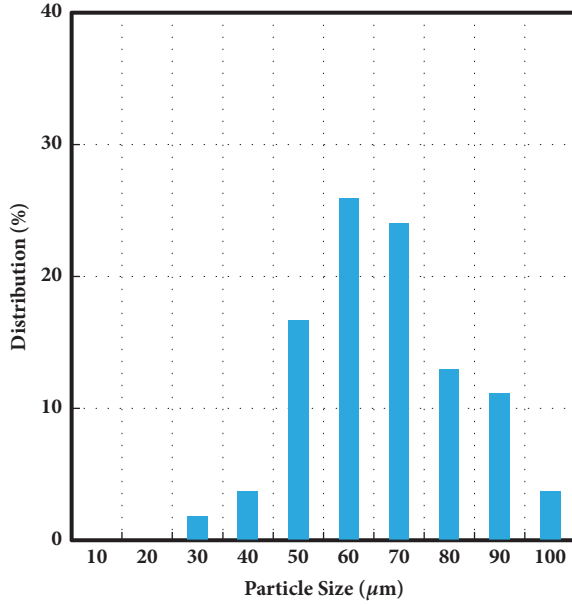


FIGURE 3: Particle size distribution with an average size of 67 μm . The sizes were measured using optical microscope images of Cu powders.

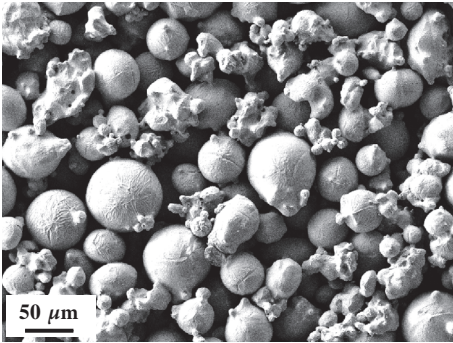


FIGURE 4: SEM of HTCMC sintered copper particles.

uncertainties using the method which was developed by Kline and McClintock [14]. Heat flux measurement uncertainty caused by the current, voltage, and surface area of the heater was estimated to be less than 5% with a 95% confidence level. From numerical simulation, the heat loss through the Lexan and epoxy insulation of the heater was estimated to be less than 0.5%. The temperature accuracy combined from the T-type thermocouple and the data acquisition system was estimated to be ± 0.5 K.

3. Results and Discussion

The pool boiling of the subcooled water was studied experimentally for subcoolings of 10, 20, and 30 K at atmospheric pressure for both the plain copper and HTCMC surfaces. The plain copper surface was polished with a 600 grit sand paper. For the HTCMC, a copper powder with an average particle size of 67 μm with ~ 300 μm coating thickness was tested, which appeared to be the most enhanced nucleate

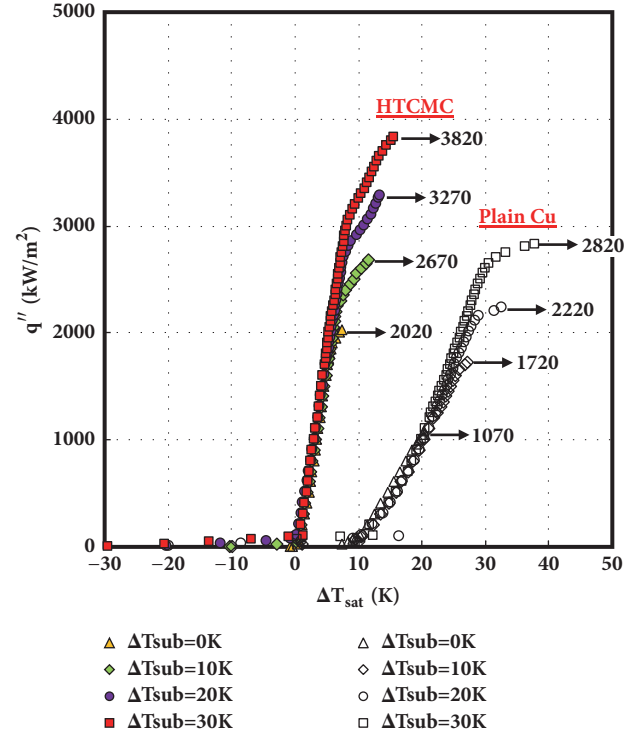


FIGURE 5: Boiling curves of HTCMC and a plain Cu surface at subcoolings.

boiling heat transfer (NBHT) and critical heat flux (CHF) [15]. The results at saturation showed that the NBHT and the CHF (the numeric values next to the arrows in Figure 5) are significantly enhanced compared to those of a plain surface, as shown in Figure 5. According to Jun et al. [16], the enhancement of the NBHT coefficient of the HTCMC is attributed to its porous structure with micron-scale cavities and reentrant-type cavities which create larger embryonic bubbles. Reentrant-type cavities are stable in generating vapor bubbles even at low wall superheat by combining the effects of their geometry and the thermodynamic aspects of the fluid [17]. The condition for an embryonic bubble growing in a cavity can be expressed by combining the Young–Laplace and Clausius–Clapeyron equations [18]:

$$\Delta T_{\text{sat}} \cong \frac{2\sigma T_1 v_{lv}}{L_{lv} R_c} \quad (6)$$

where ΔT_{sat} is the wall superheat ($=T_s - T_{\text{sat}}$), σ is the surface tension of bulk liquid at saturation, T_1 is the bulk liquid temperature, v_{lv} is the specific volume difference between vapor and liquid ($=v_v - v_l$), L_{lv} is the latent heat of vaporization, and R_c is the radius of liquid/vapor interface curvature in a cavity. According to (4), a smaller wall superheat (ΔT_{sat}) is required at larger R_c to make the embryonic bubble grow. Reentrant-type cavities in the HTCMC have a significantly larger R_c compared to those of the plain copper surface, so the wall superheat needed for the embryonic bubble to grow in the HTCMC must be much smaller. Therefore, it leads to the increased number of nucleation sites and NBHT enhancement of the HTCMC.

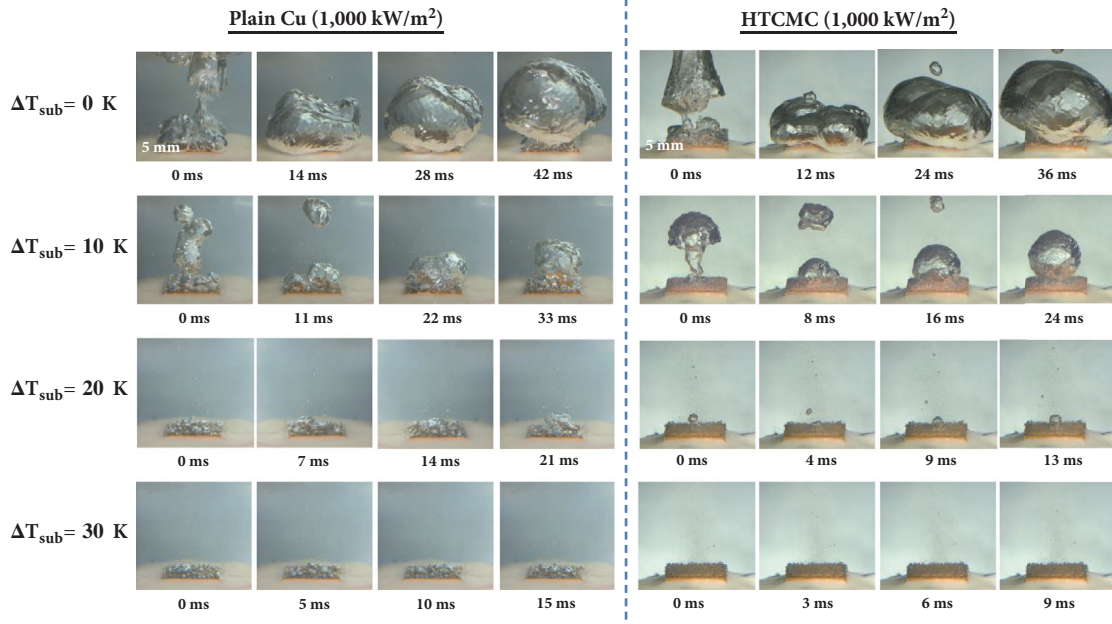


FIGURE 6: Nucleate boiling comparison of Plain Cu and HTC MC with different subcooled temperatures (ΔT_{sub}) of 0 K, 10 K, 20 K, and 30 K at a heat flux of $1,000 \text{ kW/m}^2$.

The subcooled pool boiling of both the HTC MC and the plain copper surfaces revealed that the wall superheats at different subcoolings were close at heat fluxes up to $\sim 2,000 \text{ kW/m}^2$ and $\sim 1,000 \text{ kW/m}^2$, each being near the CHF at saturation. This insensitivity effect of subcooling on NBHT is consistent with previous literature [4, 10–12, 17, 19, 20]. According to Engelburg-Forster and Grief [4], the combined effects of smaller bubble departure diameter and shorter bubble cycle at subcooling make the NBHT little difference at the same heat fluxes. The same trend was observed from the current study. Therefore, the enhancement of the NBHT in the HTC MC was maintained throughout the subcoolings. In other words, the wall superheats of the HTC MC for all the subcooled boiling remained below 5 K for the heat flux of $1,500 \text{ kW/m}^2$, and this is the significant enhancement of the nucleate boiling of the HTC MC compared to the plain copper that showed about 24 K of wall superheat at the same heat flux, as shown in Figure 5. In addition, the higher wall superheat jump for the plain surface compared with that of the HTC MC was observed at nucleate boiling incipience. For example, at 20 K subcooling (yellow circle in Figure 5) the temperature jump was $\sim 5 \text{ K}$ before boiling incipience, whereas it was about only $\sim 1 \text{ K}$ for HTC MC at the same subcooling temperature. This represents the fact that the HTC MC is more effective on nucleate boiling incipience at subcoolings as well [12]. In addition, Figure 5 shows the CHF values of both the HTC MC and the plain surfaces increased as subcooling increased so that the CHF value of the HTC MC was $3,820 \text{ kW/m}^2$ and that of the plain surface was $2,820 \text{ kW/m}^2$ at 30 K subcooling.

Figure 6 shows snapshots obtained with a high speed camera (Phantom, Miro 30) with 2,000 frames per second during boiling experiments with the hovering bubble growth

at different subcoolings of the plain surface and the HTC MC at a heat flux of $1,000 \text{ kW/m}^2$. It can be seen that a bubble size of subcooled boiling is smaller at lower bulk liquid temperature because of the condensation of the bubble by the surrounding subcooled liquid. The hovering bubble sizes for both the plain surface and the HTC MC are comparable at the same subcooling since the hovering bubble cycles of both the HTC MC and the plain surface are similar, but they decrease as the degree of subcooling increases due to the condensation of the surrounding subcooled liquid. On the other hand, the bubbles below the large hovering bubble of the HTC MC are much smaller, and the number of bubbles is much higher than that of the plain surface. The NBHT of the HTC MC was significantly enhanced compared to the plain surface at the same heat flux of $1,000 \text{ kW/m}^2$, as the wall superheat of the HTC MC was $\sim 3 \text{ K}$, whereas that of the plain surface was $\sim 20 \text{ K}$. The hovering bubble cycles of both the HTC MC and the plain surface were comparable at the same subcooling, but they decreased as the subcooling increased from ~ 40 milliseconds (ms) at saturation to ~ 20 ms at 20 K subcooling. In case of the degree of subcooling at 30 K, no hovering bubbles were observed for both surfaces at $1,000 \text{ kW/m}^2$ because of rapid condensation due to high subcooling. Only mist-like tiny bubbles rose upward, as shown in Figure 6, and the mist-like bubbles appeared to be smaller for the microporous surface boiling.

The maximum hovering bubble sizes near the CHF are observed in Figure 7 and they decrease as the degree of subcooling increases, although the CHF values become higher as the subcooling increases. However, the maximum hovering bubble size of the HTC MC is larger than that of the plain surface because of higher CHF values with the HTC MC surfaces. To summarize, it is observed that the hovering

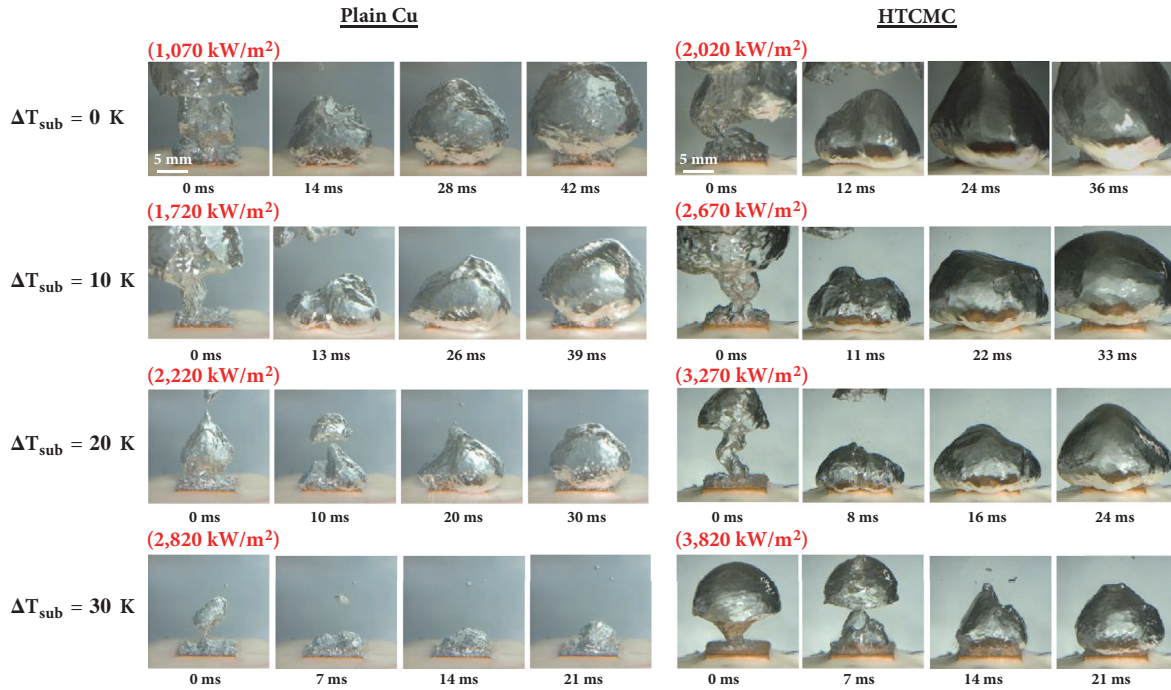


FIGURE 7: Nucleate boiling comparison of Plain Cu and HTCMC with different subcooled temperatures (ΔT_{sub}) of 0 K, 10 K, 20 K, and 30 K at the CHF. The values in parentheses represent applied heat fluxes.

bubble sizes of the HTCMC and the plain surface are similar at the same heat flux as shown in Figure 6, but their size decreases as the subcooling increases and increases as the heat flux increases the vapor bubble generating rate increases as the heat flux increases.

It is well known that CHF increases with subcooling. According to Kutateladze [1], CHF occurs when vapor films are generated between the heater wall and the liquid, so in order to create a vapor film in a subcooled liquid, it is necessary to supply at least enough heat equal to that required for a critical rate of vapor formation in a saturated liquid. This causes CHF enhancement in subcooling. Another explanation for the CHF increase in subcooling is the ease of access for liquid to flow toward a heated surface by condensation of vapor leaving the region of the heated surface through the subcooled pool [17]. The results showed that the CHF of both the plain surface and the HTCMC linearly increases with subcooling and this agrees with previous research [1–3, 5–11, 13, 20, 21], as shown in Figure 8. The increasing rates of CHF due to the subcooling are similar for both the plain and HTCMC surfaces as $\sim 60 \text{ kW/m}^2$ per degree of subcooling. This implies that a similar amount of subcooled water near the heated surfaces is heated to saturation at the same subcooling for both the plain and HTCMC surfaces. As a result, the CHF values of the HTCMC remained $\sim 1,000 \text{ kW/m}^2$ higher than those of the plain surface throughout the subcoolings tested. In case of 30 K of subcooling, the CHF of the plain surface was $2,820 \text{ kW/m}^2$, whereas that of the HTCMC was $3,820 \text{ kW/m}^2$.

The linearity of the CHF with the degree of subcooling was often normalized by the CHF value at saturation [8]:

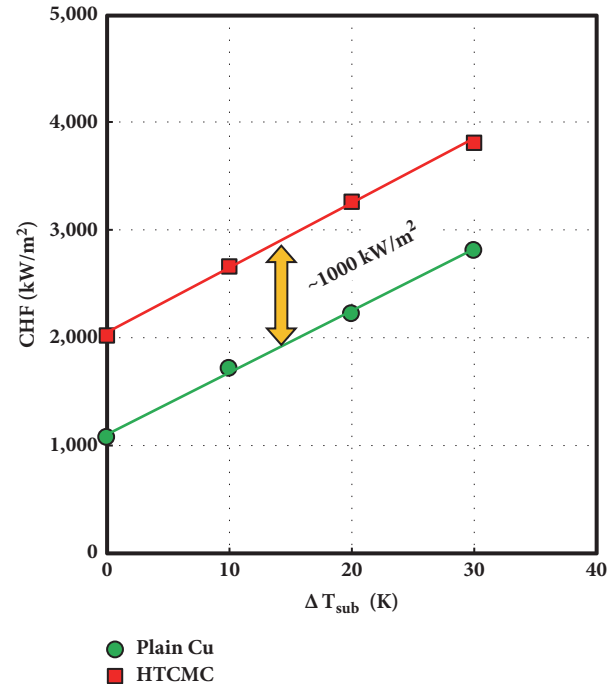


FIGURE 8: CHF comparison of HTCMC and plain surface with subcooling.

$$\frac{q''_{CHF,sub}}{q''_{CHF,sat}} = 1 + C_{sub} \Delta T_{sub} \quad (7)$$

C_{sub} is an empirical constant, and ΔT_{sub} ($=\Delta T_{sat}-T_1$) is the degree of subcooling. The linear increase in normalized CHF

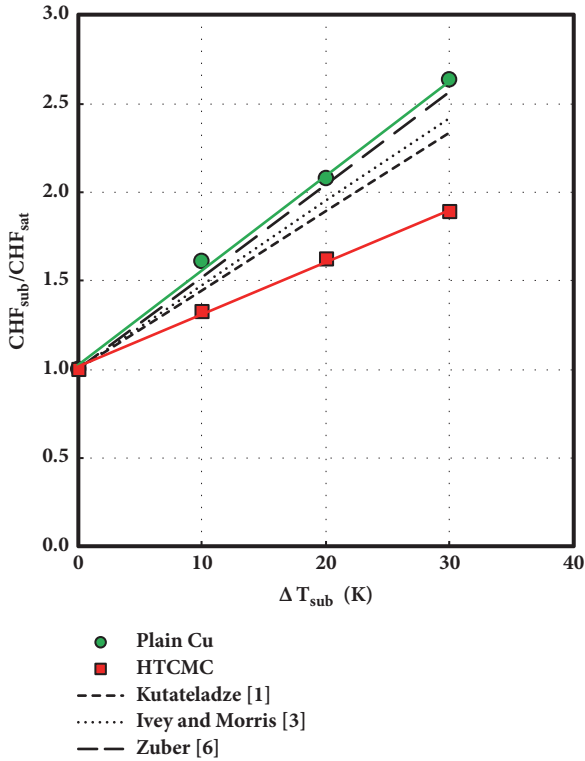


FIGURE 9: Normalized CHF comparison of HTCMC and plain surface with subcooling.

TABLE 1: The coefficient “ C_{sub} ” of (5) for subcooled CHF.

| Result/Model | C_{sub} |
|---------------------|-----------|
| Plain Cu (Present) | 0.0535 |
| HTCMC (Present) | 0.0296 |
| Kutateladze [1] | 0.0446 |
| Ivey and Morris [3] | 0.0482 |
| Zuber [6] | 0.0522 |

with the degree of subcooling is plotted in Figure 9 for water. For the plain surface, the current experiment showed the constant C_{sub} value to be 0.0535 (Table 1) by linear curve fitting. This means a 5.3% increase in the CHF per degree of subcooling. The increment of the plain surface in water is higher than dielectric fluids such as of FC-72 (3.1%) [8] or PF-5600 (2.1%) [13] on a plain surface. This shows that water is more efficient cooling fluid than the others for single-phase, and the CHF thus increases efficiently in subcooled boiling heat transfer compared to the other fluids. The current data of the plain surface were compared with some of the existing CHF correlations and best matched with Zuber’s correlation, as shown in Table 1 and Figure 9. For the HTCMC case, the coefficient of C_{sub} turned out to be 0.0296. Thus, it implies that the rate of CHF increase based on the CHF at saturation of the HTCMC was smaller due to the higher CHF value at saturation. However, the absolute values of increment in CHF for the HTCMC are similar to those of the plain surface, as mentioned above.

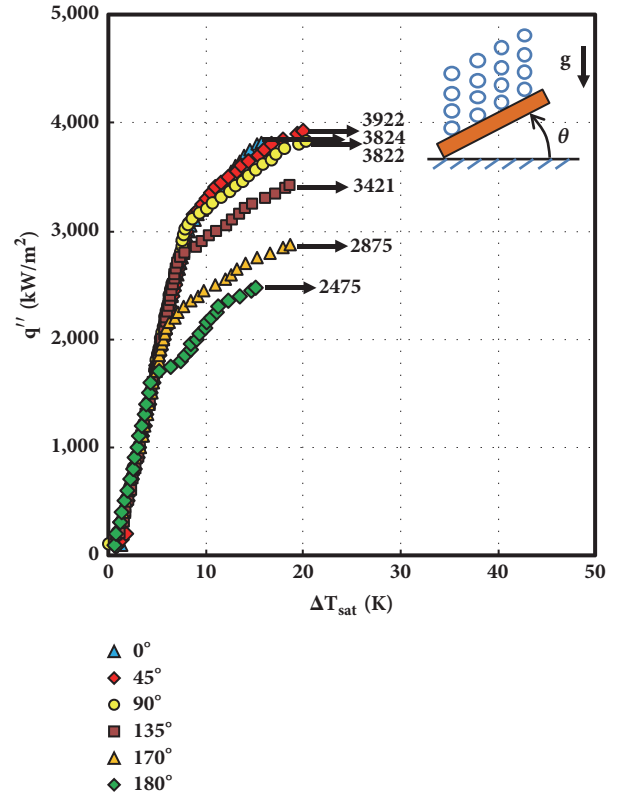


FIGURE 10: Boiling curves of HTCMC with various orientation angles at 30 K subcooling.

The orientation effects on pool boiling with 30 K of subcooling for the HTCMC were examined in order to investigate the combined effects of orientation and subcooling. The heater orientations were varied from 0° to 180° . The results showed that the boiling curves collapsed with single line heat fluxes up to $\sim 1,700 \text{ kW/m}^2$, as shown in Figure 10. The results are consistent with the orientation effects on pool boiling heater transfer of the HTCMC surface at saturation [22]. This implies that the NBHT is not affected much by heater orientations, neither at saturation nor subcooling. The wall superheat started to increase faster as the heat flux increased to higher values due to different partial dryout situations. The CHF values were 3,800–3,900 kW/m^2 at the inclination angles between 0° and 90° and they did not change much, whereas they decreased down to 2,475 kW/m^2 as the inclination angle increased at the downward facing directions (from 90° to 180°) due to a higher residence time of vapor bubbles on the surface, causing dryout by blocking cold liquid access onto the heater surface.

The decreasing CHF trend for facing down cases is similar to the orientation effect on the boiling at saturation [22] as shown in Figure 11. In addition, the CHF further sharply decreases between 170° and 180° , and this angle is called a transition angle. The value of the transition angle is consistent with previous studies [22–25]. Based on the experimental results of CHF values for orientation at 30 K of subcooling for the HTCMC surface, the orientation effect can be classified into three regions: upward to vertical ($0\text{--}90^\circ$) where the

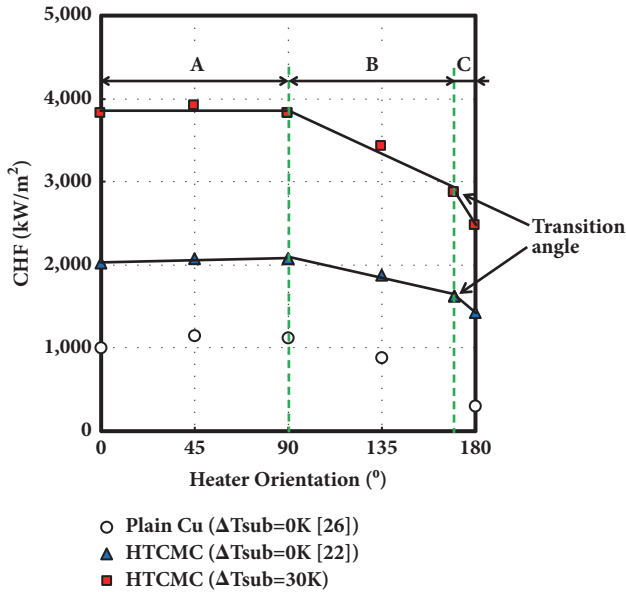


FIGURE 11: CHF comparison of HTCMC with orientation between saturation and 30 K subcooling; A: upward to vertical (0–90°), and B: vertical to downward facing (90–170°), and C: downward facing to complete downward (170–180°).

CHF maintains close values; vertical to inclined downward facing (90–170°) where the CHF linearly decreases with the orientation angle; and further downward facing (170–180°) where the CHF abruptly decreases just as Jun et al. [22] observed in the heater orientation effects at saturation for the HTCMC. It should be also noted in Figure 11 that the decrease in the CHF at 170–180° was much less for the HTCMC cases compared to the drastic decrease of CHF for the plain Cu case observed in Kwark et al. [26]. Delaying the dryout and the CHF of the heated surface when it is downward facing is highly beneficial factor of using HTCMC surfaces.

4. Conclusions

The subcooling effects of pool boiling heat transfer were studied experimentally at subcoolings of 10, 20, and 30 K for a Cu-HTCMC and a plain surface, and the boiling heat transfer and the CHF were compared. The results showed that the nucleate boiling heat transfer did not change much with the degree of subcooling for both the HTCMC and the plain surface. However, the CHF linearly increased with the similar rates of 60 kW/m² per degree for both surfaces, so the CHF values of the HTCMC stayed about ~1,000 kW/m² higher than those of the plain surface throughout the subcooling. For the plain surface, the CHF values were well matched with Zuber's correlation for subcooling. The combined effect of orientation and subcooling was also investigated for the HTCMC at 30 K subcooling and it was compared with the data at saturation. The results showed that the nucleate boiling heat transfer was close up to ~1,700 kW/m² regardless of the heater orientation. The CHF values of the HTCMC at different orientations with the subcooling 30 K showed the

same trend with those of saturation case. The CHF values for Cu-HTCMC stayed at 3,800~3,900 kW/m² at upward to vertical orientation (0–90°) and linearly decreased at downward facing orientations (90–170°) and then sharply decreased at further downward facing angles (170–180°) to ~2,500 kW/m².

Nomenclature

| | |
|---------------------------|--|
| C: | Empirical constant |
| c_p : | Specific heat [J/kgK] |
| g: | Gravitational acceleration [m/s ²] |
| h: | Boiling heat transfer coefficient [W/m ² K] |
| k: | Thermal conductivity [W/mK] |
| L: | Latent heat of vaporization [J/kg] |
| R: | Radius [m] |
| q'' : | Heat flux [W/m ²] |
| T: | Temperature [K] |
| ΔT_{sat} : | Wall superheat [K] |
| ΔT_{sub} : | Degree of subcooling [K] |
| V: | Volume [m ³] |
| v: | Specific volume [m ³ /kg]. |

Greek Symbols

| | |
|-----------------|---|
| α : | Thermal diffusivity [m ² /s] |
| σ : | Surface tension [N/m] |
| ε : | Porosity |
| τ : | Bubble residence time [s]. |

Subscripts

| | |
|------|----------------------|
| c: | Cavity |
| cp: | Copper powder |
| l: | Liquid |
| lv: | Liquid-vapor |
| m: | Microporous coating |
| p: | Plain |
| sat: | Saturated conditions |
| sub: | Subcooled conditions |
| t: | Total. |

Data Availability

The data used to support the findings of this study are available from the corresponding author upon request.

Disclosure

Partial work of this study was presented at Second Thermal and Fluids Engineering Conference, 2017.

Conflicts of Interest

The authors declare that they have no conflicts of interest.

Acknowledgments

This work was supported by the National Research Foundation of Korea (NRF) grant funded by the Korean government (Ministry of Science and ICT; Grant no. 2017 M2A8A4015274).

References

- [1] S. S. Kutateladze, "Heat Transfer in Condensation and Boiling," Tech. Rep., State Scientific and Technical Publishers of Literature on Machinery, 1952.
- [2] S. Kutateladze and L. Schneiderman, "Experimental study of influence of temperature of liquid on change in the rate of boiling," USAEC Report AECtr. 3405, 1953.
- [3] H. Ivey and D. Morris, *On the Relevance of the Vapour-Liquid Exchange Mechanism for Sub-Cooled Boiling Heat Transfer at High Pressure*, Reactor Development Division, Atomic Energy Establishment, 1962.
- [4] K. Engelburg-Forster and R. Grief, "Heat transfer to a boiling liquid-mechanism and correlations," *Journal of Heat Transfer*, vol. 81, pp. 43–53, 1959.
- [5] H. Ivey and D. Morris, "Critical heat flux of saturation and subcooled pool boiling in water at atmospheric pressure," in *Proceedings of the 3rd International Heat Transfer Conference*, vol. 4, pp. 129–142, 1966.
- [6] N. Zuber, M. Tribus, and J. W. Westwater, "The hydrodynamic crisis in pool boiling of saturated and subcooled liquids," *International Developments in Heat Transfer*, vol. 27, pp. 220–236, 1963.
- [7] U. Hwang and K. Moran, "Boiling heat transfer of silicon integrated circuits chip mounted on a substrate," in *Proceedings of the Winter Annual Meeting*, vol. 1, pp. 53–59, 1981, Boiling heat transfer of silicon integrated circuits chip mounted on a substrate, 1.
- [8] I. Mudawar and T. M. Anderson, "Parametric investigation into the effects of pressure, subcooling, surface augmentation and choice of coolant on pool boiling in the design of cooling systems for high-power-density electronic chips," *Journal of Electronic Packaging, Transactions of the ASME*, vol. 112, no. 4, pp. 375–382, 1990.
- [9] A. A. Watwe, A. Bar-Cohen, and A. McNeil, "Combined pressure and subcooling effects on pool boiling from a PPGA chip package," *Journal of Electronic Packaging, Transactions of the ASME*, vol. 119, no. 2, pp. 95–105, 1997.
- [10] K. N. Rainey, S. M. You, and S. Lee, "Effect of pressure, subcooling, and dissolved gas on pool boiling heat transfer from microporous surfaces in FC-72," *Journal of Heat Transfer*, vol. 125, no. 1, pp. 75–83, 2003.
- [11] K. N. Rainey, S. M. You, and S. Lee, "Effect of pressure, subcooling, and dissolved gas on pool boiling heat transfer from microporous, square pin-finned surfaces in FC-72," *International Journal of Heat and Mass Transfer*, vol. 46, no. 1, pp. 23–35, 2003.
- [12] J. L. Parker and M. S. El-Genk, "Enhanced saturation and subcooled boiling of FC-72 dielectric liquid," *International Journal of Heat and Mass Transfer*, vol. 48, no. 18, pp. 3736–3752, 2005.
- [13] M. S. El-Genk and A. Suszko, "Effects of inclination angle and liquid subcooling on nucleate boiling on dimpled copper surfaces," *International Journal of Heat and Mass Transfer*, vol. 95, pp. 650–661, 2016.
- [14] S. J. Kline and F. McClintock, "Describing uncertainties in single-sample experiments," *Mechanical Engineering*, vol. 75, pp. 3–8, 1953.
- [15] S. Jun, J. Kim, D. Son, H. Y. Kim, and S. M. You, "Enhancement of Pool Boiling Heat Transfer in Water Using Sintered Copper Microporous Coatings," *Nuclear Engineering and Technology*, vol. 48, no. 4, pp. 932–940, 2016.
- [16] S. Jun, H. Wi, A. Gurung, M. Amaya, and S. M. You, "Pool boiling heat transfer enhancement of water using brazed copper microporous coatings," *Journal of Heat Transfer*, vol. 138, no. 7, Article ID 071502, 2016.
- [17] V. P. Carey, *Liquid-Vapor Phase-Change Phenomena*, Taylor & Francis Group, New York, NY, USA, 2nd edition, 2008.
- [18] E. E. Anderson, *Thermodynamics*, PWS Publishing Company, Boston, Mass, USA, 1st edition, 1994.
- [19] A. Ono and H. Sakashita, "Liquid-vapor structure near heating surface at high heat flux in subcooled pool boiling," *International Journal of Heat and Mass Transfer*, vol. 50, no. 17-18, pp. 3481–3489, 2007.
- [20] M. S. El-Genk and A. Suszko, "Saturation and subcooled CHF correlations for PF-5060 dielectric liquid on inclined rough copper surfaces," *Multiphase Science and Technology*, vol. 26, no. 2, pp. 139–170, 2014.
- [21] T. Inoue, N. Kawae, and M. Monde, "Effect of subcooling on critical heat flux during pool boiling on a horizontal heated wire," *Heat and Mass Transfer*, vol. 33, no. 5-6, pp. 481–488, 1998.
- [22] S. Jun, J. Kim, S. M. You, and H. Y. Kim, "Effect of heater orientation on pool boiling heat transfer from sintered copper microporous coating in saturated water," *International Journal of Heat and Mass Transfer*, vol. 103, pp. 277–284, 2016.
- [23] Y. H. Kim and K. Y. Suh, "One-dimensional critical heat flux concerning surface orientation and gap size effects," *Nuclear Engineering and Design*, vol. 226, pp. 277–292, 2003.
- [24] S. H. Yang, W.-P. Baek, and S. H. Chang, "Pool-boiling critical heat flux of water on small plates: Effects of surface orientation and size," *International Communications in Heat and Mass Transfer*, vol. 24, no. 8, pp. 1093–1102, 1997.
- [25] A. H. Howard and I. Mudawar, "Orientation effects on pool boiling critical heat flux (CHF) and modeling of CHF for near-vertical surfaces," *International Journal of Heat and Mass Transfer*, vol. 42, no. 9, pp. 1665–1688, 1999.
- [26] S. M. Kwark, M. Amaya, R. Kumar, G. Moreno, and S. M. You, "Effects of pressure, orientation, and heater size on pool boiling of water with nanocoated heaters," *International Journal of Heat and Mass Transfer*, vol. 53, no. 23-24, pp. 5199–5208, 2010.

Research Article

A Conceptual Approach to Eliminate Bypass Release of Fission Products by In-Containment Relief Valve under SGTR Accident

Taeseok Kim ¹, Wonjun Choi ¹, Joongoo Jeon ¹, Nam Kyung Kim ¹,
Hoichul Jung¹ and Sung Joong Kim ^{1,2}

¹Department of Nuclear Engineering, Hanyang University, Seoul 04763, Republic of Korea

²Institute of Nano Science and Technology, Hanyang University, Seoul 04763, Republic of Korea

Correspondence should be addressed to Sung Joong Kim; sungjkim@hanyang.ac.kr

Received 22 March 2018; Accepted 18 July 2018; Published 6 August 2018

Academic Editor: Seong Wan Hong

Copyright © 2018 Taeseok Kim et al. This is an open access article distributed under the Creative Commons Attribution License, which permits unrestricted use, distribution, and reproduction in any medium, provided the original work is properly cited.

During a hypothesized severe accident, a containment building is designed to act as a final barrier to prevent release of fission products to the environment in nuclear power plants. However, in a bypass scenario of steam generator tube rupture (SGTR), radioactive nuclides can be released to environment even if the containment is not ruptured. Thus, thorough mitigation strategies are needed to prevent such unfiltered release of the radioactive nuclides during SGTR accidents. To mitigate the consequence of the SGTR accident, this study was conducted to devise a conceptual approach of installing In-Containment Relief Valve (ICRV) from steam generator (SG) to the free space in the containment building and it was simulated by MELCOR code for numerical analysis. Simulation results show that the radioactive nuclides were not released to the environment in the ICRV case. However, the containment pressure increased more than the base case, which is a disadvantage of the ICRV. To minimize the negative effects of the ICRV, the ICRV linked to Reactor Drain Tank (RDT) and cavity flooding was performed. Because the overpressurization of containment is due to heat of ex-vessel corium, only cavity flooding was effective for depressurization. The conceptual design of the ICRV is effective in mitigating the SGTR accident.

1. Introduction

Prevention or mitigation of fission product release is very important to guarantee ultimate safety of nuclear power plants (NPPs). Faithful to the Defence-in-Depth philosophy, a containment building is designed and constructed as the last barrier to prevent the fission product release under severe accident (SA) scenarios [1]. Many researchers have studied hazardous factor such as direct containment heating [2], steam explosion [3], hydrogen combustion [4], and overpressure [5]. These studies enhance reliability of the containment building.

However, in a hypothesized scenario of containment bypass, even if the containment building is not ruptured, fission products can be released to the environment. Representative bypass accidents are interfacing system loss of coolant accident (ISLOCA) and steam generator tube rupture (SGTR). ISLOCA is containment bypass accident where a pipeline connected to the reactor coolant system (RCS) is

broken outside of the containment [6]. SGTR accident can release fission products to environment without containment rupture because pressure boundary of the primary system is not retained due to SGTR [7]. Due to characteristics of containment bypass accidents, some sensitivity studies of bypass were conducted [8, 9].

The SGTR accident, especially, can be induced by the other SAs. Station blackout (SBO) accident such as the one that occurred in Fukushima can induce SGTR with failure of turbine-driven auxiliary feed water (TDAFW) [10]. During an extreme situation of SBO transient, steam generator (SG) U-tube integrity could be threatened by thermally or pressure-induced creep rupture [11]. The SGTR accident induced by SBO releases more fission products to environment because many safety features such as auxiliary feed water (AFW) are inoperable. Therefore, to fortify the safety of the NPP during the SGTR accident, a more creative mitigation strategy needs to be devised.

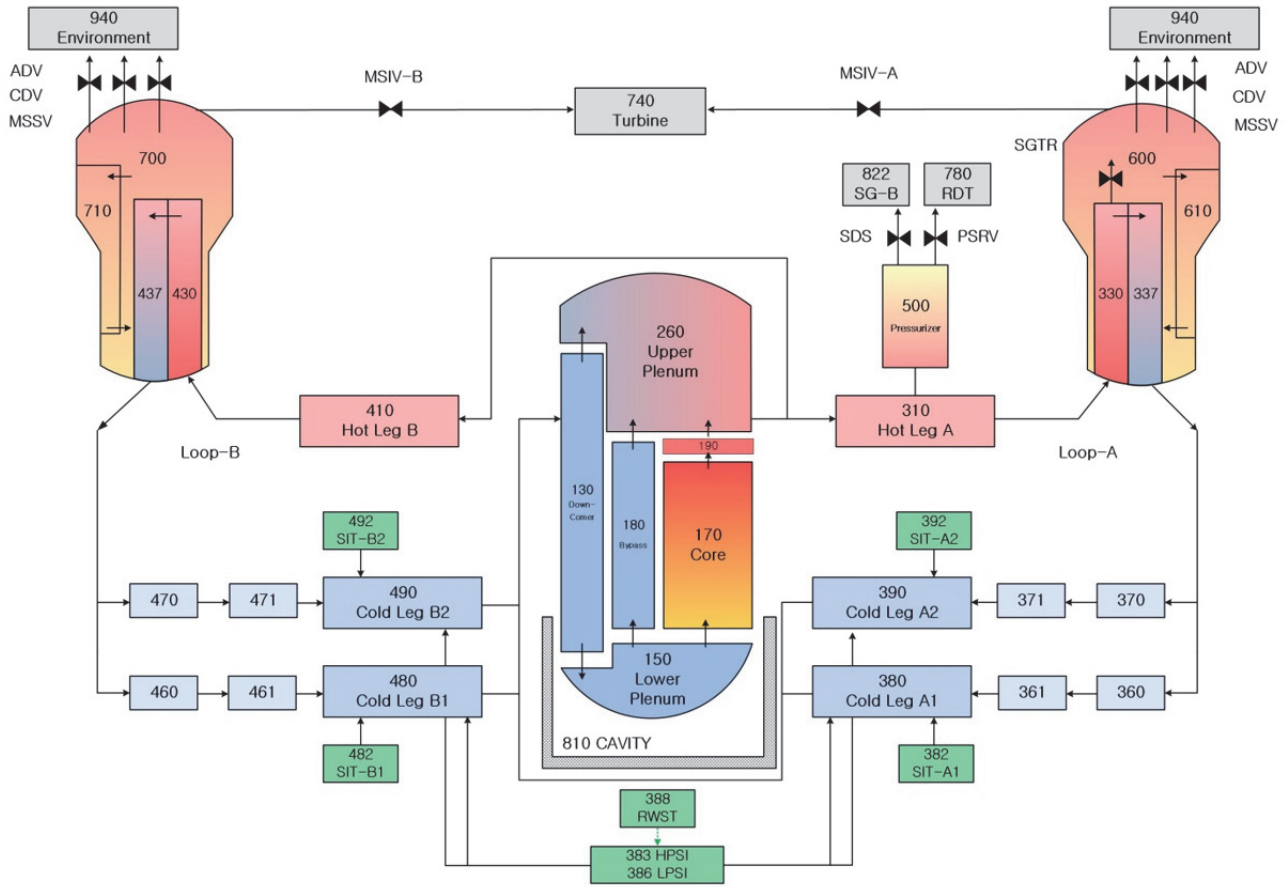


FIGURE 1: MELCOR nodalization of OPR1000.

In this study, a conceptual approach was taken to mitigate the consequence of SGTR accident by generating in-containment relief valve (ICRV). The ICRV is additional paths from SG to in-containment free space such as upper dome and reactor drain tank (RDT) for venting steam of the secondary system. To investigate its effectiveness in Optimized Power Reactor 1000 MWe (OPR1000) consisting of a major fleet of Korean operating NPPs, numerical simulation was conducted using MELCOR code.

2. Numerical Methodologies

2.1. MELCOR Code. MELCOR code is a SA analysis code developed for light water reactors (LWRs). Since 1982, Sandia National Laboratories have been developed for use in plant risk assessment and source term analysis for US Nuclear Regulatory Commission [12]. MELCOR can simulate various SA phenomena such as thermal-hydraulic response of the primary RCS, core uncovering, fuel heat-up, cladding oxidation, heat-up of the reactor pressure vessel (RPV) lower head by the molten core, lower plenum penetration, hydrogen production, and fission product release. Because of this usefulness in analyzing SA, MELCOR is usually used for uncertainty analysis and sensitivity studies [13]. In addition, many countries have used MELCOR for the regulation of

LWR [14]. Particularly, the Korean regulatory body has utilized MELCOR for monitoring and judgement of SAs [15, 16]. Thus, in this study, MELCOR version 2.1 was used to investigate effectiveness and adverse effects of the ICRV.

2.2. MELCOR Input Model of OPR1000. The Korean pressurized water reactor (PWR) OPR1000 as a reference plant was modelled in MELCOR. OPR1000 nodalization consists of two loops of nuclear steam supply system and containment. Figure 1 shows a schematic nodalization of OPR1000 for the MELCOR simulation. The input model includes a core (control volume (CV) 170), a downcomer (CV 130), a lower plenum (CV 150), an upper plenum (CV 260), two hot legs (CV 310 and 410), four cold legs (CV 380, 390, 480, and 490), and a pressurizer (CV 500). Two SGs are composed of a primary side inlet (CV 330 and 430), outlet (CV 337 and 437), and secondary sides (CV 600, 700, 610, and 710). Safety features consist of four safety injection tanks (SITs; CV 382, 392, 482, and 492), high-pressure safety injection (HPSI; CV 383), and low-pressure safety injection (LPSI; CV 386) connected refuelling water tank (RWT; CV 388). In addition, AFW, the safety depressurization system (SDS), containment spray, the passive autocatalytic recombiner (PAR), pressurizer safety relief valve (PSRV), main steam safety valve (MSSV), and atmospheric dump valve (ADV) were also modelled

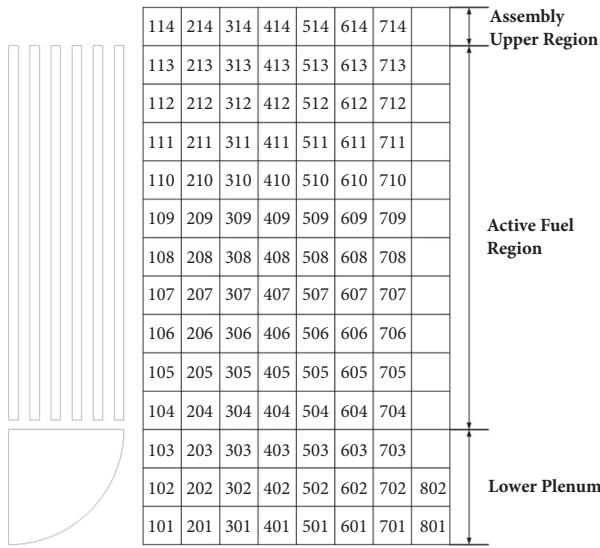


FIGURE 2: MELCOR nodalization for core.

to enable depressurization of the primary and secondary systems. MSSVs are operated above 8.6 MPa of SG pressure.

The core nodalization for MELCOR calculation included 7 radial rings and 14 axial levels (Figure 2). The lower plenum (CV 150) extended from the first to the third axial level, the core region (CV 170) extended from the fourth to thirteenth axial levels, and the fourteenth axial level of the core cell represented the upper region of the fuel assembly, from which the core exit temperature (CET) information was extracted. The lower plenum allows seven penetrations and hemispheric lower head type is optioned.

The nodalization of containment was based on the compartment configuration of the MAAP-CONTAIN analysis [4]. Figure 3 shows the nodalization of containment. It was also based on the layout of the containment building in the Final Safety Analysis Report (FSAR) for Shin Kori NPP Units 1 and 2 [17]. The 20 CVs were constructed according to the axial height and function of each compartment. The total volume of the 20 CVs modelled was 77,420.92 m³, which is approximately the same as the containment volume specified in the FSAR.

2.3. Description of the SGTR Accident. The SGTR scenario was selected as the main accident scenario due to the bypassed release of radionuclides to the environment unlike other accident scenarios such as small break loss of coolant accident (SBLOCA), SBO, and total loss of feed water (TLOFW) [7]. To investigate effectiveness of a new mitigation strategy creating an ICRV, very conservative conditions with the SGTR scenario were applied in this simulation. First, the accident started with a complete break of one U-tube in SG, with flow area of 4.49×10^{-4} m². Second, the active safety systems such as HPSI, LPSI, and SDS were assumed to fail. Finally, AFW was assumed unavailable in the secondary system. Henceforth, only the passive safety features such as PSRV, MSSV, and SITs were assumed available in the

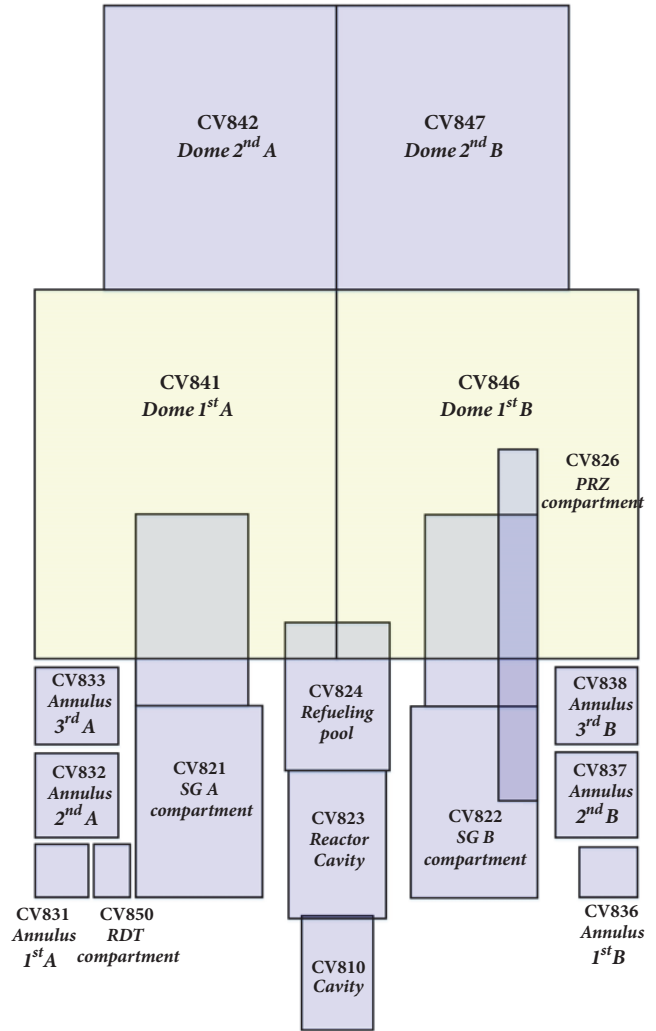


FIGURE 3: MELCOR nodalization for the OPR1000 containment.

simulation. Between a SG tube (CV330) and SG (CV600), a flow path was modelled to simulate the SGTR accident. Figure 4 shows the description of the steam generator tube rupture modelling.

2.4. Description of In-Containment Relief Valve (ICRV). To prevent release of the radioactive nuclides through MSSV, an ICRV was modelled in this study. The ICRV is connected between SG and in-containment space such as upper dome and RDT. If a case includes no ICRV (base case), the radionuclides contained in steam can be released to the environment directly via the MSSV. However, cases bearing the ICRV (ICRV case) do not allow release of radionuclide to the environment without containment rupture. This study was conducted with two types of the ICRV cases and a base case as shown in Figure 5. The base case includes MSSV to prevent overpressurization of the secondary system. The MSSV is connected between SG and the environment (Figure 5(a)). On the other hand, the ICRV cases model the ICRV instead of MSSV. One ICRV case has ICRV connected to upper dome in the containment (CNMT). The other case that has the

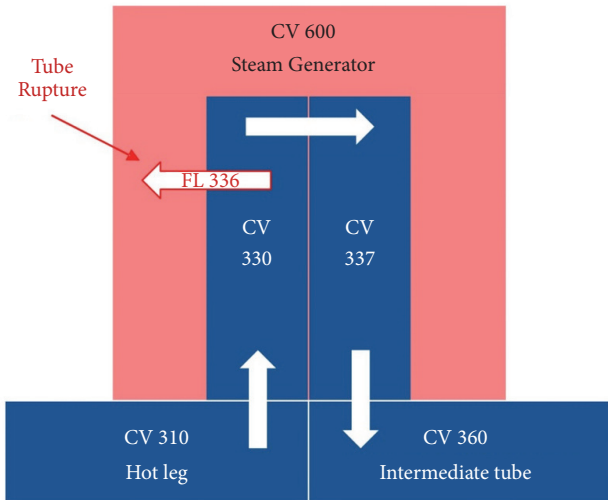


FIGURE 4: A schematic of the steam generator tube rupture in MELCOR input model.

TABLE 1: Comparison of major parameters between FSAR values and MELCOR calculation.

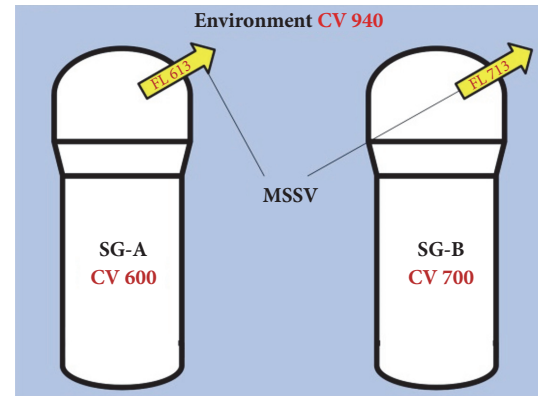
| Parameter | FSAR [17] | MELCOR | Error (%) |
|-------------------------------|-----------|--------|-----------|
| Core thermal power (MWt) | 2815 | 2815 | 0.00 |
| RCS pressure (MPa) | 15.5 | 15.5 | 0.00 |
| Core inlet temperature (K) | 569 | 573 | 0.70 |
| Core outlet temperature (K) | 600 | 603 | 0.50 |
| Primary flow rate (kg/s) | 15,306 | 15,546 | 1.33 |
| Secondary side pressure (MPa) | 7.37 | 7.37 | 0.00 |
| Steam flow rate per SG (kg/s) | 800 | 809 | 1.13 |

valve is connected to RDT for heat removal of the steam using the RDT water. The condensation effect was especially investigated in the ICRV-RDT case because relatively small volume of the RDT may not accommodate the substantial amount of steam release from the SG if effective condensation of the steam does not occur. The path parameters such as flow area, length, and open pressure were determined based on the specifications of the MSSV.

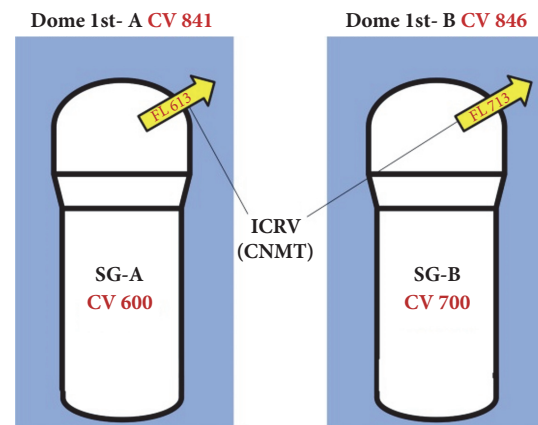
3. Results and Discussion

3.1. Steady-State Calculation. Using the current MELCOR simulation, a steady-state calculation was performed to verify the suitability of the MELCOR nodalization of OPR1000. Steady-state operating conditions of OPR1000 from the MELCOR calculation were compared with corresponding values specified by the FSAR [17] and were summarized in Table 1. It was confirmed that the MELCOR results are in good agreement with the nominal FSAR values. Thus, the input model used in this study confirmed the suitability of current MELCOR nodalization of OPR1000 during the severe accident.

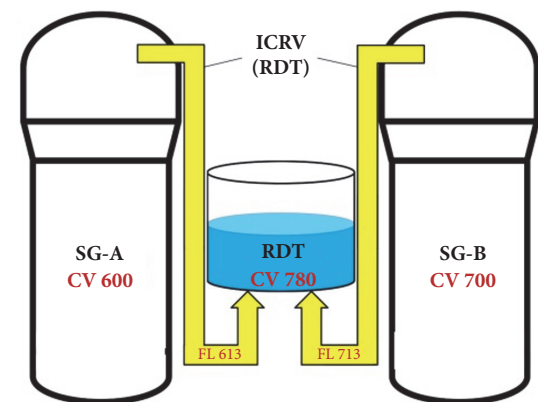
3.2. Base Case Simulation. The base case of SGTR scenario was simulated using MELCOR 2.1. Table 2 shows the accident sequences in base case. When the accident started, the



(a)



(b)



(c)

FIGURE 5: Schematic of simulation cases: (a) base case, (b) ICRV-CNMT case, and (c) ICRV-RDT case.

primary coolant was transported to the secondary system. It increased the secondary pressure and decreased the RCS pressure. Then, a reactor trip occurred with MFW trip and MSIV closure. In this scenario, the AFW was assumed unavailable in the secondary system. Thus, a large amount of the steam was released into the environment through the MSSV. The RCP was stopped by cavitation after the reactor trip. The core was uncovered and heated because of loss of the coolant through the MSSV. As the primary

TABLE 2: Accident sequences in the base case.

| Accident sequence | SGTR base (s) |
|-------------------|-----------------|
| Accident start | 0 |
| MFW trip | 2,654 (0.74 h) |
| Reactor trip | 2,654 (0.74 h) |
| MSSV open | 2,654 (0.74 h) |
| RCP trip | 2,672 (0.74 h) |
| Oxidation start | 12,437 (3.45 h) |
| Gap release | 12,644 (3.51 h) |
| Cladding melting | 13,872 (3.85 h) |
| Melt relocation | 14,328 (3.98 h) |
| RPV failure | 21,406 (5.94 h) |

water was depleted and the core water temperature increased, zircaloy in the fuel cladding was highly oxidized by the high temperature steam. During this oxidation process, substantial amount of oxidation heat was generated, which accelerated the core damage. Subsequently, the fuels were subjected to extremely high temperature condition and the reactor core started to melt down and relocate to the lower plenum of the RPV. Finally, RPV failure was predicted by the thermal attack of molten corium in the penetration location.

Figure 6 shows the primary and secondary system pressure. In the early state of the accident, RCS pressure decreased by coolant release through the tube rupture. Without safety injection, coolability of the core was not maintained. Thus, the core temperature increased and the RCS pressure increased despite tube rupture. The coolant was released continuously to the environment through the MSSV and the system pressure decreased with time. After RPV failure, the system pressure rapidly decreased by ejection of the corium and the coolant. The secondary side pressure reached 8.6 MPa, which is the MSSV open pressure. The valve was kept open until RPV failure and secondary pressure rapidly decreased only in broken SG. In the broken SG side, the coolant was released to the outside of the RCS through the tube rupture. Thus, the pressure quickly decreased at the time of RPV failure. However, no mass transfer occurs in the intact SG side and thus the pressure was maintained although the RPV failed.

The tendency of the accident progress in terms of the water level of the SGs and reactor core is shown in Figure 7. Following the SGTR event, the primary system water crossed over the secondary system and thereby the primary system water level decreased. Before the reactor trip, the water level of the broken SG was not decreased because the MFW was not tripped and the MSIV was not closed. However, the water level of the broken and intact SGs rapidly decreased after the MFW trip and corresponding MSSV open. When the water level of the broken SG was reached to the SGTR set point, the residual water in the U-tube and that in hot- and cold-leg were evaporated together. Therefore, a very gradual decrease in water level was observed in the broken SGs between 2.5 to 6 hrs before RPV failure. Although the duration of the gradual decrease in water level is different, a similar tendency was reported in Wang et al.'s study, which performed the SGTR

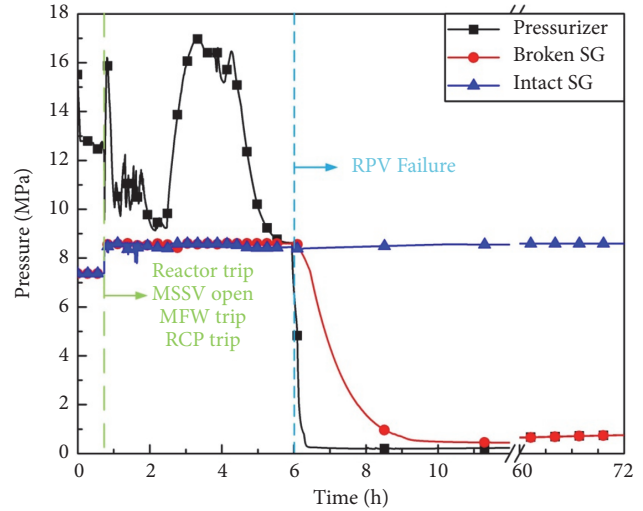


FIGURE 6: Pressure of the RCS and SGs in the base case.

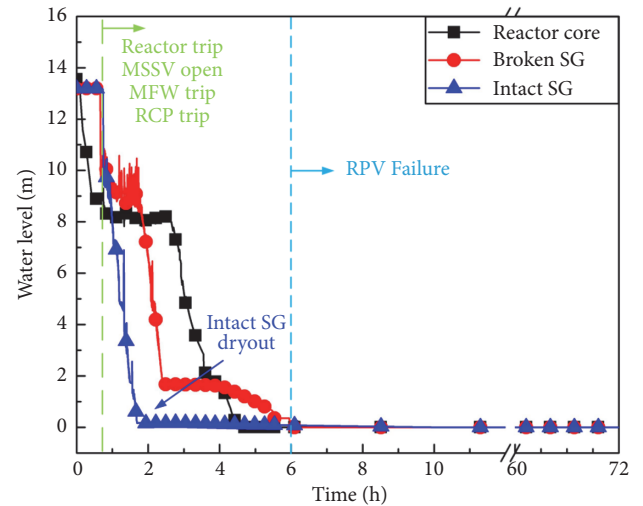


FIGURE 7: The water level of the RCS and SGs in the base case.

analysis using RELAP5/MOD3.4 [18]. Following the RPV failure, the reactor core water level decreased down to 0 m.

As mentioned above, the steam of secondary system was released to the environment through MSSV. Figure 8 shows the released steam mass through MSSV in the base case. After MSSV opening due to overpressure of the secondary system, both SGs released steam to the environment. In the intact SG, the most steam was released earlier than in the broken SG. Because the pressure boundary was not broken in the intact SG, the water in the SG was dried out earlier than broken SG. After dryout, increase of the pressure by boiling did not occur anymore. So, the release of the steam was almost stopped at the SG dryout. On the other hand, the steam release through the broken SG continued due to inflow of the primary coolant through ruptured SG tube. The primary system was connected to the broken SG by ruptured SG tube. Thus, the broken SG received sufficient water from primary system until RPV failure. When the RPV

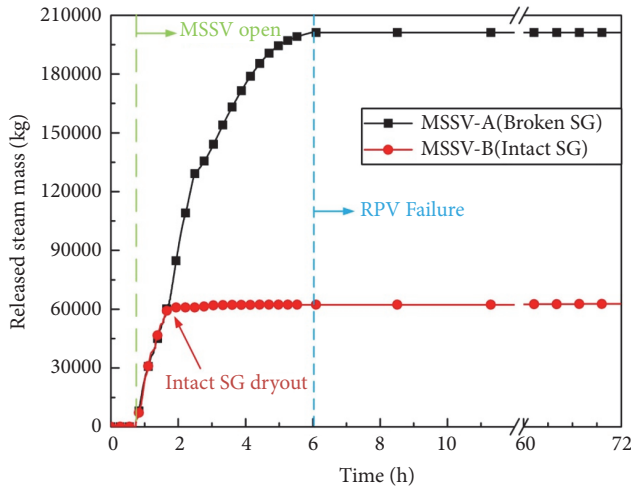


FIGURE 8: Released steam mass through MSSV in the base case.

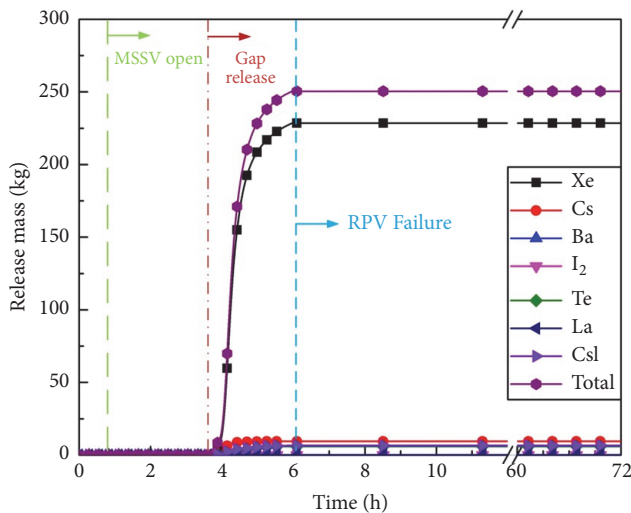


FIGURE 9: The release of mass of radionuclides to the environment in the base case.

failure occurred, a large amount of water and core debris were ejected outside of primary system. Because the pressure was quickly decreased at the time of RPV failure (Figure 6), the steam release through the broken SG was stopped.

In the base case, it was predicted that radionuclides were released to the environment through the MSSV of the broken SG side. The pressure of the secondary system reached the MSSV open pressure at the early stage of accident (0.74 h), at which the radionuclides were not released to the environment because it existed only in fuel before the gap release. After elapsing gap release time, however, the radionuclides were released to the coolant and transported to the secondary side. So, it was predicted that the radionuclides could be released to the environment after the gap release. But, the release of the radionuclides stopped at the time of RPV failure. It is because the primary and secondary system pressure decreased at the time of RPV failure (Figure 6). So, the MSSV was closed with lower pressure. This is clearly seen in Figure 9, in which the

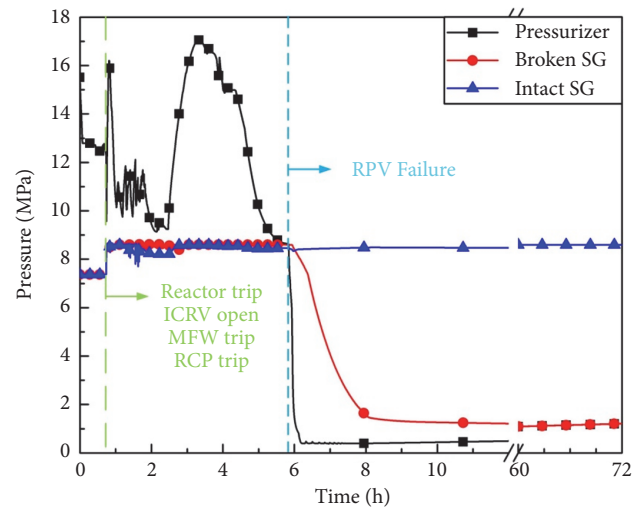


FIGURE 10: Pressure of the RCS and SGs in the ICRV-CNMT case.

release of the radionuclides to the environment stopped after RPV failure.

3.3. ICRV-CNMT Case Simulation. The ICRV-CNMT case is that the steam of the secondary system releases to the upper dome to prevent the release of the radioactive nuclides to environment. The specifications of the ICRV such as flow area are identical to MSSV except exit target. Figure 10 shows the system pressure of the ICRV-CNMT case. Because activation pressure of the ICRV is the same as MSSV, the SG pressure after ICRV opening was kept at 8.6 MPa similar to the base case. Compared to the base case, only exit location of the relief valve is different in the ICRV-CNMT case. Thus, the overall system pressure is similar between the base case and ICRV-CNMT case. However, the pressure of the pressurizer and broken SG in the latter period was different between the base and the ICRV-CNMT case. This is because the steam resided in the containment in the ICRV-CNMT case. It caused containment pressure to increase and affected the pressure of the pressurizer and the broken SG after the time of RPV failure.

The ICRV-CNMT case also retains the secondary pressure through the steam release to the outside of the secondary system. However, the steam was released to the inner space of the containment building. Thus, more steam was added to the containment than the base case. The steam mass through the ICRV is shown in Figure 11. The overall amount of the released steam through the ICRV was similar to that through the MSSV in the base case (Figure 8). The total released steam mass out of broken SG and intact SG was 200,715 kg and 63,140 kg, respectively. It was almost the same with the steam mass of the base case, 201,259 kg and 62,728 kg from broken SG and intact SG, respectively. There is no significant difference of the steam mass between MSSV and ICRV because the ICRV was modelled with reference to the MSSV. The MSSV and ICRV were opened by pressure difference between the SG and the environment (MSSV) or containment (ICRV). Unlike the environment, the containment pressure increases because of the released

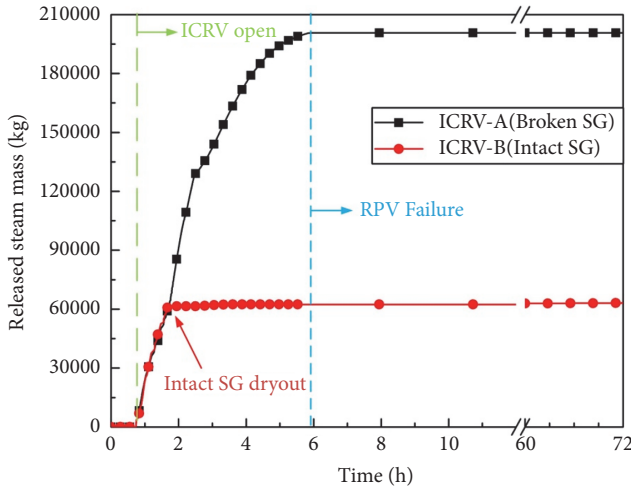


FIGURE 11: Released steam mass through ICRV in the ICRV-CNMT case.

steam from the ICRV. So the released steam mass was only slightly different. Because the intact SG does not have fission product in the SGTR accident, it is no problem that the steam of the intact SG is released to the environment. In this study, however, not only broken SG but also intact SG released steam into the containment for the conservative results. Thus, in the ICRV-CNMT case, total steam of 263,855 kg was added to the containment compared to the base case.

In the ICRV-CNMT case, the results of the system pressure and released steam mass from SGs were almost the same as the base case. However, the released mass of radionuclides to the environment was different between the base case and the ICRV-CNMT case. In the ICRV-CNMT case, there is no release through the MSSV. Thus, the radionuclides were not released to the environment without containment rupture in the ICRV-CNMT case.

Although the radioactive nuclides were not released to the environment in the ICRV-CNMT case, the steam from the secondary system was released into the containment. It caused an increase of the containment pressure by the released steam. To confirm this effect, the containment pressure was calculated and presented in Figure 12. Figure 12(a) shows the containment pressure in the early stage of the accident until 18 h. When the ICRV opened, the pressure increased because of the released steam of the secondary system. However, the pressure of the base case was not increased because the steam was released to the environment until the time of RPV failure. After RPV failure, a large amount of steam and corium were ejected to the cavity, so containment pressure was peaked. The MSSV and the ICRV did not release the steam anymore. However, the containment pressure increased by boiling off the water in the cavity until cavity experienced a dryout. Although the water was completely evaporated, the pressure increased by the molten corium concrete interaction (MCCI), which, in turn, released a large amount of the gases such as noncondensable gases, carbon monoxide, and hydrogen. In addition, the decay heat of ex-vessel corium increased the containment pressure by

the steam expansion in the containment. Finally, the containment pressure was calculated by 0.75 MPa and 1.2 MPa in the base case and the ICRV-CNMT case, respectively, at the 72 h.

3.4. ICRV-RDT Case Simulation. Even if the ICRV-CNMT case did not release the radioactive nuclides to the environment, it caused the containment overpressure. For the effective application of the ICRV, the overpressure needs to be suppressed. Thus, the heat removal of the released steam through the ICRV was investigated in this study. The ICRV is connected to the RDT bottom as shown in Figure 5(c). To condense steam in the water, the model in MELCOR was used. MELCOR 2.1 has bubble physics model in the CVH/FL (Control volume hydrodynamics/Flow path) package [19]. It calculates pool scrubbing with RN (Radionuclide) package in MELCOR using SPARC90 model [20]. In this model, condensate steam mass is calculated using the water depth and subcooling of water. Thus, the RDT water volume was changed and simulated in ICRV-RDT cases. Figure 13 shows that the modelling of the RDT differed by water volume.

In the ICRV-RDT cases, the secondary system released steam to the RDT for the heat exchange with the water in the RDT. It was expected that the RDT water condensates the released steam through ICRV and reduces the containment pressure compared to ICRV-CNMT case. However, the containment pressure of the RDT cases was reduced lower than the ICRV-CNMT case as shown in Figure 14. On the contrary, the containment pressure was increased more than the ICRV-CNMT case. In addition, the effects of the RDT water volume were not confirmed in the containment pressure. These results show that the RDT water alone cannot remove the heat of the steam released through the ICRV. The RDT water mass in each case was the evidence of these results.

Figure 15 shows the water mass of RDT in each case. In Figure 15(b), each case of the ICRV-RDT had different water mass of the RDT. Nevertheless, overall tendency is that decreased mass was the same in each case. In the ICRV-RDT-18 m³ case, the water mass rapidly decreased in the early stage unlike the other ICRV-RDT cases. Because the water level of the RDT reached the flow path location, the water spilled over. This phenomenon was not seen in the other ICRV-RDT cases because flow path is far to the surface of water pool.

Compared to the ICRV-CNMT and the base case, the ICRV-RDT case has much transition in the RDT water mass. In Figure 15(a), in the base and the ICRV-CNMT case, the water mass was not changed with time. This is because the steam from the SG was not released into the RDT and so the water mass in the RDT was not changed. On the other hand, the RDT water mass increased slightly after ICRV opened in the ICRV-RDT case by condensation of the steam. Then the RDT water mass decreased rapidly after PSRV opened. At this time, the pressure was reached at the RDT rupture disk break pressure. So the water in the RDT was released to the outside of the RDT. After the time of RPV failure, the release through the PSRV and ICRV was stopped. Thus, the drastic decrease of the RDT water was almost stopped at this time. However, the water of RDT was boiled by the decay heat of the ex-vessel corium and it was accelerated after cavity dryout.

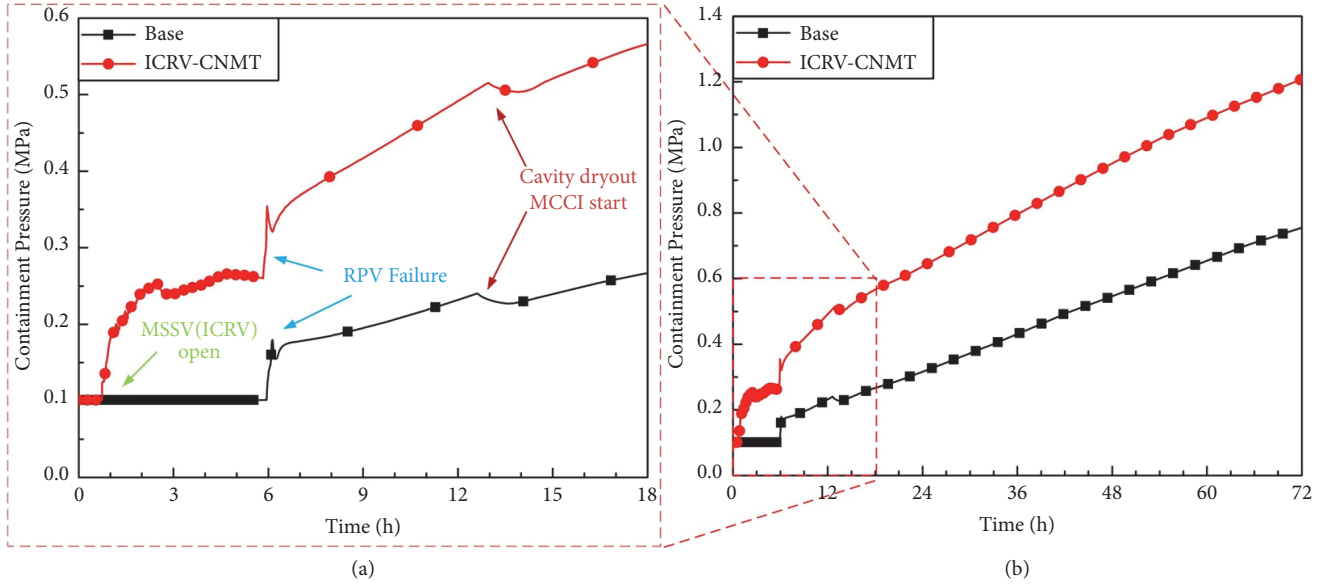


FIGURE 12: Comparison of containment pressure: (a) first 18 hours; (b) full 72 hours.

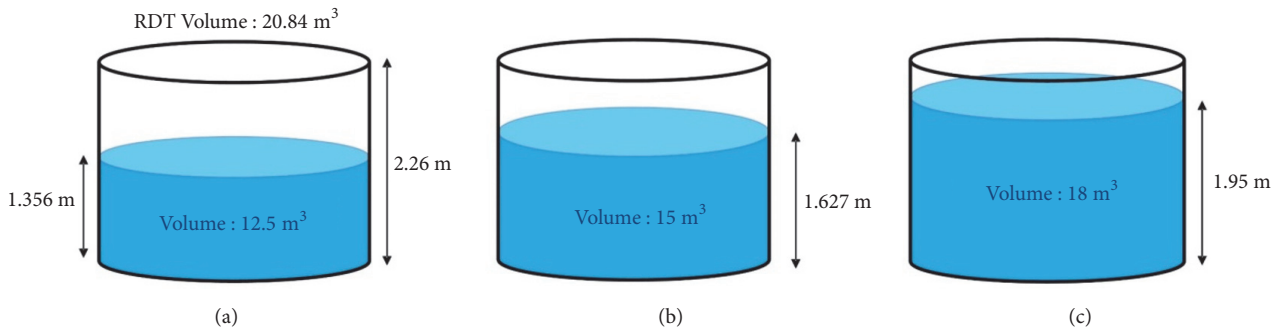
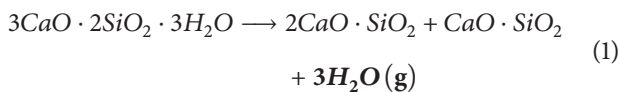


FIGURE 13: The different water volume in the RDT in each case: (a) 12.5 m³, (b) 15 m³, and (c) 18 m³.

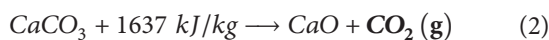
This boiled water of the RDT causes higher pressure in the ICRV-RDT case than the ICRV-CNMT case. Therefore, the depressurization strategy using the RDT is ineffective to the ICRV.

3.5. The Effects of the Cavity Flooding. In the latter period of accident, the overpressure of the containment was caused by two reasons, the heat of the ex-vessel corium and gas generated by MCCI. After the time of RPV failure, the corium was relocated into the cavity which consists of concrete. Then, the massive heat of the corium decomposed the concrete as follows [21, 22].

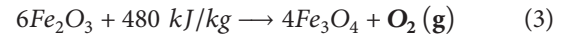
Dehydration of hydrates (100-850°C):



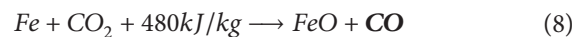
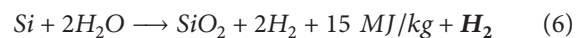
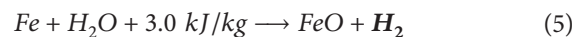
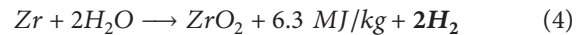
Decomposition of calcium carbonate (600-900°C):



Decomposition of hematite into magnetite (1462°C):



These gases generated by concrete decomposition interact with the corium in the cavity. The reactor core consists of uranium dioxide, zirconium in the cladding, and so on. These materials can react with the steam of high temperature as follows [23, 24]:



These reactions are oxidation reaction of the metal in the corium. Finally, these MCCI gases caused the containment

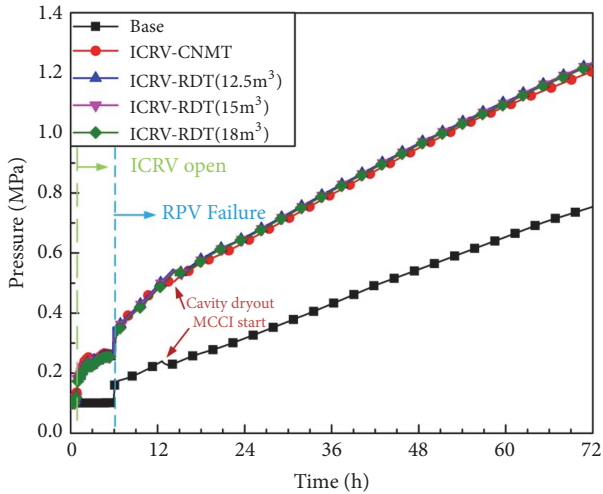


FIGURE 14: Comparison of containment pressure with the base case, the ICRV-CNMT case, and the ICRV-RDT cases.

pressure to be increased. In addition, the decay heat of the ex-vessel corium increases the containment pressure. In this study, the decay heat was calculated by ANS model in the MELCOR [25]. The decay heat of corium expanded the steam in the containment building, and it caused the overpressure of the containment. To diminish these causes of overpressurization, cavity flooding was performed using low-pressure safety injection (LPSI) in this study.

To confirm the effects of cavity flooding, the containment pressure was presented in Figure 16. The cavity flooding was activated from 64,800 s to 72,300 s and the water of RWT injected almost 425,000 kg. When the cavity flooding started, the containment pressure decreased by heat removal of the cavity flooding. The pressure was reincreased by the ex-vessel corium. Finally, the containment pressure reached 0.53 MPa and 0.8 MPa in the base-cavity flooding case and the ICRV-CNMT-cavity flooding, respectively. Although it is not low pressure, ultimate containment failure pressure of OPR1000 with 5% probability at 95% confidence level is 1.01 MPa [26]. Therefore, the cavity flooding method is potentially successful as a depressurization strategy because it reduced the containment pressure from 1.2 MPa to 0.8 MPa in the ICRV-CNMT case. Certainly, the depressurization of the cavity flooding was confirmed. However, the effect of depressurization was different with the base case and the ICRV-CNMT case. The pressure was reduced to 0.22 MPa and 0.4 MPa in the base case and the ICRV-CNMT case, respectively, by cavity flooding. It was caused by the difference of the condensate water mass in containment.

Figure 17 shows the steam mass in the containment. In the ICRV-CNMT cases, the steam mass was increased after ICRV open. However, the steam mass in the containment was not the same as released steam mass through ICRV (Figure 11). It is because the released steam was condensed by the structure in containment such as containment wall. After the RPV failure, the steam mass increased by water boiling in the cavity. The steam production rate was steeper in the ICRV cases than the base case because the condensed water

before the RPV failure was collected in the cavity in the ICRV cases. These increases were stopped at the cavity dryout, but the MCCI occurred and the steam was generated by concrete decomposition (see (1)). When the cavity flooding occurs, the steam mass in the containment decreased in the cavity flooding cases. In the ICRV-CNMT case, more steam existed in the containment than the base case. Thus, the cavity flooding can interact with more steam, and it caused more reduced steam mass. These differences caused the pressure difference between the base case and the ICRV-CNMT case.

Besides the effect of the decay heat, the MCCI gas affects the containment pressure. Figure 18 shows the total mass of gases generated by MCCI. After RPV failure, little gases were generated by MCCI but the water in the cavity suppressed MCCI until cavity dryout. Then the MCCI occurred and the gases were generated by MCCI. After cavity flooding, the generation of gases was relaxed due to delayed MCCI by heat removal. Although the MCCI gas mass was reduced by the cavity flooding, it cannot explain the difference of the decrement between the base case and the ICRV-CNMT case. Therefore, the pressure difference between the base and ICRV-CNMT cases exists because of the steam in the containment building, not MCCI gas.

After 72 hours of accidents in Figure 18, the mass of MCCI gas reached approximately 60,000 kg in the base and the ICRV-CNMT cases. In the MELCOR simulation, the MCCI gas consists of CO_2 , CO , H_2O , and H_2 . It is generated by concrete decomposition reactions ((1) to (3)) or corium oxidation reactions ((2) to (9)). The decay heat of the corium participates in decomposing the concrete, whose example is shown in (3). If the heat transferred to the concrete is totally consumed during chemical reaction of hematite into magnetite ((3)), the CO_2 mass generation rate can be calculated as follows:

$$\frac{Q - Q_{sen}}{\Delta H} = \dot{m} \quad (Q_{sen} = mC_p\Delta T) \quad (10)$$

Q is the heat transferred from the corium to the concrete and Q_{sen} is the sensible heat of the concrete. ΔH is the enthalpy of concrete decomposition. \dot{m} is mass generation rate of CO_2 gas. C_p and m are the specific heat and mass of the concrete, respectively. ΔT is temperature difference between reaction and initial temperature. The decay heat transferred to the concrete is shown in Figure 19 in the base and ICRV-CNMT cases. By using (10), CO_2 generation is calculated as 39,000 kg for 72 hours. However, this approach yields a rough estimate of the MCCI gas. If the other chemical reactions were considered all together, it may reach to 60,000 kg of the MCCI gas in Figure 18. Similar result could be found in MAAP4 calculation [27].

4. Conclusions

The conceptual design of the ICRV was investigated using the MELCOR code in SGTR scenario. The steam of the secondary system was released to the upper dome and the RDT using ICRV. The released mass of the radionuclides was analyzed, and containment pressure was compared in the several explored cases. In addition, the cavity flooding

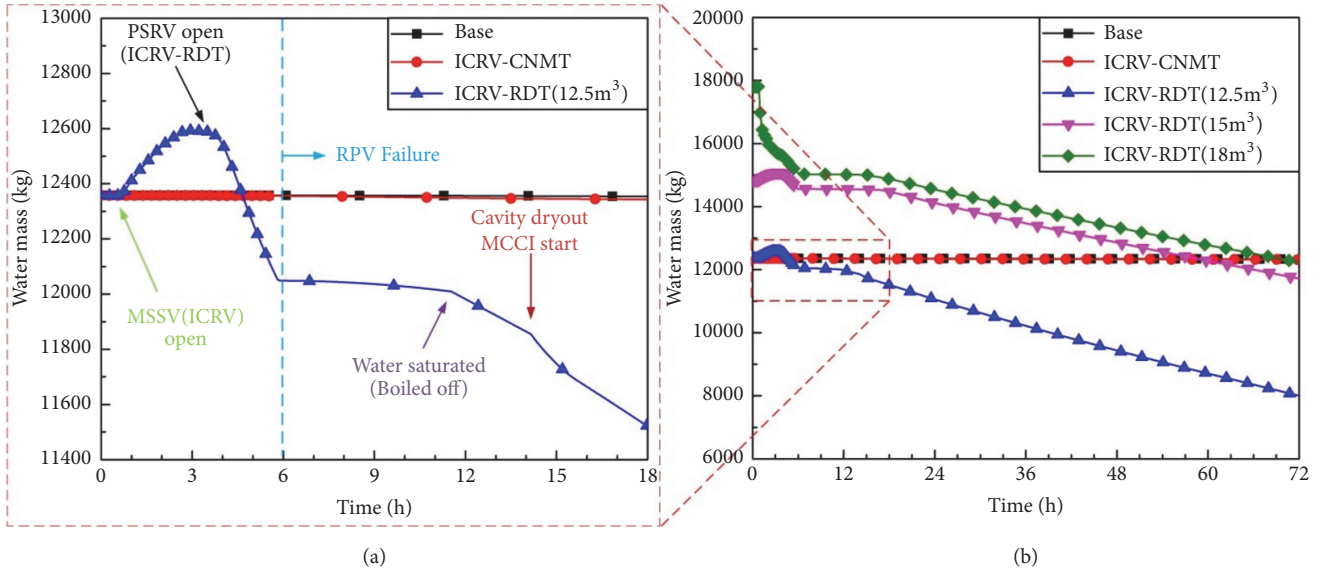


FIGURE 15: The water mass of the RDT in each case.

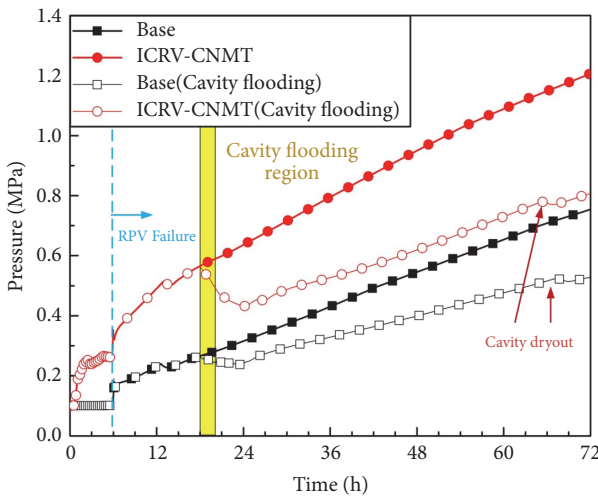


FIGURE 16: The effect of cavity flooding in the containment pressure.

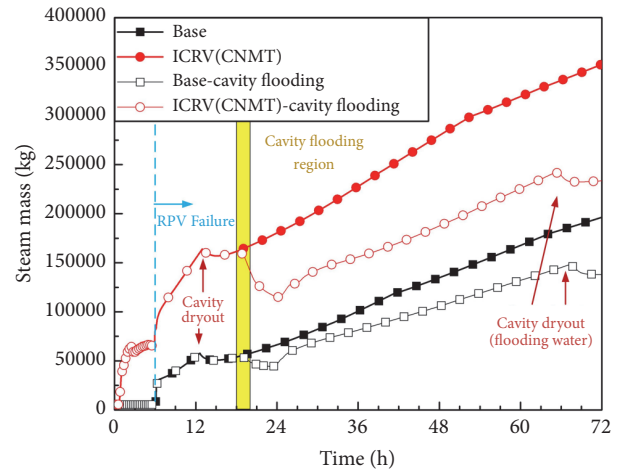


FIGURE 17: The steam mass of cavity flooding in containment.

was performed to reduce the adverse effect of ICRV. Major findings in this study and future work can be summarized as follows:

- (i) The radionuclides were released to the environment through MSSV in the base case. On the other hand, the in-containment relief valve prevents the release of the radionuclides to the environment.
- (ii) As the adverse effect of ICRV, the release steam through ICRV increases pressure in containment building. And it reached 1.2 MPa, which is higher than 0.75 MPa of the base case pressure.
- (iii) To reduce the adverse effect of ICRV, depressurization strategy in which the ICRV was connected to RDT was conducted. But it was ineffective because the capacity of the water in the RDT did not satisfy the release steam from steam generator.

(iv) The overpressure which is adverse effect of the ICRV can be reduced by cavity flooding. The decay heat removal of the cavity flooding causes the depressurization with the steam condensation. The cavity flooding decreased the containment pressure from 1.2 MPa to 0.8 MPa in the ICRV case.

(v) In the future work, the sensitivity of the specification of ICRV and effects of other safety features should be investigated.

Nomenclature

- ADV: Atmospheric dump valve
- AFW: Auxiliary feed water
- CET: Core exit temperature
- CNMT: Containment
- CVH: Control volume hydrodynamics
- FL: Flow path

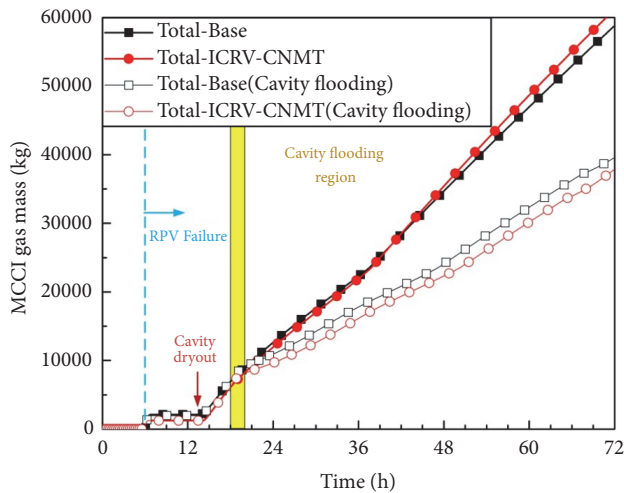


FIGURE 18: The gases mass generated by MCCI in the cases with/without cavity flooding.

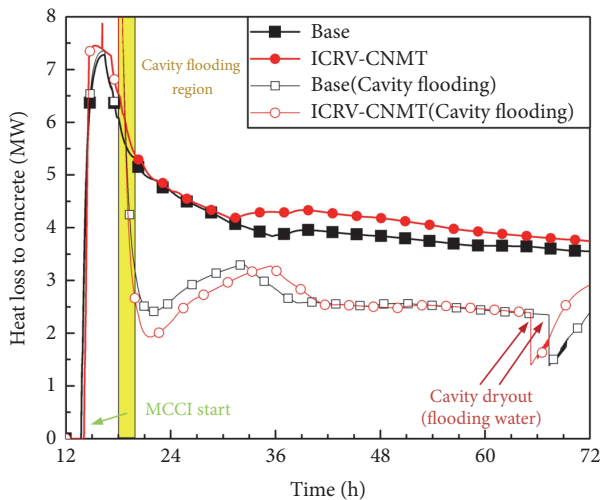


FIGURE 19: The corium heat loss to concrete in the cases with/without cavity flooding.

- FSAR: Final Safety Analysis Report
- HPSI: High-pressure safety injection
- ICRV: In-containment relief valve
- ISLOCA: Interfacing system loss of coolant accident
- LPSI: Low-pressure safety injection
- LWR: Light water reactor
- MCCI: Molten corium concrete interaction
- MSSV: Main steam safety valve
- NPPs: Nuclear Power Plants
- PAR: Passive autocatalytic recombiner
- PSRV: Pressurizer safety relief valve
- RCS: Reactor coolant system
- RDT: Reactor drain tank
- RN: Radionuclides
- RWT: Refuelling water tank
- SBLOCA: Small break loss of coolant accident
- SBO: Station blackout

- SDS: Safety depressurization system
- SG: Steam generator
- SGTR: Steam generator tube rupture
- SITs: Safety injection tanks
- TDAFW: Turbine-driven auxiliary feed water
- TLOFW: Total loss of feed water.

Data Availability

The data used to support the findings of this study are available from the corresponding author upon request.

Conflicts of Interest

The authors declare that there are no conflicts of interest regarding the publication of this paper.

Acknowledgments

This work was supported by the National Research Foundation of Korea (NRF) funded by the Ministry of Science & ICT (MSIT, Korea) [Grants nos. NRF-2017M2A8A4018213 and NRF-2017M2B2A9A02049735].

References

- [1] USNRC, *Containment Integrity Research at Sandia National Laboratories: An Overview* NUREG/CR-6906, Sandia National Laboratories, 2006.
- [2] J. W. Yang, *PWR Dry Containment Issue Characterization* NUREG/CR-5567, Brookhaven National Laboratory, 1990.
- [3] USNRC, *Reactor Safety Study: An Assessment of Accident Risks in U.S. Commercial Nuclear Power Plants* WASH-1400 NUREG-75/014, NTIS, 1975.
- [4] N. K. Kim, J. Jeon, W. Choi, and S. J. Kim, “Systematic hydrogen risk analysis of OPR1000 containment before RPV failure under station blackout scenario,” *Annals of Nuclear Energy*, vol. 116, pp. 429–438, 2018.
- [5] USNRC, *Severe Accident Risks: An Assessment for Five U.S. Nuclear Plants*, NUREG-1150, NTIS, 1975.
- [6] D. Kelly, J. Auflick, and L. Haney, “Assessment of ISLOCA risk-methodology and application to a combustion engineering plant,” Tech. Rep. NUREG/CR-5745, 1992.
- [7] W. Choi, H.-Y. Kim, R.-J. Park, and S. J. Kim, “Effectiveness and adverse effects of in-vessel retention strategies under a postulated SGTR accident of an OPR1000,” *Journal of Nuclear Science and Technology*, vol. 54, no. 3, pp. 337–347, 2017.
- [8] S. Han, T. Kim, and K. Ahn, “An Improvement of Estimation Method of Source Term to the Environment for Interfacing System LOCA for Typical PWR Using MELCOR code,” *Journal of Radiation Protection and Research*, vol. 42, no. 2, pp. 106–113, 2017.
- [9] Y. Jin, S.-Y. Park, and Y.-M. Song, “Application of severe accident management guidance in the management of an SGTR accident at the Wolsong plants,” *Nuclear Engineering and Technology*, vol. 41, no. 1, pp. 63–70, 2009.
- [10] USNRC, *Consequential SGTR Analysis for Westinghouse and Combustion Engineering Plants with Thermally Treated Alloy 600 and 690 Steam Generator Tubes*, NUREG-2195, 2016.
- [11] Y. Liao and K. Vierow, “Melcor analysis of steam generator tube creep rupture in station blackout severe accident,” *Nuclear Technology*, vol. 152, no. 3, pp. 302–313, 2005.

- [12] L. L. Humphries, V. G. Figueroa, M. F. Young, D. Louie, and J. T. Reynolds, "MELCOR Computer Code Manuals Volume 1: Primer and Users' Guide," Tech. Rep. SAND2015-6691R, 2015.
- [13] R. O. Gauntt, N. E. Bixler, and K. C. Wagner, "An uncertainty analysis of the hydrogen source term for a station blackout accident in Sequoyah using MELCOR 1.8.5," Tech. Rep. SAND2014-2210, 2014.
- [14] J. Carbajo, "Severe accident source term characteristics for selected Peach Bottom sequences predicted by the MELCOR Code," Tech. Rep. NUREG/CR-5942, 1993.
- [15] K.-I. Ahn and S.-Y. Park, "Development of a risk-informed accident diagnosis and prognosis system to support severe accident management," *Nuclear Engineering and Design*, vol. 239, no. 10, pp. 2119–2133, 2009.
- [16] S.-Y. Park and K.-I. Ahn, "SAMEX: A severe accident management support expert," *Annals of Nuclear Energy*, vol. 37, no. 8, pp. 1067–1075, 2010.
- [17] KHNP (Korea Hydro & Nuclear Power corporation), *Shin Kori 1&2 Final Safety Analysis Report 2008*, 2008.
- [18] M. J. Wang, W. Tian, S. Qiu, G. Su, and Y. Zhang, "An evaluation of designed passive Core Makeup Tank (CMT) for China pressurized reactor (CPR1000)," *Annals of Nuclear Energy*, vol. 56, pp. 81–86, 2013.
- [19] L. L. Humphries, V. G. Figueroa, M. F. Young, D. Louie, and J. T. Reynolds, "MELCOR Computer Code Manuals," Tech. Rep. SAND2015-6692R, 2015.
- [20] P. Owczarski and K. Burk, "SPARC-90: A code for calculating fission product capture in suppression pools," Tech. Rep. NUREG/CR-5765, 1991.
- [21] KHNP (Korea Hydro & Nuclear Power corporation), *Probabilistic safety assessment of Wolsung unit 1*, 2007.
- [22] Z. P. Bazant and M. F. Kaplan, *Concrete at high temperatures: Material Properties and Mathematical Models*, Essex: Longman Group, 1996.
- [23] M. W. Chase, "NIST-JANAF Thermochemical Tables., , Parts I and II, pp," in *Journal of Physical and Chemical Reference Data*, 4th edition, 1952.
- [24] T. Sev and E. Facility, "Molten Core - Concrete Interactions in Nuclear Accidents Theory and Design of an Experimental Facility," *VTT*, p. 14, 2005.
- [25] American Nuclear Society Standards Committee Working Group ANS-5.1, *American National Standard for Decay Heat Power in Light Water Reactors*, ANSI/ANS-5.1, American Nuclear Society, 1979.
- [26] S.-W. Lee, T.-H. Hong, Y.-J. Choi, M.-R. Seo, and H.-T. Kim, "Containment depressurization capabilities of filtered venting system in 1000 MWe PWR with large dry containment," *Science and Technology of Nuclear Installations*, vol. 2014, Article ID 841895, 10 pages, 2014.
- [27] Nan Jiang, Minjun Peng, Wei Wei, and Tenglong Cong, "Strategy Evaluation for Cavity Flooding during an ESBO Initiated Severe Accident," *Science and Technology of Nuclear Installations*, vol. 2018, Article ID 8680406, 15 pages, 2018.

Research Article

Modelling of Severe Accident and In-Vessel Melt Retention Possibilities in BWR Type Reactor

Mindaugas Valinčius , **Tadas Kaliatka** , **Algirdas Kaliatka**, and **Eugenijus Ušpuras** 

Laboratory Of Nuclear Installation Safety, Lithuanian Energy Institute, Breslaujos St. 3, LT-44403 Kaunas, Lithuania

Correspondence should be addressed to Mindaugas Valinčius; mindaugas.valincius@lei.lt

Received 23 March 2018; Revised 15 June 2018; Accepted 15 July 2018; Published 1 August 2018

Academic Editor: Sevostian Bechta

Copyright © 2018 Mindaugas Valinčius et al. This is an open access article distributed under the Creative Commons Attribution License, which permits unrestricted use, distribution, and reproduction in any medium, provided the original work is properly cited.

One of the severe accident management strategies for nuclear reactors is the melted corium retention inside the reactor pressure vessel. The work presented in this article investigates the application of in-vessel retention (IVR) severe accident management strategy in a BWR reactor. The investigations were performed assuming a scenario with the large break LOCA without injection of cooling water. A computer code RELAP/SCDAPSIM MOD 3.4 was used for the numerical simulation of the accident. Using a model of the entire reactor, a full accident sequence from the large break to core uncover and heat-up as well as corium relocation to the lower head is presented. The ex-vessel cooling was modelled in order to evaluate the applicability of RELAP/SCDAPSIM code for predicting the heat fluxes and reactor pressure vessel wall temperatures. The results of different ex-vessel heat transfer modes were compared and it was concluded that the implemented heat transfer correlations of COUPLE module in RELAP/SCDAPSIM should be applied for IVR analysis. To investigate the influence of debris separation into oxidic and metallic layers in the molten pool on the heat transfer through the wall of the lower head the analytical study was conducted. The results of this study showed that the focusing effect is significant and under some extreme conditions local heat flux from reactor vessel could exceed the critical heat flux. It was recommended that the existing RELAP/SCDAPSIM models of the processes in the debris should be updated in order to consider more complex phenomena and at least oxide and metal phase separation, allowing evaluating local distribution of the heat fluxes.

1. Introduction

Nuclear energy is currently counting more than half of a century of its existence. That being said, the technology still keeps advancing and evolving, eliminating more and more safety issues in the nuclear power plants (NPP). However, even extremely rare, severe accidents in NPP must be very carefully investigated, so that consequences would be mitigated in case of such an unlikely event. After the accident in the Fukushima NPP, the whole viewpoint of the nuclear energy organizations including International Atomic Energy Agency has changed and current safety standards require that severe accidents must be covered in the design extension conditions and that must be within the design envelope.

In case of a severe accident, one of the severe accident management strategies for nuclear reactors is the melted corium retention inside the reactor pressure vessel (RPV). The In-Vessel Retention (IVR) of molten corium by external

cooling of the vessel lower head was introduced about 25 years ago [1]. It was first applied to two designs of reactors: AP600 [2] and VVER-440 [3]. The VVER-440 case has led to a practical application at the Loviisa plant where IVR is a part of the severe accident management. The AP600 design was not further developed as it was later replaced with the AP1000 design [4], keeping the option of IVR. In parallel, other designs involving IVR were examined, such as APR-1400 [5, 6], SWR-1000 (BWR type, also known as KERENA) [7], and VVER-640 [8]. The concept is also considered for the recent Chinese design CPR-1000.

The IVR strategy is very attractive for several reasons. It ensures that corium is maintained in the vessel, avoiding the presence of large masses of radioactive materials in the containment and the risks of failure of the containment. In principle, external cooling of the vessel appears to be able to extract enough power and is suitable for long-term stabilization of corium. Also the practical design, under its

TABLE 1: General data of BWR-5 [14–16].

| Parameter | Value |
|----------------------------|---|
| Control | 109 control rods of SS with Boron carbide or Boron carbide plus Hafnium. Total mass 580 kg. |
| Fuel | 444 fuel assemblies. Matrix 8x8 with 2 water rods. Active core length 3.58 m. Number of fuel rods per assembly 62 |
| Pressure | 6.93 MPa nominal |
| Power (thermal) | 2029 MW _t |
| Steam flow | 1100 kg/s |
| Recirculation pumps | 2 |
| Recirculation nominal flow | 2565 kg/s |
| Feed water flow | 1097 kg/s |
| Number of jet pumps | 20 |
| Vessel | Made of carbon steel, internally clad with stainless steel; Total height; 20.8 m, diameter 5.30 m; thickness from 0.13 to 0.19 m; |
| Lower head | radius (cylindrical part) = 2.71 m; thickness (cylindrical part) = 0.19 m; radius (hemispherical part) = 2.87 m; thickness (hemispherical part) = 0.19 m; heat surface (hemispherical part) = 38.5 m ² ; |
| Mass of Zircaloy | Total mass in the core 27045 kg. Claddings 20745 kg Control rods and fuel boxes 6300 kg |

simplest form, appears less expensive than an external core-catcher.

Although this IVR strategy is not new, its potential is still not fully investigated. In order to consolidate the results of these investigations, perform additional studies for the missing parts, and explore the possibilities of IVR in more detail, the HORIZON 2020 project In-Vessel Melt Retention Severe Accident Management Strategy for Existing and Future NPPs (IVMR) [9] was initiated.

The main objective of this article is to investigate various modes of ex-vessel heat transfer and to make a comparison between them. A numerical study of severe accident in the nuclear reactor and the analysis of corium retention inside the reactor pressure vessel are presented. A full plant model of a ~2000 MW thermal power BWR reactor was used and large break Loss of Coolant Accident (LOCA) with total failure of cooling water injection was assumed. Full accident sequence from normal operation conditions to core heat-up, melting, and relocation into lower head was modelled. The ex-vessel cooling was investigated with the available options of the heat transfer modes in the RELAP/SCDAPSIM computer code.

2. Selection of Accident Scenario for the Analysis

The analysis of IVR strategy for BWR type NPP is performed in the frame of IVMR project. As a basis for the analysis the generic BWR model of General Electric BWR-5 reactor installed in Mark-II containment, developed in the frame of the international SCDAP Development and Training

Program (SDTP) [11–13], was used. The most important features of this modelled generic BWR-5 reactor are presented in the Table 1.

The general practice suggests that in the safety analysis the worst case scenario should be investigated. For a BWR type reactor, a scenario with the large break LOCA is considered to lead to the worst consequences in the shortest time. In this study, a guillotine break of external circulation pump suction pipe, LOCA without injection of cooling water due to the failure of the Emergency of Core Cooling Systems (ECCS), is considered. The main assumptions for this scenario are as follows: at time moment $t = 0$ s reactor is shut down (SCRAM'ed), main coolant pumps are tripped, and main steam Isolation valves are closed; cooling water are not supplied during all accident scenario. This is a hypothetical scenario in order to cause the fast core melt and observe the slumping of melted materials to the lower head, which leads to heating of the bottom of the RPV. The containment is modelled and external cooling of the reactor vessel is considered. The technical measures for supplying the water into the reactor cavity are not analyzed in this study. It was assumed that the cavity is filled before the meltdown and slumping of the melted materials into the reactor lower head.

3. RELAP/SCDAPSIM Model Description

The RELAP/SCDAPSIM computer code is widely used in the world to simulate the severe accidents [17, 18]. Computer code consists of three separate modules: RELAP5 calculates thermal hydraulics, SCDAP calculates core heat-up,

oxidation, and degradation, and COUPLE is used to calculate the heat-up of reactor core material that slumps into the lower head of the RPV. The COUPLE module solves two-dimensional, finite-element based heat transfer problem. This module takes into account the decay heat and initial internal energy of slumped debris and then calculates the transport by conduction of this heat in the radial and axial directions to the wall structures and water surrounding the debris. The COUPLE module solves the following two-dimensional energy equation:

$$(1 - \varepsilon) \rho_D c_D \frac{\partial}{\partial t} (T) = \frac{\partial}{\partial x} \left(k_e \frac{\partial T}{\partial x} \right) + \frac{\partial}{\partial y} \left(k_e \frac{\partial T}{\partial y} \right) + Q \quad (1)$$

where ρ_D is density of debris particles (kg/m^3); c_D is heat capacity of debris particles ($\text{J/kg}\cdot\text{K}$); k_e is effective thermal conductivity ($\text{W/m}\cdot\text{K}$); Q is volumetric heat generation rate (W/m^3); T is temperature of mixture of debris and interstitial fluid (K); ε is porosity (pore volume/total volume).

The RELAP/SCDAPSIM input deck, which was used for large LOCA simulation in this work, initially was developed by the regulatory body in Mexico (CNSNS) [11, 12] for Laguna Verde NPP in Mexico. The detailed nodalization scheme and explanation of the model is presented in [13]. This input deck was modified, and the ex-vessel model was appended in order to simulate heat transfer through the vessel wall by flooding the reactor cavity and submerging the RPV in water. The supply of feed water, turbine, suppression pool, and control rod drive system are represented by boundary conditions. Four fuel rods channels represent the reactor core and each fuel rod is nodalized with 13 axial nodes to model heat transfer and mass distribution in the core. Boundary conditions that represent the primary containment at constant pressure are fixed to simulate the break-in the recirculation loop with the time-dependent volumes that are connected to the valves. These valves are used to simulate breaks in the recirculation lines (from RPV side and circulation pump side). These valves are open at the beginning of the calculation.

In this work, the heat transfer to the ex-vessel was investigated as a standalone simulation, separated from the full plant simulation. The reason for this separation was to eliminate all the uncertainties arising from the feedback between corium relocation and different mode of vessel cooling, time step, etc. Since the main objective of this work was to investigate various modes of ex-vessel heat transfer and to make a comparison between them. Therefore, the results of a full plant accident scenario simulation were used as an input data for simplified ex-vessel cooling model. The main parameters were the masses, composition, and the decay heat of the corium in the lower head.

Similar model and investigations are presented in [19]. However, in this article, it was reported that for the long-term simulation the problems of the heat transfer in the lower head occurred and calculations of the RELAP/SCDAPSIM code crashed. For our calculations the model was improved. In [19] presented problems were avoided by adjusting the time step ratio between the thermal-hydraulic calculations and 2D finite-element solver for the heat transfer in the lower head and setting it to be equal to 1.

In the RPV ex-vessel model the in-vessel hydrodynamic volume receives the corium slumps, and finite-element mesh is used to calculate the heat transfer from the corium to walls and structures. The convective boundary is then connected to the external surface of the RPV lower head, and the heat from COUPLE finite-element mesh is transferred to hydrodynamic volumes of RELAP5 code, representing the ex-vessel. There are two different modes of ex-vessel in RELAP/SCDAPSIM:

- (a) The first one is RELAP5 based convective heat transfer from the external vessel wall to the hydrodynamic volume. The heat transfer coefficient depends on the flow regime in the hydrodynamic volume, void fraction, and all other parameters. The scheme of this model using this method is shown in Figure 1(a).
- (b) The second is a special ex-vessel model implemented in COUPLE code, which then uses heat transfer as a function of contact angle of a curved downward facing structure, such as RPV lower head. This model using this approach is presented in Figure 1(b).

In the case of the ex-vessel model with RELAP5 heat transfer mode (see Figure 1(a)), the model consists of 2 time-dependent volumes, 2 single volumes, one vertical pipe component, and a time-dependent junction. Time-dependent volumes used in order to give the boundary conditions for the developed model. 2 single volumes are used as the buffering volumes in the model. Vertical pipe component represents the available volume around ex-vessel. Pipe components have 10 internal nodes (see Figure 1(a)). Each node is connected to a separate segment of the COUPLE mesh. In order to have more precise calculation results each node has flow area and height is different, following the shape of the COUPLE the mesh. The height of the first nodes is increasing going from the bottom to the top of the lower head.

In the case of the ex-vessel model with COUPLE heat transfer mode (Figure 1(b)), a heat transfer is described as a function of contact angle. In this case only one hydrodynamic volume can be connected as a heat sink (limitation of the RELAP/SCDAPSIM MOD 3.4 code). COUPLE code then calculates the contact angle by the shape of the mesh and applies the heat flux, according to the temperature difference between the sink and the COUPLE wall. The sink temperature is chosen to be either saturation temperature by the pressure in that volume or 10 K below the saturation temperature. A separate variable is needed for COUPLE to track the water level in the ex-vessel volume. This variable can be set by the user as a constant (e.g., always full), or it can be a function of time or void fraction in ex-vessel volume or any other option chosen by the user. If the node is calculated to be uncovered (e.g., level variable is 1 m, and the node is at the elevation of 1.5 m), the user-defined heat transfer coefficient for dried-out surface is applied.

The correlation for heat transfer in COUPLE ex-vessel model was obtained from US Nuclear regulatory commission (NRC) subscale boundary layer boiling (SBLB) tests (NUREG/CR6507) [20]. The heat flux depending on contact angle and temperature difference (for model illustrated in

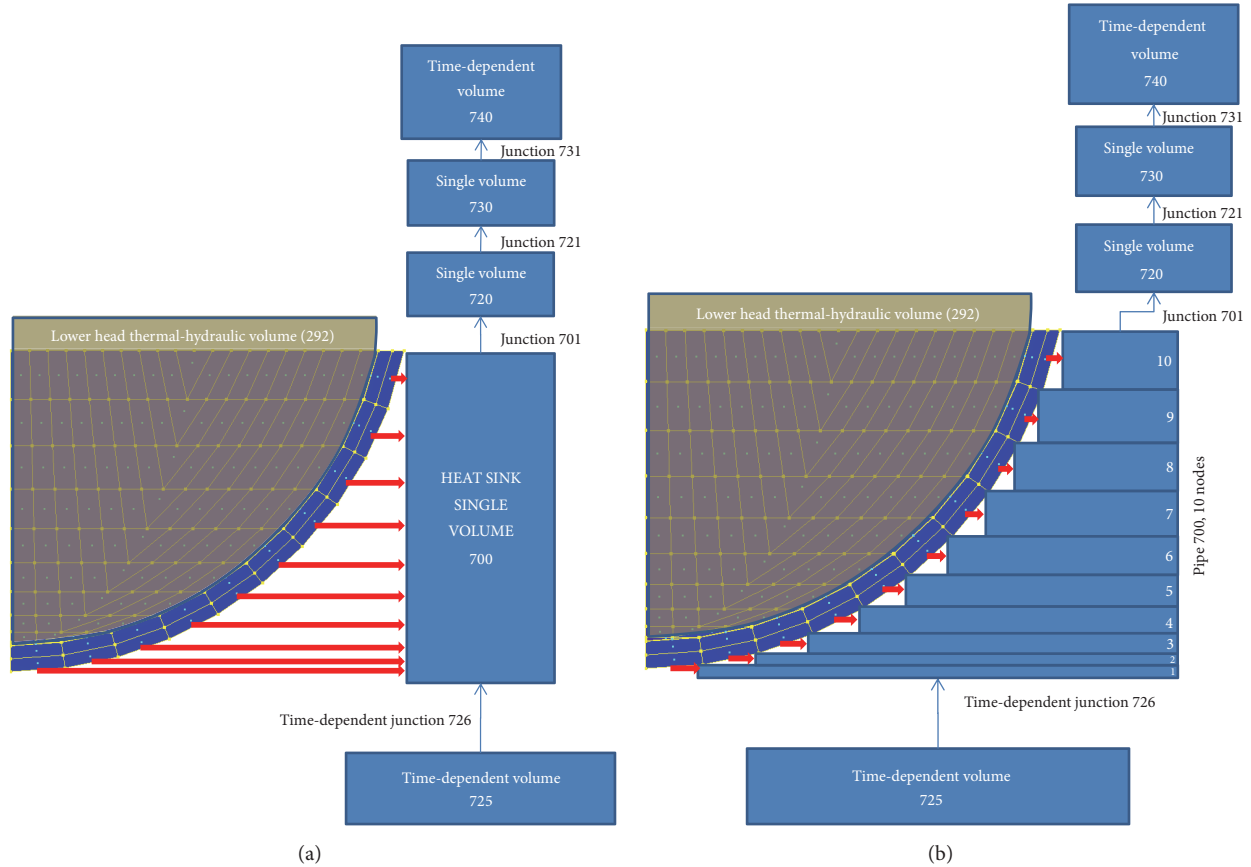


FIGURE 1: Scheme of the COUPLE lower head model with (a) RELAP5 heat transfer; (b) COUPLE heat transfer.

Figure 1(b) is presented in Figure 2. The peak of each curve means that the CHF has been reached, and the CHF value can be read from y -axis.

The analytical equation of critical heat flux as a function of contact angle (θ) and degree of subcooling (ΔT_{sub}) is defined by (2) [10]. This equation is implemented into the COUPLE code, and the user can choose to apply either saturated or $\Delta T_{sub} = 10$ K subcooled conditions. The resulting critical heat flux of both available options under atmospheric conditions is presented in Figure 3. It is obvious from this figure that using the saturated boiling curve is more conservative assumption for the critical heat flux.

$$q_{CHF} = 0.4 \left(1 + 0.021\theta - (0.007\theta)^2 \right) \left(1 + 0.036\Delta T_{sub} \right) \quad (2)$$

where q_{CHF} is critical heat flux (W/m^2); θ is contact angle (deg.); ΔT_{sub} is degree of subcooling (K).

4. Results and Discussion

The objective of the analysis was to investigate the effectiveness of ex-vessel cooling, so that the RPV would stay intact. The main parameter for such evaluation was the wall temperature of the RPV wall. It was assumed that if temperature of the wall reaches the melting temperature of carbon steel (1723 K) the geometry is assumed as melted. The residual wall thickness of the RPV was derived from these

results. It was calculated by assuming linear temperature gradient in the vessel wall and from the initial wall thickness (0,19 m) subtracting the thickness of the wall having higher temperature than melting point.

The accident sequence begins from the steady-state conditions, which are tuned to be as close as possible to the reactor design values. The main operational parameters in steady-state operation before the accident were assumed according to the initial conditions presented in Table 1.

The LOCA occurs at the time = 0 s, and at the same moment the feed-water stops. The failure of emergency water supply was assumed. Reactor emergency shutdown (SCRAM) occurs immediately. The key events of the accident sequence are presented in Table 2.

4.1. Processes in the Core. During the steady state, the heat from the core is transferred to the coolant via boiling. After guillotine break of cold leg (large LOCA), the water is rapidly discharged through the broken pipe and the water level in the RPV decreases. The discharge flow rate through the break and collapsed water level in the reactor core are shown in Figures 4 and 5, respectively. Due to the water loss, the reactor gets depressurized and the behavior of steam dome pressure is presented in Figure 6.

After large LOCA is initiated, the top of active fuel is uncovered in 32 seconds after the break and fully uncovers

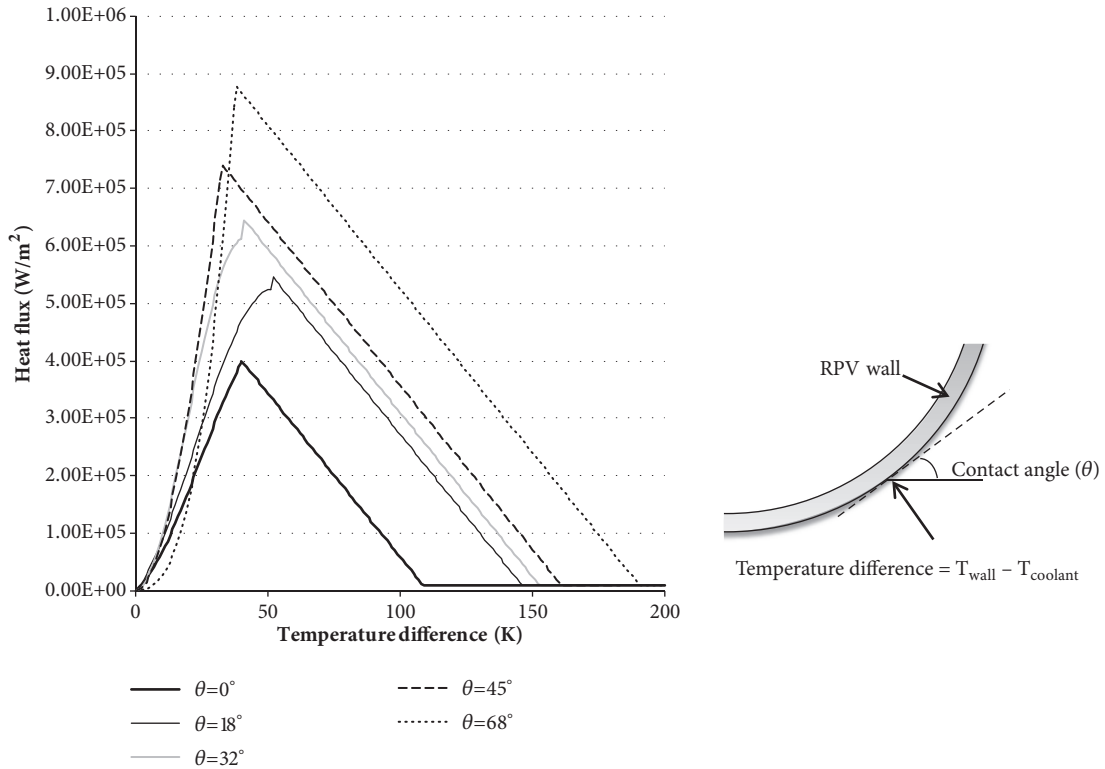


FIGURE 2: Heat flux as a function of temperature difference and contact angle for COUPLE heat transfer under saturated boiling conditions [10].

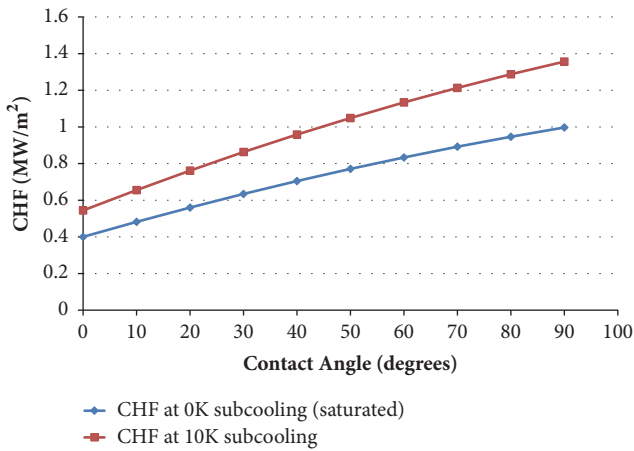


FIGURE 3: Critical heat flux at atmospheric pressure for both subcooling options in COUPLE heat transfer correlation.

in 50 seconds. After the fuel is uncovered, the heat-up of the fuel rods takes place. The peak cladding temperature is shown in Figure 7. The first rupture due to ballooning occurs in 421 s after the accident. In case of no ECCS in operation as it was assumed in our work, the heat-up of the reactor core progresses and ends up with melting of the core materials and relocation of the debris into the lower head.

The relocation of the corium to the lower head starts at $t = 847$ s after beginning of the accident. The drop of significant

TABLE 2: Key events of accident sequence.

| KEY EVENT | TIME (s) |
|---|----------|
| LOCA | 0 |
| Reactor emergency shutdown (SCRAM) initiating (evaluating system delay) | 0.2 |
| Turbine trip initiating | 0.2 |
| Trip of recirculation pumps initiating | 0.3 |
| Core Uncovers/ First heat up of the core | 32 |
| Core fully uncovered | 50 |
| Oxidation onset | 292 |
| $T_{cladding} = 1473$ K (1200°C) | 421 |
| Start of core relocation to lower head | 847 |
| Dry out of the lower head | 3000 |

amount of UO_2 debris into lower head leads to more rapid decrease of the water level (at 2600 s after the beginning of the accident). The remaining water in the lower head (as presented in Figure 5) fully evaporates in 3000 s after the beginning of accident, as it is heated by slumped debris.

4.2. Relocation and Decay Heat of Corium in Lower Head. Melting and relocation of the core begin with the lighter metals, and the earliest slumps of debris contain mainly Fe and B_4C absorber and small quantities of Zr and ZrO_2 . The first slump is observed at 847 s after the beginning

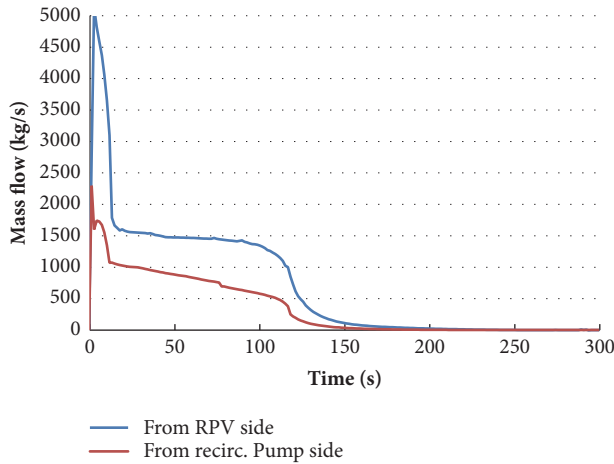


FIGURE 4: Water discharge flow rate through the break (both ends of the pipe).

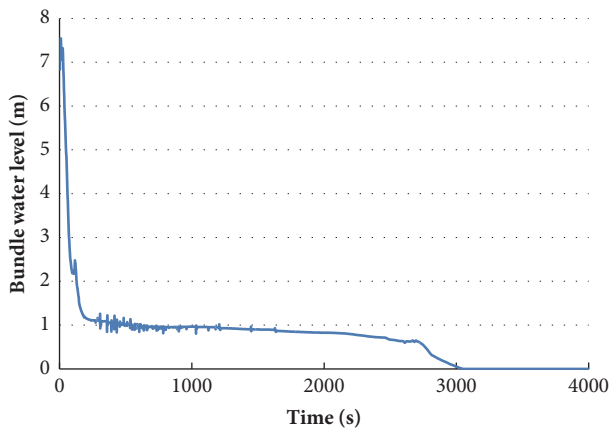


FIGURE 5: Water level in the RPV.

of the accident. The slumping of debris to the lower head by material type is shown in Figure 8. Due to limitations of RELAP/SCDAPSIM MOD 3.4 code, the materials in the lower head takes the positions and stay in the order it was relocated. As slumped materials start melting in the lower head, RELAP/SCDAPSIM treats them as a single homogeneous liquid pool (see Figure 9), with uniform properties. In reality, complex transient processes take place in debris bed and, after stratification, 2- or 3-layer configuration is formed, depending on the debris composition [21] (as shown in Figure 9). In our calculations, since the light metal is the first to slump into the lower head of RPV, these metals (Fe, B₄C) always stay at the bottom. Above this layer, the debris containing Zr, ZrO₂, and UO₂ builds up later. The origin of all the materials is only the reactor core elements, specifically fuel assemblies, control rods, and channel boxes, because RELAP/SCDAPSIM does not have any additional models to include other internal RPV structures (i.e., core plate, control rod guide tubes, and instrumentation tubes in the lower head) into the debris bed. The only structure considered in the model is the RPV wall, but wall ablation is

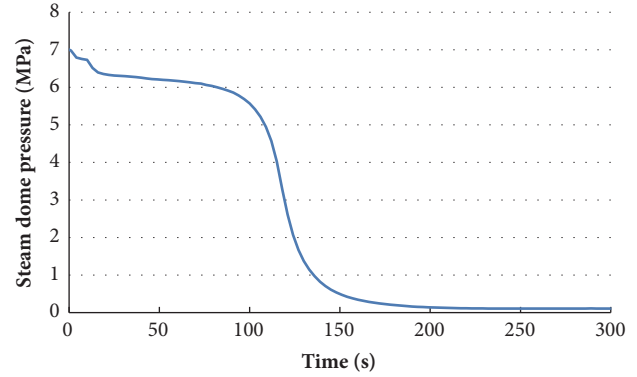


FIGURE 6: Steam dome pressure.

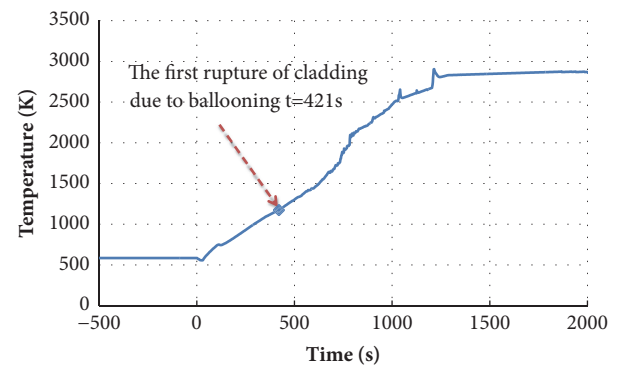


FIGURE 7: Peak cladding temperature of the core.

not considered. The aspect of debris stratification is covered in Section 4.4, where the heat transfer from metal/oxide layers is investigated analytically.

The main task of this analysis is to cope with the decay heat in debris and to achieve proper cooling of the lower head. The decay heat in the reactor core and the corium in the lower head are presented in Figure 10. Each sudden “step” in the chart means that a portion of UO₂ fuel has slumped from the reactor core into the lower head.

4.3. Ex-Vessel Cooling. In our case the reactor cavity outside RPV is assumed to be filled with water before the debris starts slumping into the lower head. The water supply stops after filling the reactor cavity just a bit above the lower head. The total of ~170 m³ of water is needed to reach this level from the bottom of the reactor pit. The accident management actions as water supply after the accident was not in the scope of this analysis.

Although there is no actual mixing of the materials modelled by RELAP/SCDAPSIM, the heat transfer in the debris bed is simulated not only by conduction, but also by convection. RELAP/SCDAPSIM achieves this by calculating the quantity of liquefied debris and treats it like one well-mixed molten pool with uniform power density and melting temperature. This molten pool has the “effective heat transfer

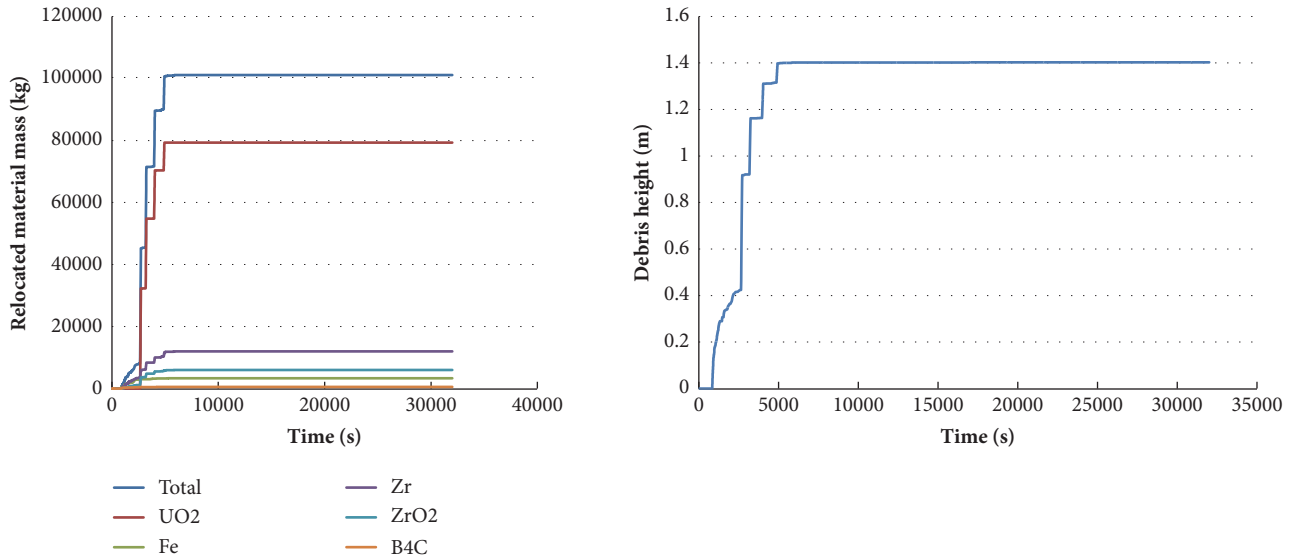


FIGURE 8: Mass of different materials and debris height in the lower head.

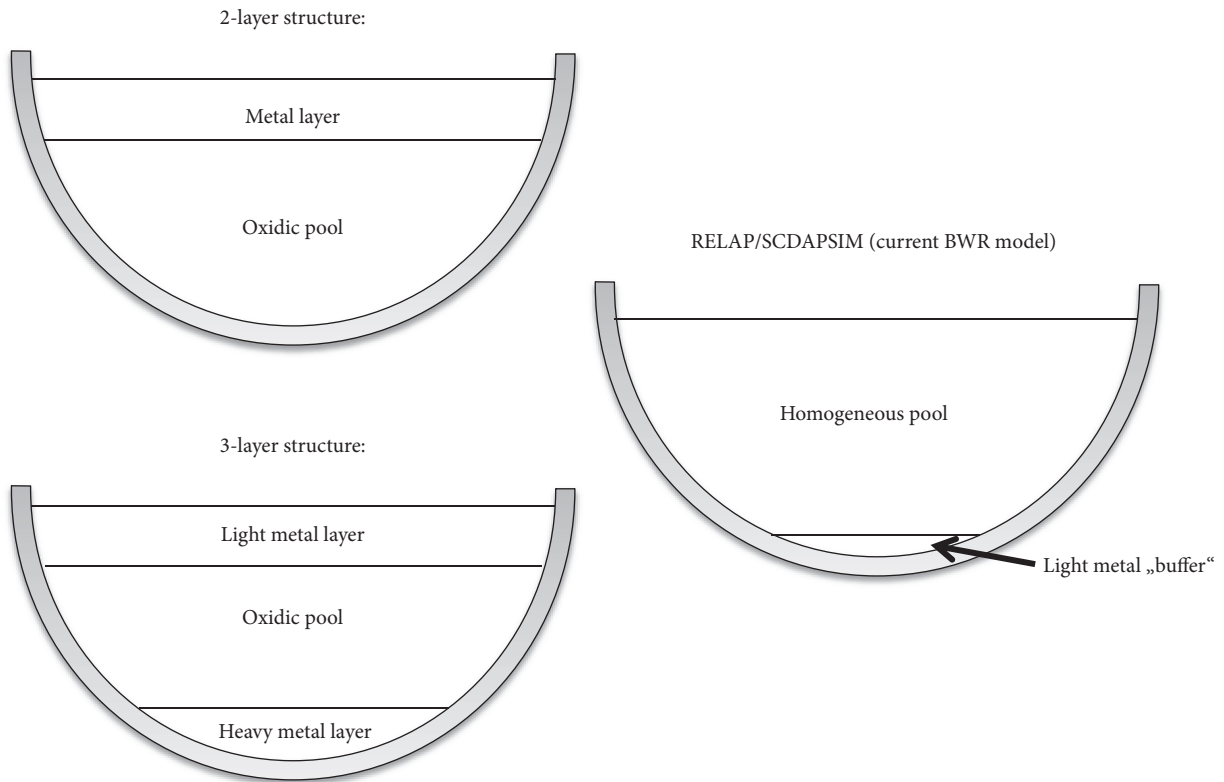


FIGURE 9: Layer formation in debris bed compared to RELAP/SCDAPSIM model.

coefficient”, which is based on the Rayleigh number. The liquefied debris mass calculated by RELAP/SCDAPSIM in comparison with the total debris mass is presented in Figure 11. It can be seen from the figure that the debris bed contains approximately 80000 kg of molten material at around 7000 s after the beginning of the accident. Unfortunately, only one molten pool is considered in current RELAP/SCDAPSIM

MOD 3.4 code version; therefore it cannot model the liquid light metal above the liquid oxidic pool which is a typical situation to have the “focusing effect” [22]. The influence of “focusing effect” is evaluated analytically in Section 4.4.

The temperature of the external RPV wall for all cases is shown in Figure 12. Internal wall temperature is shown in Figure 13. The heat flux from RPV to the water in reactor

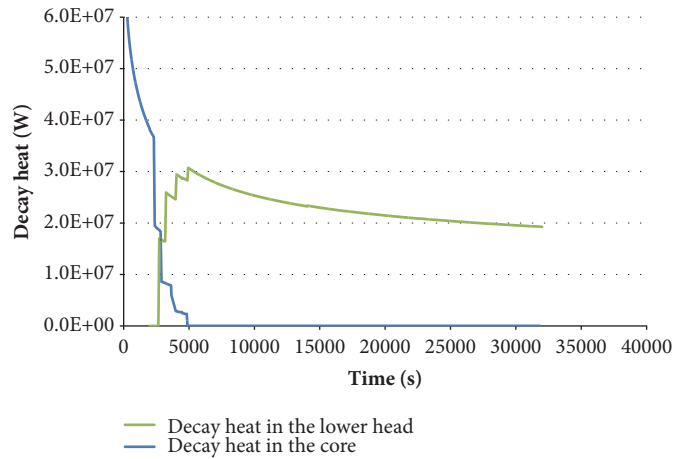


FIGURE 10: Decay heat in the reactor core and the corium in the lower head.

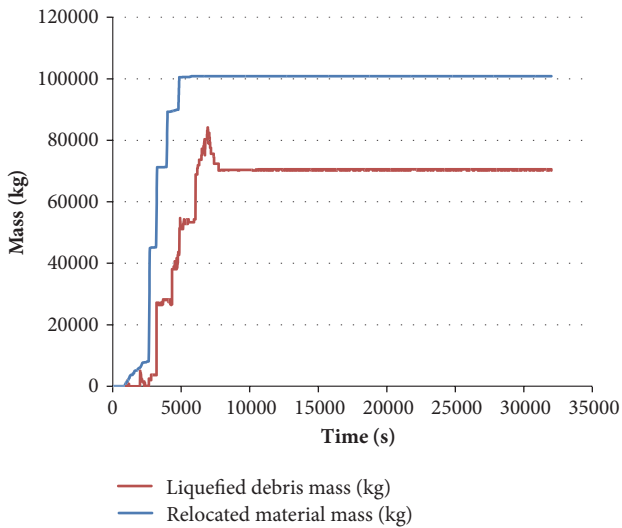


FIGURE 11: Liquefied debris mass in comparison with the total relocated material mass.

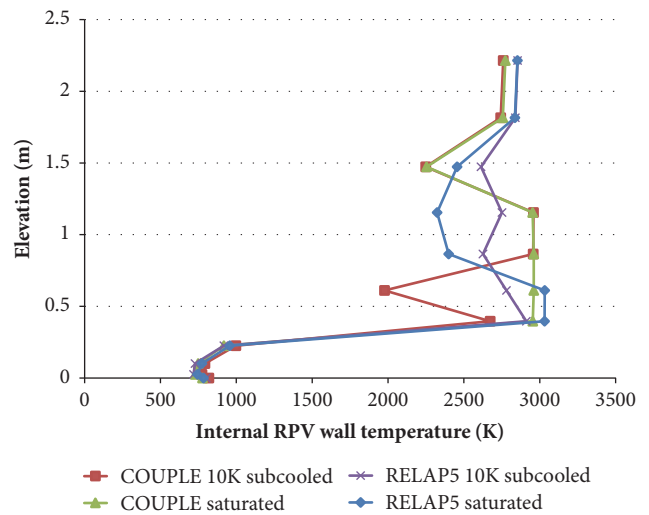


FIGURE 13: Maximum RPV internal wall temperature for each case.

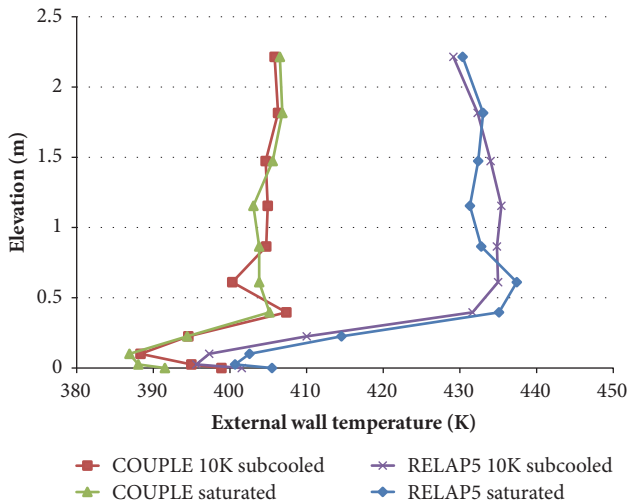


FIGURE 12: Maximum RPV external wall temperature for each case.

cavity is shown in Figure 14. Also, the heat transfer coefficient is presented in Figure 15. The results are presented for the saturated or subcooled boiling using RELAP5 heat transfer mode (model shown in Figure 1(a)) and COUPLE heat transfer mode (model shown in Figure 1(b)).

Calculation results showed that the external surface successfully cooled and CHF is not expected with any of the heat transfer modes. As it is shown in Figure 14 there is a significant margin between CHF (which was calculated by (2)) and the calculated actual heat flux. The results suggest that main factor for the given reactor to achieve success with IVR strategy is to maintain the water level in the reactor pit.

As for the distribution of the heat fluxes/temperature/heat transfer coefficient along the wall, it can be observed that, in both heat transfer modes, heat flux at the bottom of the RPV is the lowest. This is due to the fact that there is no formation of the layers considered in RELAP/SCDAPSIM, and there is a light metal “buffer” (structure of thicker crust without the decay heat) at the bottom of the RPV, Figure 9.

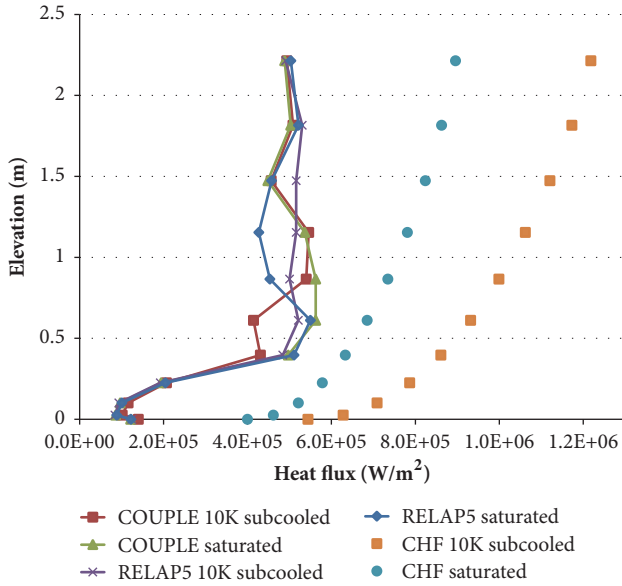


FIGURE 14: Maximum RPV heat flux to the ex-vessel for each case.

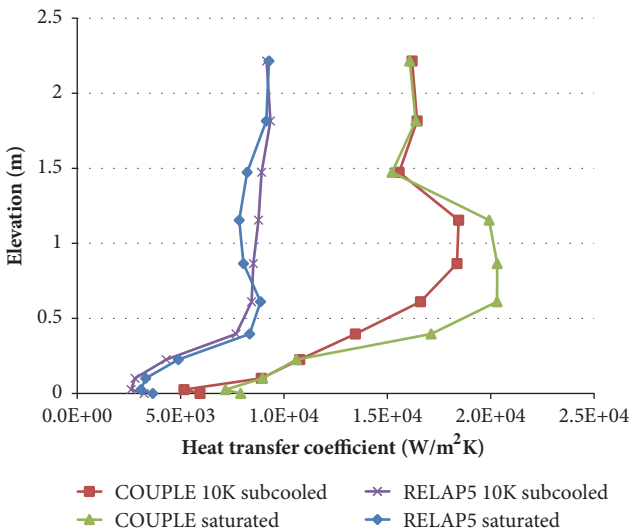


FIGURE 15: Heat transfer coefficient from external wall to ex-vessel volume for each case.

Going upwards along the RPV wall the results show that the COUPLE heat transfer mode is more effective and the heat transfer coefficient is higher (Figure 15). Therefore, the wall temperature (Figure 12) is also lower by around 30 K. The correlations for ex-vessel heat transfer implemented into COUPLE code are based on the experimental results for the shape of RPV lower head, submerged into a pool of water [10]. For this reason, employing the COUPLE based heat transfer mode is strongly recommended for such kind of problems, while RELAP5 calculated heat transfer effectiveness is considered underestimated. The underestimation can be seen in both saturated and 10 K subcooled cases. On the other hand, COUPLE heat transfer mode can be not suitable in some cases, since the HTC in a natural convection is not

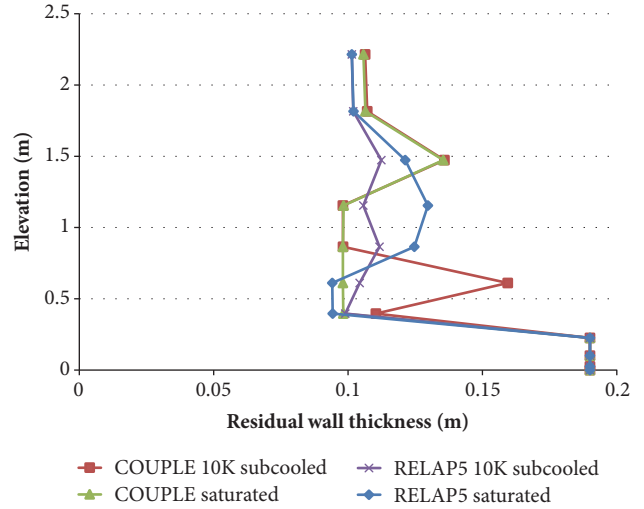


FIGURE 16: Residual wall thickness of the RPV for each case.

only strongly influenced by the shape of the lower head, but also the geometry of the cooling channel (the width, with/without baffle, and RPV coating). These aspects should be considered when applying COUPLE based heat transfer mode.

As it was mentioned at the beginning of Section 4, the main parameter for the RPV integrity would be the residual wall thickness. The results of the analysis are presented in Figure 16. The calculations were performed taking into account external wall temperature (Figure 12) and internal wall temperature (Figure 13) and assuming linear temperature gradient in the wall. As it can be seen from the results, the minimal residual wall thickness is calculated to be around 10 cm, which is sufficient to maintain the integrity of the RPV.

Summarizing the results it may be concluded that currently the RELAP/SCDAPSIM computer code can evaluate the effectiveness of IVR strategy only in case of the homogeneous debris bed (as it is presented in Figure 9). The correlations for heat transfer from the external RPV surface are implemented into the code and are based on real experimental data. However, the models of the RELAP/SCDAPSIM computer code should be updated to evaluate more complex processes in the debris bed and the ability to predict typical 2 or 3 layers stratification of oxides and metals could give more realistic results. Predicting the focusing effect would enable evaluating local critical heat fluxes, which are potentially dangerous when using IVR strategy for severe accident management.

4.4. Analytical Solution for Metal Layers and Focusing Effect.

As it was already mentioned, due to RELAP/SCDAPSIM limitations, this code does not take into account the debris separation into oxidic and metallic layers (shown in Figure 9). In order to bypass this limitation, the analytical study was carried out, assuming steady-state conditions in the lower head. This analytical study is based on the work done by

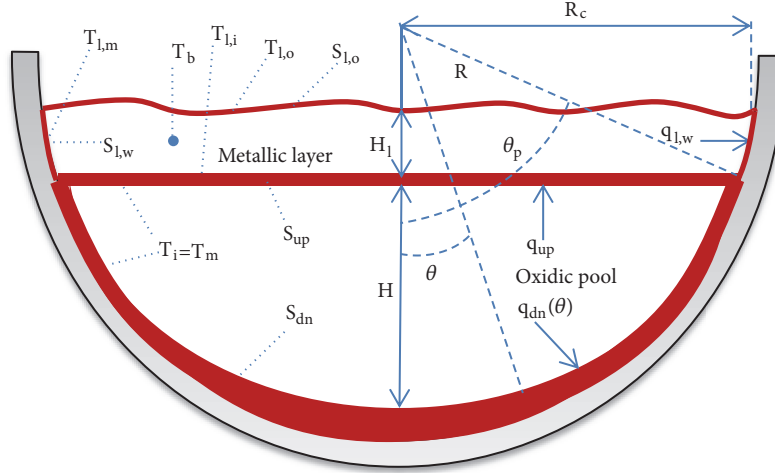


FIGURE 17: Graphical representation of parameters, used for solving the heat fluxes.

Theofanous et al. [2]. The sketch of the problem and variables is shown in Figure 17.

The heat transfer in the oxidic layer was calculated using the following:

$$Nu_{up} = 0.345 \cdot Ra^{10.233}, \quad (3)$$

$$Nu_{dn} = 0.0038 \cdot Ra^{10.35} \quad (4)$$

where Nu_{up} is the Nusselt number defining heat transfer to the metallic layer on the top of the oxidic layer and Nu_{dn} is the Nusselt number defining heat transfer to the vessel wall in contact with the oxidic layer. The power split between “up” and “down” regions is based on the assumption that the crust exists all around the oxidic pool and the interface temperatures of the upper boundary and side boundary are the same.

Ra' is the Rayleigh number with volumetric heating:

$$Ra' = Gr \cdot Pr \cdot Da \quad (5)$$

The dimensionless Grashof (Gr), Prandtl (Pr), and Dammköhler (Da) numbers used in this equation are expressed as follows:

$$Gr = \frac{g\beta(T_{max} - T_i)H^3}{\nu^2};$$

$$Pr = \frac{\nu}{\alpha}; \quad (6)$$

$$Da = \frac{\dot{Q}H^2}{k(T_{max} - T_i)}$$

where g is acceleration due to gravity (m/s^2); β is thermal expansion coefficient ($1/K$); k is thermal conductivity ($W/(m \cdot K)$); α is thermal diffusivity (m^2/s); ν is kinematic viscosity (m^2/s); T_{max} is bulk temperature of the fluid (K); T_i is temperature at the boundary (K); H is characteristic length or

in our case layer height (m); \dot{Q} is volumetric heat generation rate (W/m^3).

The heat transfer along the curved surface of the lower head depends on the contact angle, and to identify this heat transfer the correlations were used:

$$\frac{Nu_{dn}(\theta)}{Nu_{dn}} = 0.1 + 1.08 \left(\frac{\theta}{\theta_p} \right) - 4.5 \left(\frac{\theta}{\theta_p} \right)^2 + 8.6 \left(\frac{\theta}{\theta_p} \right)^3, \quad 0.1 \leq \frac{\theta}{\theta_p} \leq 0.6, \quad (7)$$

$$\frac{Nu_{dn}(\theta)}{Nu_{dn}} = 0.41 + 0.35 \left(\frac{\theta}{\theta_p} \right) + \left(\frac{\theta}{\theta_p} \right)^2, \quad 0.6 < \frac{\theta}{\theta_p} \leq 1 \quad (8)$$

where θ is contact angle at location of interest (degrees); θ_p is contact angle at the top of the oxidic layer (degrees).

The distribution between heat fluxes to the sidewalls (q_{dn}) and to the metallic layer (q_{up}) is found by the following:

$$\dot{Q}V = S_{up} \cdot q_{up} + S_{dn} \cdot q_{dn} \quad (9)$$

where \dot{Q} is volumetric heat generation rate of the oxidic layer (W/m^3); V is volume of the oxidic layer (m^3); S_{up} is contact area of the oxidic layer and the metallic layer.

After the oxidic layer is solved and the heat flux to the metallic layer (q_{up}) is found, the next step is to solve the heat fluxes in the metallic layer. The heat transfer in the metallic layer was calculated using Globe & Dropkin equation [23]:

$$Nu = 0.069 \cdot Ra^{1/3} \cdot Pr^{0.074} \quad (10)$$

TABLE 3: Inventories and basic properties of relocated materials.

| Material | Mass (kg) | Density (kg/m ³) | Specific heat c_p (J/kg·K) | Volume (m ³) |
|--|-----------|------------------------------|------------------------------|--------------------------|
| UO ₂ | 79337 | 8740 | 485 | 9.08 |
| ZrO ₂ | 5972 | 5990 | 815 | 1.00 |
| Zr | 12002 | 6130 | 458 | 1.96 |
| Fe | 3312 | 7020 | 835 | 0.47 |
| | | Volume averaged: | Mass averaged: | |
| Oxidic phase (UO ₂ +ZrO ₂): | 85309 | 8467.85 | 508.10 | 10.07 |
| Metallic phase (Fe+Zr): | 15314 | 6302.82 | 539.53 | 2.43 |
| TOTAL: | 100623 | | | 12.50 |

TABLE 4: Properties of oxidic and metallic layers assumed in analytical calculations.

| Property | Notation (unit) | OXIDIC layer | METALLIC layer |
|--|------------------------|--------------|----------------|
| Thermal expansion coefficient | β (1/K) | 1.05E-04 | 1.10E-04 |
| Thermal conductivity | k (W/m·K) | 5.3 | 31.4 |
| Dynamic viscosity | μ (Pa·s) | 5.35E-03 | 4.00E-03 |
| Emissivity (crust for Oxide and molten for Metallic) | ϵ | 0.8 | 0.45 |
| Liquidus temperature | T_i or $T_{l,m}$ (K) | 2973 | 1600 |

From energy balance considerations, as shown by Theofanous et al. (with the Prandtl number ~ 0.13), we have the following:

$$(T_{l,i} - T_b)^{4/3} = (T_b - T_{l,o})^{4/3} + \frac{H_l}{R_c} (T_b - T_{l,m})^{4/3} \quad (11)$$

$$0.15 \cdot k \left(\frac{g \cdot \beta}{\alpha \cdot \nu} \right)^{1/3} (T_b - T_{l,o})^{4/3} = \epsilon \sigma T_{l,o}^4 \quad (12)$$

$$q_{up} = 0.15 \cdot k \left(\frac{g \cdot \beta}{\alpha \cdot \nu} \right)^{1/3} (T_{l,i} - T_b)^{4/3} \quad (13)$$

This system of three equations is solved to find three unknowns: T_b , $T_{l,i}$, and $T_{l,o}$. The lower indices here are referred to as follows: b , bulk; l,o , top surface of the metallic layer; l,m , liquidus; l,w – metallic layer interface with RPV wall. Other variables are as follows: ϵ , emissivity; σ , Stefan-Boltzmann constant ($W \cdot m^{-2} \cdot K^{-4}$); H_l , height of metallic layer (m); R_c , radius at the top location of metallic layer (m).

After solving the temperatures, the heat flux to the RPV wall ($q_{l,w}$) is found by the following:

$$q_{l,w} = 0.15 \cdot k \left(\frac{g \cdot \beta}{\alpha \cdot \nu} \right)^{1/3} (T_b - T_{l,m})^{4/3} \quad (14)$$

The initial data for inventories of relocated materials were taken from the results of RELAP/SCDAPSIM calculations. The properties of materials were assumed the same as in Theofanous et al. [2]. For this analysis only base values were used. The initial data of relocated materials is shown in Table 3. The resulting debris bed is shown in Figure 18. The height of metallic layer is only 0.15 m. The values of other properties for the oxidic and metallic layers are given in Table 4.

The comparison of local heat flux from RPV wall to water with the CHF values allows justifying if IVR strategy could

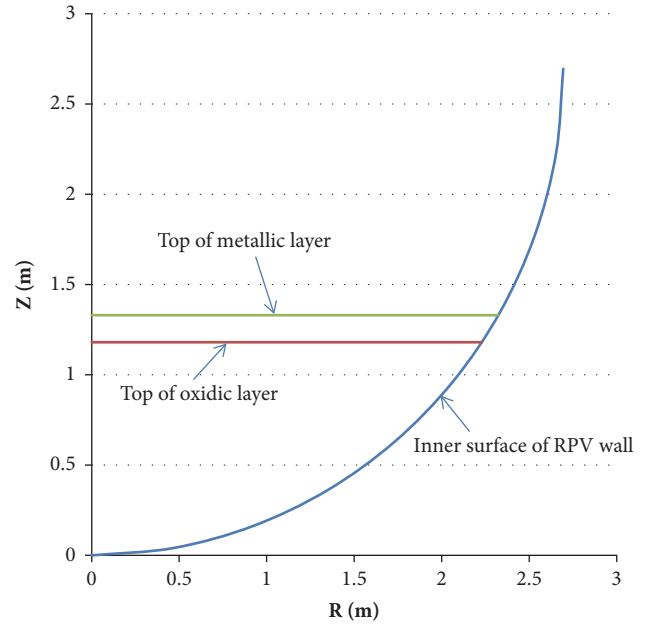


FIGURE 18: Graphical representation of oxidic and metallic layers in the RPV.

be successfully applied. This heat flux is directly related to the decay heat in the lower head. As it can be seen from Figure 10, the maximum decay heat (~ 30 MW) is observed at around 5000 s after the accident. This decay heat is very conservative, because additional time is needed for stratification and melting of the internal structures in the lower head. Moreover, the loss of volatiles in the lower head is not taken into account. However, the decay heat of 30 MW was assumed as an extreme case. Moreover, there were no additional steel added, which should come from core plate,

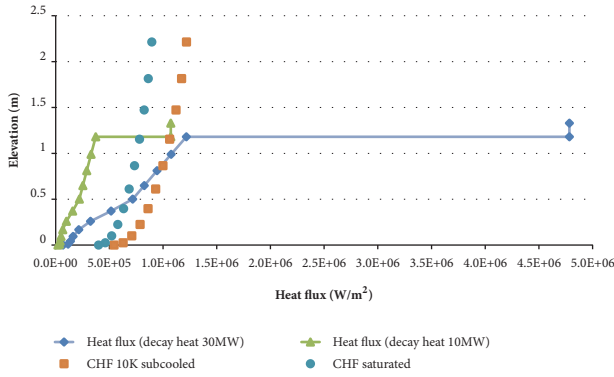


FIGURE 19: Calculated heat fluxes along the RPV wall. Decay heat 30 MW and 10 MW.

internal structures in the lower head, and the ablated vessel wall. The analytical calculation results for this extreme case, i.e., heat flux along the RPV wall together with CHF curves, are shown in Figure 19. As it is presented in the figure, with the metallic layer being only 0.15 m, 30 MW decay heat is too high, and RPV failure is inevitable due to excessive heat flux of 4.8 MW/m^2 . At the same time, it can be observed that, even within the oxidic layer, the heat flux exceeds the CHF. Therefore it could be concluded that IVR is not possible with 30 MW decay heat in such geometry of the lower head and such configuration of debris. It is shown in the same figure that in order to stay within the limits of subcooled boiling CHF (obtained by SBLB tests [20]), the decay heat should be less than 10 MW.

As it was demonstrated, the focusing effect is relatively high, but this is due to a very thin metallic layer, which is only 0.15 m. This case is not realistic, since more steel should be added from core plate and structures in the lower head. The total mass of stainless steel in control rod guide tubes and instrumentation guide tubes makes around 50,000 kg. Also, the ablated vessel wall would also eventually transfer to the metallic layer. Moreover, separation into oxidic and metallic layers takes time, and, during this time window, decay heat of molten materials also decreases. These transient processes are complicated and require detailed modelling, and in our case we must make more assumptions. For this reason, a parametric study has been conducted. In this parametric study, the oxidic layer was assumed the same in all cases; the target was to match the metallic layer heat flux and CHF of 10 K subcooled boiling. The CHF at the top of oxidic layer (height of 1.15 m) is equal to 1.06 MW/m^2 , so the criterion was set that the heat flux from metallic layer cannot exceed this value. Following these conditions for each decay heat value (25 MW - 10 MW), the minimum metallic layer height was found. The results are shown in Figure 20. The additional mass of steel required to reach metal layer height in each case is also presented in Figure 20.

Figure 10 suggests that the decay heat after debris stratification could reach 20–25 MW. In order to maintain the heat flux below CHF, additional 57000–90000 kg of steel would be needed. The availability of molten steel and timing of debris stratification during transient should be analyzed

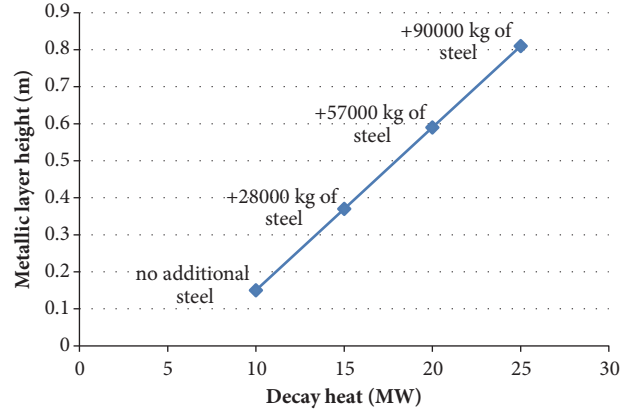


FIGURE 20: Decay heat versus metallic layer height, required to achieve heat flux equal to CHF.

with more capable software. The other aspect to consider in this approach is the CHF value itself, since higher values (up to $\sim 1.8 \text{ MW/m}^2$) can usually be reached using improved design (with baffle, vessel coating, etc.). With more details on the reactor design (masses of the melted different metallic structures in the vessel and possibility of enhancing the efficiency of the ERVC), the results of this study should be updated.

5. Conclusions

The initiating event selected for the analysis was large break LOCA with total failure of cooling water injection in a BWR-5 reactor in Mark-II containment with initial nominal power of $\sim 2000 \text{ MWt}$. In this most conservative scenario, no activation of emergency water supply system was assumed. This hypothetical scenario leads to the very fast overheating of the core and the start of fuel melting at high decay heat level (~ 600 seconds after the beginning of the accident). The dry-out of the lower head occurs approximately 1 hour after beginning of the accident. It was assumed in the simulation that the reactor cavity (pit) around the reactor vessel is flooded by water in advance. To evaluate RELAP/SCDAPSIM ability to model ex-vessel heat transfer, two modes were analyzed, i.e., (a) RELAP5 based heat transfer mode and (b) COUPLE based heat transfer mode.

It was observed that using RELAP5 based heat transfer mode the RPV wall temperature was overestimated, compared to the COUPLE based heat transfer mode. The correlations for ex-vessel heat transfer implemented into COUPLE computer code are based on the experimental results for the shape of RPV lower head, submerged into a pool of water. For this reason, employing the COUPLE based heat transfer mode is strongly recommended for such kind of problems. However, it must be noted that COUPLE heat transfer mode can be not suitable in some cases, e.g., specific geometry of the cooling channel and RPV coating.

RELAP/SCDAPSIM does not take into account the formation of the metallic layer on the top of the oxidic layer. For this reason, some important effects (such as focusing effect)

are not considered and the local heat fluxes are underestimated using this tool. Using the homogenous pool models, the results show that even for the most conservative initial and boundary conditions critical heat flux is not reached in the analyzed cases. To investigate the influence of debris separation into oxidic and metallic layers on the heat transfer through RPV wall and to evaluate the substantiation of received optimistic RELAP/SCDAPSIM calculation results, the analytical study was conducted. The analytical study presented in this paper showed that, considering oxidic and metallic layers, a relatively thin metallic layer (0.15 m), and maximum decay heat (30 MW), the steady-state heat flux in the metallic layer greatly exceeds the CHF value. The metallic layer height is calculated from the results of RELAP/SCDAPSIM, taking into account only steel in the reactor core, and 30 MW is the peak power calculated by RELAP/SCDAPSIM at the time of slumping. Since these values are not realistic during actual accident scenario, a parametric study has been conducted to identify metallic layer height needed to dissipate heat at lower rate than CHF. The results show that a significant amount of steel should be added (57000–90000 kg) in order to stay below CHF (1.06 MW/m²) in case of decay heat of 20–25 MW. This amount of steel could be acceded from core plate and structures in the lower head and ablated vessel wall. Unfortunately at this moment there is no possibility of precisely evaluating the amount of the steel which could be relocated to the lower head during the postulated accident.

The models of the RELAP/SCDAPSIM computer code are recommended to be updated to evaluate more complex processes in the debris bed and the ability to predict typical 2 or 3 layers stratification of oxides and metals could provide more realistic results.

The work presented in this article is a part of the IVMR project, which was launched with the objective to investigate the applicability of IVR as a strategy for severe accident management in nuclear reactors. The whole spectrum of different reactors will be investigated and the developed computational tools for predicting and defining their reliability will be a significant result of this project. The results of this project will be used as a strong background in the safety analysis, when implementing this strategy in real nuclear power plants, especially with high power reactors.

Data Availability

The data used to support the findings of this study are included within the article.

Conflicts of Interest

The authors declare that they have no conflicts of interest.

Acknowledgments

The work is performed in the frame of Project “In-Vessel Melt Retention Severe Accident Management Strategy for Existing and Future NPPs”, IVMR, under H2020 Grant Agreement no. 662157. The authors would like to thank Dr.

Javier Ortiz-Villafuerte (Nuclear Systems, National Institute of Nuclear Research, Mexico) for his considerable advice and providing information regarding mass of steel in control rod and instrumentation guide tubes.

References

- [1] H. Tuomisto and T. G. Theofanous, “A consistent approach to severe accident management,” *Nuclear Engineering and Design*, vol. 148, no. 2-3, pp. 171–183, 1994.
- [2] T. G. Theofanous, C. Liu, S. Additon, S. Angelini, O. Kymäläinen, and T. Salmassi, “In-vessel coolability and retention of a core melt,” *Nuclear Engineering and Design*, vol. 169, no. 1-3, pp. 1–48, 1997.
- [3] O. Kymäläinen, H. Tuomisto, and T. G. Theofanous, “In-vessel retention of corium at the Loviisa plant,” *Nuclear Engineering and Design*, vol. 169, no. 1-3, pp. 109–130, 1997.
- [4] H. Esmaili and M. Khatib-Rhabar, *NUREG/CR-6849, Analysis of In-Vessel Retention and Ex-Vessel Fuel Coolant Interaction for AP1000*, 2004.
- [5] J. L. Rempe, D. L. Knudson, K. G. Condie, K. Y. Suh, F.-B. Cheung, and S.-B. Kim, “Corium retention for high power reactors by an in-vessel core,” *Nuclear Engineering and Design*, vol. 230, no. 1-3, pp. 293–309, 2004.
- [6] D. L. Knudson, J. L. Rempe, K. G. Condie, K. Y. Suh, F.-B. Cheung, and S.-B. Kim, “Late-phase melt conditions affecting the potential for in-vessel retention in high power reactors,” *Nuclear Engineering and Design*, vol. 230, no. 1-3, pp. 133–150, 2004.
- [7] H. Schmidt, W. Brettschuh, J. Meseth et al., “Tests to investigate the RPV exterior two-phase flow behavior in the event of core melt,” in *Proceedings of the 38th European Two-Phase Flow Group Meeting*, Paper A6, Karlsruhe, Germany, 2000.
- [8] L. A. Dombrovskii, V. N. Mineev, A. S. Vlasov et al., “In-vessel corium catcher of a nuclear reactor,” *Nuclear Engineering and Design*, vol. 237, no. 15-17, pp. 1745–1751, 2007.
- [9] F. Fichot, L. Carénini, M. Sangiorgi et al., “Some considerations to improve the methodology to assess In-Vessel Retention strategy for high-power reactors,” *Annals of Nuclear Energy*, vol. 119, pp. 36–45, 2018.
- [10] L. Siefken, E. Coryell, S. Paik, and H. Kuo, “SCDAP/RELAP5 Modeling of Heat Transfer and Flow Losses in Lower Head Porous Debris,” INEEL/EXT-98-00820, Rev. 2, 1999.
- [11] G. Espinosa-Paredes and A. Nuñez-Carrera, “SBWR model for steady-state and transient analysis,” *Science and Technology of Nuclear Installations*, vol. 2008, Article ID 428168, 18 pages, 2008.
- [12] C. Allison, J. Hohorst, F. Venturi, N. Forgone, and R. Lopez, “Application of RELAP/SCDAPSIM/MOD3.5 to a Representative BWR for Fukushima-Daichii-like SBO transients,” in *Proceedings of the International Congress on Advances in Nuclear Power Plants, ICAPP 2013*, 2013.
- [13] G. Espinosa-Paredes, R. Camargo-Camargo, and A. Nuñez-Carrera, “Severe accident simulation of the laguna verde nuclear power plant,” *Science and Technology of Nuclear Installations*, vol. 2012, Article ID 209420, 11 pages, 2012.
- [14] M. M. Gris, “Reactor Pressure Vessel Neutron Embrittlement & Metal fatigue,” in *Materials Degradation Technical Meeting*, Vienna, Austria, 2013.
- [15] Bock. Module 06 Boiling Water Reactors (BWR), 2016.

- [16] M. J. Fallacara, *Hardened Containment Vents for BWR Mark I & II Containments and Evaluation of Filtration Systems*, Rensselaer Polytechnic Institute Hartford, Connecticut, USA, 2013.
- [17] C. M. Allison, G. A. Berna, E. W. Coryell et al., "SCDAP/RELAP5 Users Guide and Input Manual," NUREG/CR-6150 EGG-2720, Idaho National Engineering Laboratory, USA, 1998.
- [18] C. M. Allison, G. A. Berna, T. C. Cheng et al., "SCDAP/RELAP5/MOD 3.2 code manual volume II: damage progression model theory," NUREG/CR-6150 INEL-96/0422, Idaho National Engineering and Environmental Laboratory, New York, NY, USA, 1997.
- [19] A. Nuñez-Carrera, R. Camargo-Camargo, G. Espinosa-Paredes, and A. López-García, "Simulation of the lower head boiling water reactor vessel in a severe accident," *Science and Technology of Nuclear Installations*, vol. 2012, Article ID 305405, 8 pages, 2012.
- [20] F. Cheung, K. Haddad, and Y. Liu, "Critical heat flux (CHF) phenomenon on a downward facing curved surface," NUREG/CR6507, 1997.
- [21] R. Park, K. Kang, S. Hong, S. Kim, and J. Song, "Corium behavior in the lower plenum of the reactor vessel under IVR-ERVC condition: Technical issues," *Nuclear Engineering and Technology*, vol. 44, no. 5, pp. 237–248, 2012.
- [22] X. Wang and X. Cheng, "Analysis of Focusing Effect of Light Metallic Layer in Stratified Molten Pool Under IVR-ERVC Condition," *Journal of Nuclear Engineering and Radiation Science*, vol. 1, no. 2, article 021007, 2015.
- [23] S. Globe and D. Dropkin, "Natural-convection heat transfer in liquids confined by two horizontal plates and heated from below," *Journal of Heat Transfer*, vol. 81, no. 24, 1959.

Research Article

Effect of Molten Corium Behavior Uncertainty on the Severe Accident Progress

Wonjun Choi ¹, Taeseok Kim,¹ Joongoo Jeon ¹,
Nam Kyung Kim ¹ and Sung Joong Kim ^{1,2}

¹Department of Nuclear Engineering, Hanyang University, Seoul 04763, Republic of Korea

²Institute of Nano Science and Technology, Hanyang University, Seoul 04763, Republic of Korea

Correspondence should be addressed to Sung Joong Kim; sungjkim@hanyang.ac.kr

Received 22 March 2018; Revised 13 June 2018; Accepted 25 June 2018; Published 1 August 2018

Academic Editor: Jerzy Foit

Copyright © 2018 Wonjun Choi et al. This is an open access article distributed under the Creative Commons Attribution License, which permits unrestricted use, distribution, and reproduction in any medium, provided the original work is properly cited.

Uncertainty of a severe accident code output needs to be handled reliably considering its use in safety regulation of nuclear industry. In particular, severe accident codes are utilized for probabilistic safety assessment (PSA), where the uncertainty of severe accident progress should be considered carefully due to its influence on human reliability analysis. Therefore, in this study, the uncertainty analysis of severe accident progress was performed using MELCOR code, and a total of 200 data sets of in-vessel uncertainty parameters were generated by Latin hypercube sampling method. The rank regression analysis was also performed to investigate the effect of uncertainty parameters on the severe accident progress. Sensitivity coefficients (SCs) in MELCOR such as molten clad drainage rate and zircaloy melt breakout temperature showed significant influence on relocation time and dryout time of lower plenum. However, the influence of uncertainty parameter diminished as the accident progressed.

1. Introduction

Since Fukushima accident in 2011, numerous studies about the severe accident (SA) phenomena and their progress have been investigated experimentally and numerically. However, due to the large scale of nuclear power plants, not many experimental studies were conducted for the accident sequence. Therefore the researches about the SA progress were conducted mostly by the numerical analysis [1–5]. As far as the numerical analysis of SA progress is concerned, lumped parameter SA codes such as MELCOR [6], MAAP [7], and SCDAP/RELAP [8] have been utilized in general. However, it is widely accepted that the SA code results may generate large uncertainty because rather simplified models were adopted in the codes due to the incomplete knowledge about SA phenomena. Because the code results can be reutilized for calculating source terms in the frame of PSA level 3, it is very important to investigate the uncertainty range and to identify relative importance of input parameters [9, 10].

Among the code outputs, identifying timing of certain SA sequence is important in terms of human reliability analysis (HRA). As a practical example, the success probability of

human related actions can be defined as a function of available time in HRA [11]. Thus, the timing of SA progress is important to define the available time for certain human related actions. Therefore, the uncertainty of the SA progress in terms of the major sequence time needs to be analysed for better understanding on the nuclear safety. For this reason, the major objective of this study is to perform the uncertainty analysis about occurrence time of SA progression phenomena. A representative SA scenario was selected as short term station black out (STSBO). STSBO is the scenario that all power, even direct current (DC) batteries, is unavailable. Because the safety feature using batteries is also unavailable, the accident progress can be faster than other accident scenarios.

2. Numerical Methodologies

2.1. Description of MELCOR Code [6]. MELCOR code is an integrated SA code for various kinds of nuclear power reactors. Since 1982, MELCOR code has been developed by Sandia National Laboratories (SNL) and used for plant risk assessment and source term analysis. To simulate various SA

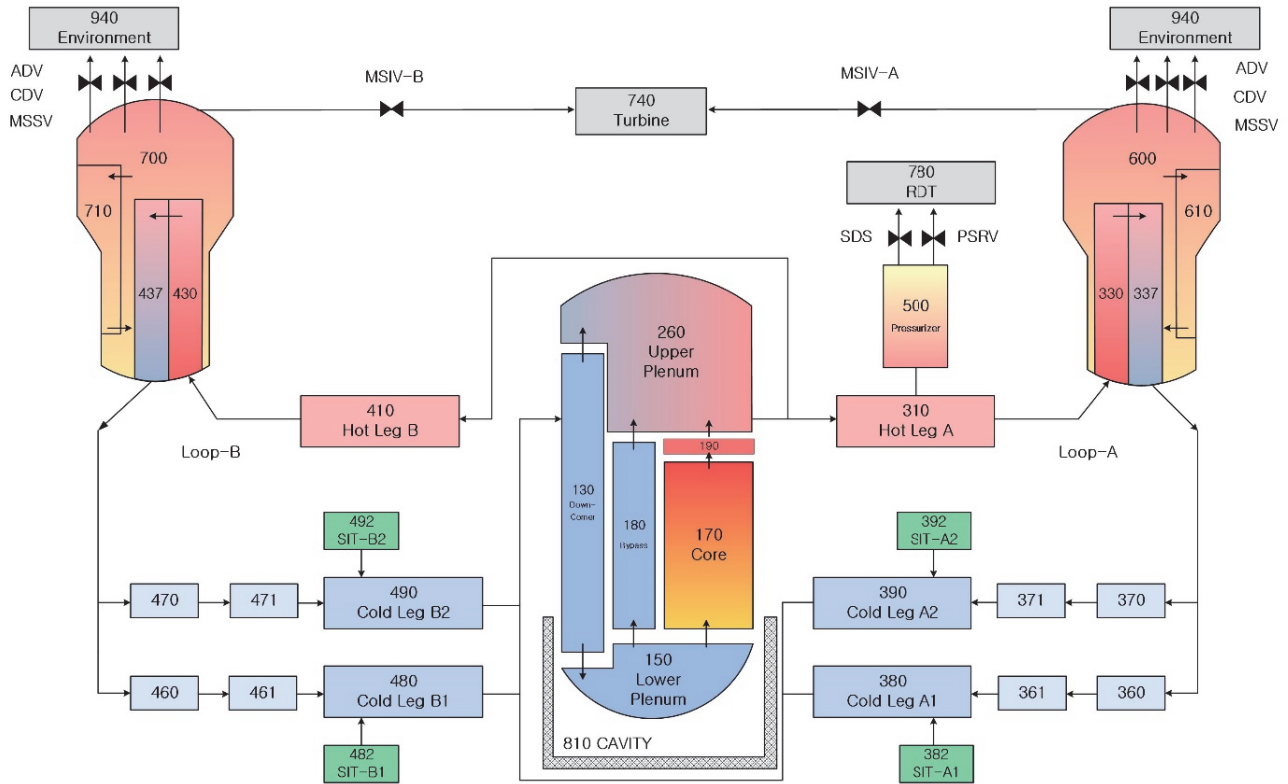


FIGURE 1: The nodalization of OPR1000 MELCOR input model.

phenomena, a number of modular packages were coupled in a unified frame. By the interaction of each modular package, MELCOR code can simulate thermal-hydraulic response of the plant, heat-up, oxidation, degradation and relocation of the core, and fission product release and transport. Because of the lack of knowledge about the SA phenomena and the interest of quick code execution time, parametric equations were used to model complicated physical processes in the past. However most recent MELCOR models are mechanistic thank to the improved calculation speed of modern computers. In many of the mechanistic models, adjustable optional parameters can be also available for uncertainty analyses and sensitivity studies. For that reason, MELCOR version 2.1.6342 was used.

2.2. MELCOR Input Model of OPR1000. As a reference plant, Optimized Power Reactor 1000 MWe (OPR1000), which consists of majority of Korean operating NPP, was selected. The nodalization of OPR1000 input model is shown in Figure 1. The input model includes reactor coolant system (RCS) composed of 25 control volumes (CVs) and simple secondary side composed of two steam generators (SGs) and a turbine. RCS consists of two hot legs (CV310 and 410), four cold legs (CV380, 390, 480 and 490), pressurizer (CV500), and reactor pressure vessel (RPV) with 6 detailed volumes (CV130, 150, 180, 170, 190, and 260). At the top of a pressurizer, pressurizer safety relief valves (PSRVs) and safety depressurization system (SDS) were modeled to simulate release of RCS coolant in case of depressurization.

The containment (CNMT) consists of 20 CVs and the total free volume is $77,440 \text{ m}^3$. Figure 2 shows the nodalization of the core. Total 7 ~ 8 radial rings and 14 axial nodes were modeled for the detailed simulation of the reactor core. 1st ~ 3rd axial core nodes were coupled with CV150 (LP), and 4th ~ 14th axial core nodes were coupled with CV170 (core region). In the core region, only 4th ~ 13th axial core nodes contained the nuclear fuel. The supporting structures were located at the 1st, 2nd, 3rd, 6th, 9th, and 12th axial node, and support plate was modeled in 3rd axial node. Total initial mass of uranium fuel, zirconium cladding, and stainless steel in the core were 85,692.0 kg, 23,910.58 kg, and 20,024.4 kg, respectively.

2.3. Description of Uncertainty Parameters and Distribution.

In SOARCA project [9], the uncertainty analysis of source term was performed using MELCOR code. Based on PIRT process by SNL and nuclear regulatory commission (NRC), total 24 epistemic MELCOR parameters were selected for uncertain input parameters of Surry power plant. To study the effect of molten corium behavior on the severe accident progress, 5 of uncertain parameters in COR package were selected in this study. The detailed distribution of uncertain parameters referred to the uncertainty analysis of Surry plant in SOARCA project. Table 1 shows the selected uncertain parameters and distributions. The lower/upper bound of zircaloy melt breakout temperature (SC1131(2)) was defined by melting point of zircaloy (2100 K) and the value of hydrogen uncertainty study [12] based on Phebus experiments [13]. The distribution was updated from the distribution

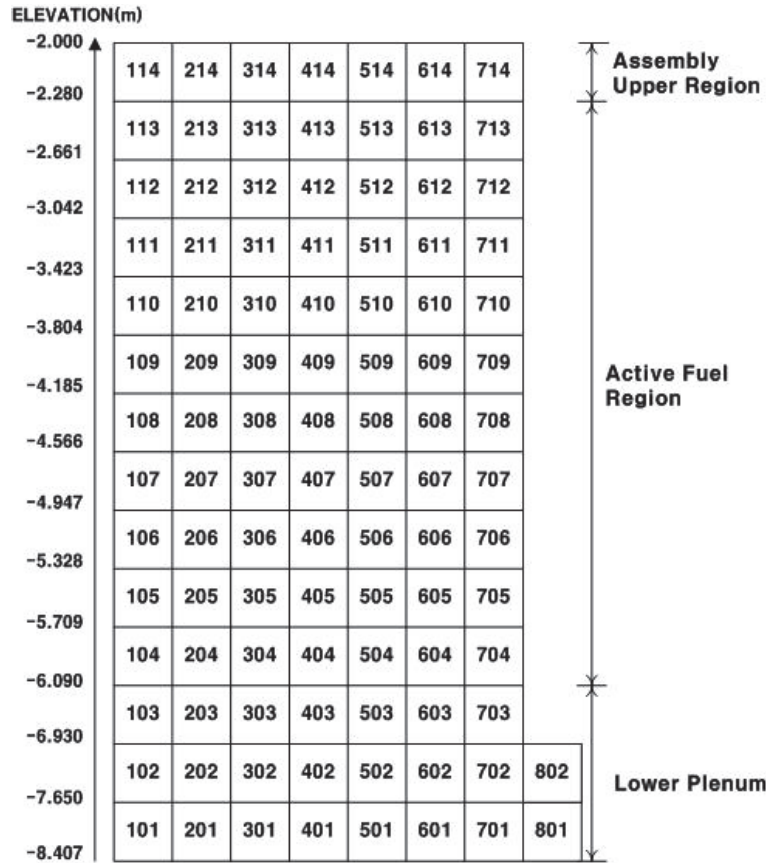


FIGURE 2: The core nodalization of OPR1000 MELCOR input model.

TABLE 1: The information of PDF about selected uncertainty parameters.

| Uncertainty parameter | Distribution type | Distribution parameters | Lower bound | Upper bound |
|--|-------------------|----------------------------------|------------------------------|---------------------------------|
| Zircaloy melt breakout temperature (SC1131(2)) | Scaled beta | α : 3.83 β : 3.0 | 2,100 K | 2,540 K |
| Molten clad drainage rate (SC1141(2)) | Log triangular | Mode: 0.2 | 0.1 kg/m-s | 2.0 kg/m-s |
| Radial solid/molten debris relocation time constant (SC1020(1)/SC1020(2)) | Uniform | - | Molten: 10 s Solid: 100 s | Molten: 100 s Solid: 1,000 s |
| Effective temperature at which the eutectic formed from UO ₂ and ZrO ₂ melts (SC1132(1)) | Normal | Mean: 2,479 K σ : 83 K | - | - |

of Peach bottom plants with the S/Q simulation results [14]. Because the technical base for the boundary values of molten clad drainage rate (SC1141(2)) and radial solid/molten debris relocation time constant (SC1020) were insufficient, the boundaries of these uncertainty parameters were selected based on order of magnitude. The default value of molten clad drainage rate was determined with CORA-13 experiment. Therefore, log triangular distribution, that is, the mode value is this default value, was used for the distribution of molten clad drainage rate. The uniform distribution was used for radial solid/molten debris relocation time constant due to the lack of experimental data. The distribution of Effective temperature at which the eutectic formed from UO₂ and

ZrO₂ melts was created based on the mean and standard deviation of 6 test results from VERCORS experiment [15].

2.4. Description of Sampling and Quantification of Results. Symbolic nuclear analysis package (SNAP) is a graphical user interface for simplifying the task of creating input files for the analytic codes and helping to visualize code results [16]. Input files of MELCOR code can also be created by SNAP. For uncertainty and sensitivity analysis, SNAP provides the additional plugin called “DAKOTA”. Using DAKOTA plugin, users can create the random samples of each sensitivity coefficient by LHS method and combine them into an input data set. The correlation between uncertain parameters was

TABLE 2: The accident sequence of base case.

| Accident sequence | Time (s) |
|--------------------------|----------|
| Reactor trip | 0 |
| RCP trip | 0 |
| MFW trip | 0 |
| SG dryout | 3,762 |
| PSRV open | 4,881 |
| Core exposure | 5,359 |
| Oxidation start | 8,991 |
| Core dryout | 9,990 |
| Cladding melt | 10,297 |
| Initial melt relocation | 10,441 |
| First LP dryout | 12,866 |
| RPV failure | 14,462 |
| CNMT over-pressurization | 60,100 |

not considered in this study. Variance inflation factor and correlation coefficient between sampled input parameters were checked to prevent significant correlation between input parameters by random sampling. In this study, total 200 cases were generated and simulated until 259,200 s (72 hrs). For the quantification of the effect of the selected uncertain parameters on the accident progress, the time of initial melt relocation, LP dryout, RPV failure, and CNMT leak were investigated as major output parameters. In addition, the statistics of the major output parameter were calculated. To investigate the individual effect of uncertain input parameters, linear rank regression analysis was also performed.

3. Results and Discussion

3.1. Description of Base Case. To investigate the uncertainty of SA progress, the aforementioned STSBO was selected as a base case. All of safety features were assumed to fail by losing AC power, and steam driven auxiliary feed water (AFW) pump was also modeled to fail. Table 2 shows the SA sequence of the base case. The STSBO was initiated by losing AC power and subsequently the reactor was tripped. With the reactor tripped, reactor coolant pumps (RCPs) and main feed water (MFW) pumps stopped. Following the reactor trip, the decay heat from the core was removed by the natural circulation of primary coolant during early phase of the accident. Because the AFW pumps were unavailable by the assumption, all SGs were exhausted at 3,762 s by the heat from the RCS. The RCS pressure increased with the loss of secondary heat removal, and the PSRV was opened at 4,881 s as shown in Figure 3. The reactor coolant was released to the CNMT through the PSRV, and thus it caused the core uncover at 5,359 s. The exposed core was heated up due to the lack of coolant, and additional oxidation heat generated between high temperature steam and high cladding temperature ($>1,100$ K) accelerated the core heat-up from 8,991 s. The coolant in the core region was dried out at 9,990 s and dryout of the LP region occurred at 12,866 s due to the relocated core debris as shown in Figure 4. After the first LP dryout, thru-wall yielding mode of RPV failure was initiated by the heat of relocated core debris.

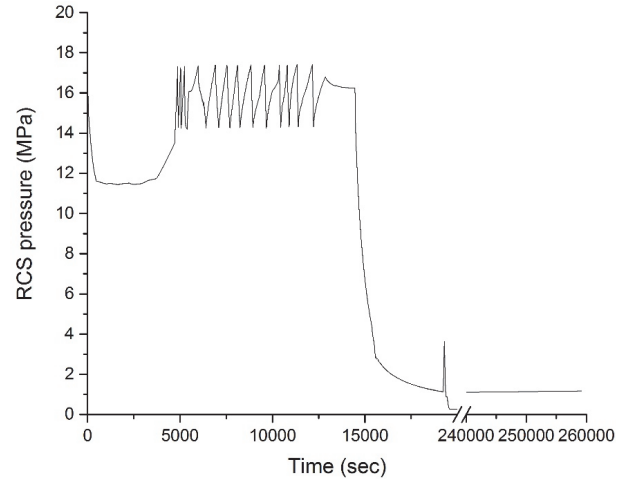


FIGURE 3: RCS pressure in the base case (STSBO).

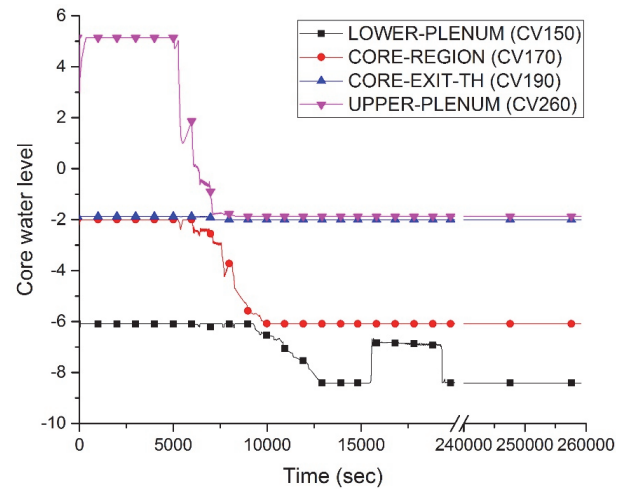


FIGURE 4: Core water level in the base case (STSBO).

When the RPV failure was initiated, the RCS pressure reached to 16.25 MPa (Figure 3). Due to the high pressure, the core debris was released into the CNMT via high pressure melt ejection (HPME) phenomena. Figure 5 shows the ejected debris mass from the RPV, debris mass in the cavity, and mass of debris ejected to CNMT atmosphere by the HPME. At first ejection with RPV failure (14,462 s), 6,341 kg of the 8,819 kg of debris ejected from the RPV was ejected to CNMT atmosphere. Because the RCS pressure decreased after the first ejection, the ejected debris mass following the first ejection only contributes to the increase of debris mass retained in the cavity. After about 19,200 s, 119,870 kg of core debris was ejected to the cavity due to the collapse of remained fuel structure. Figure 6 shows the CNMT pressure during the STSBO accident. Before the RPV failure, the CNMT pressure was repeated to increase and decrease by the opening and closure of the PSRV. After the RPV failure, 0.26 MPa of pressure peak was observed due to the direct containment heating (DCH) by the HPME.

TABLE 3: The statistics values of accident progress.

| Accident progression phenomena | # of cases | Base case | Mean (s) | C.V. | Median (s) | P5 (s) | P95 (s) |
|--|------------|-----------|----------|-------|------------|--------|---------|
| Initial melt relocation | 200 | 10,441 | 10,445 | 0.013 | 10,491 | 10,244 | 10,601 |
| First LP dryout | 199 | 12,866 | 13,421 | 0.023 | 13,466 | 12,831 | 13,811 |
| RPV failure | 199 | 14,462 | 15,850 | 0.047 | 15,731 | 14,911 | 17,253 |
| CNMT over-pressurization (CNMT pressure > 0.44 MPa) | 162 | 60,100 | 60,779 | 0.075 | 58,932 | 55,882 | 69,272 |

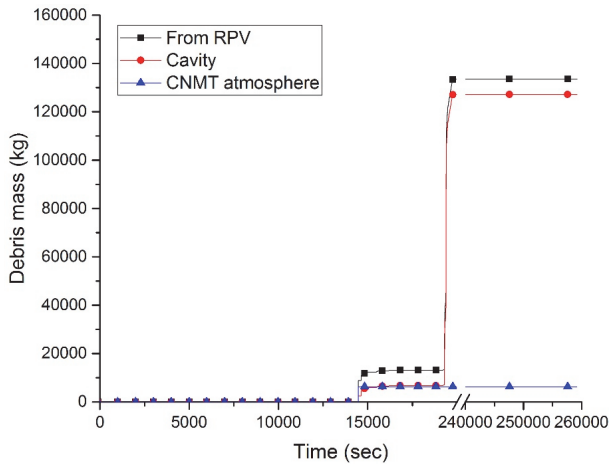


FIGURE 5: Ejected debris mass after RPV failure.

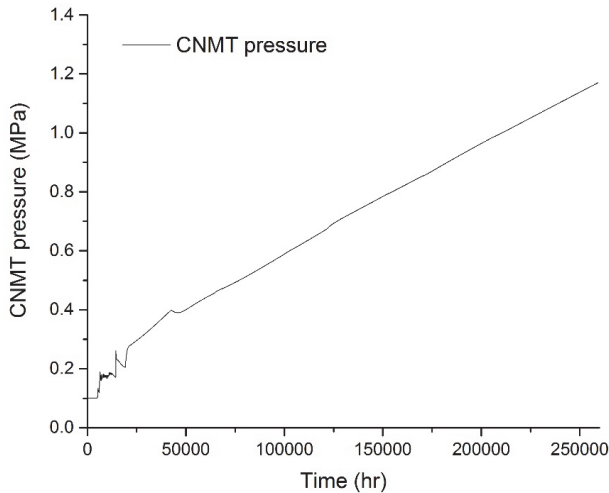


FIGURE 6: CNMT pressure in the base case (STSBO).

Because the debris within the cavity released the heat and noncondensable gas by molten corium concrete interaction (MCCI), the CNMT pressure increased continuously and reached to design pressure (0.44 MPa) at 60,100 s. The CNMT pressure at the end of calculation (259,200 s) was calculated as 1.17 MPa.

3.2. Statistics of Major Accident Progress. Among a total of 200 sample cases, only 162 cases were calculated until

259,000 s (72 hrs). Because of COR or CAV package errors, 37 cases were stopped as soon as the RPV failure was reported. A case was calculated until the initial melt relocation. However, it was terminated before the RPV failure. For that reason, the statistics of accident progress such as mean, coefficient of variance (C.V.), median, 5th percentile (P5), and 95th percentile (P95) were calculated through the available cases. Table 3 shows the statistical values of accident progress. The selected uncertainty parameters affected the accident progress after cladding melt. Therefore, the statistical values of initial melt relocation, first LP dryout, RPV failure, and CNMT overpressurization time were investigated. The mean values of initial melt relocation, first LP dryout, RPV failure, and CNMT overpressurization were calculated as 10,445 s, 13,421 s, 15,850 s, and 60,100 s, respectively. All mean values of accident progress were larger than those of the base case. The values of C.V. show that the variance of accident progress increased as the accident progressed. The median values of initial melt relocation, first LP dryout, RPV failure, and CNMT overpressurization were estimated as 10,491 s, 13,466 s, 15,731 s, and 58,932 s, respectively. Median values of initial melt relocation and first LP dryout time were larger than mean values of those. It means that the distributions were biased toward the high values. On the other hand, RPV failure and CNMT overpressurization time were biased toward the low values. Figure 7 shows these biased distributions of accident progress. Counts on Y-axis corresponded to the number of samples that was included in specific range about the time of accident progression phenomena on X-axis. The 5th/95th values of initial melt relocation, first LP dryout, RPV failure, and CNMT overpressurization were 10,244 s/10,601 s, 12,831 s/13,811 s, 14,911 s/17,252 s, and 55,882 s/69,272 s, respectively. Using bias-corrected and accelerated bootstrap method, 95% confidence interval of 5th/95th values was also calculated. The confidence intervals for 5th/95th values of initial melt relocation, first LP dryout, RPV failure, and CNMT overpressurization were 10,236 ~ 10,246 s/10,586 ~ 10,651 s, 12,676 ~ 12,931 s/13,781 ~ 13,841 s, 14,826 ~ 14,973 s/17,192 ~ 17,304 s, and 55,621 ~ 56,187 s/68,798 ~ 69,639 s, respectively.

3.3. Regression Analysis of Uncertainty Parameters on Accident Progress. Although the ordinary linear regression can show the potential relations between input and output values, capturing any complex relationship is challenging in reality [9]. Because the accident progress is the cumulative result of various phenomena, the relationship between in-vessel uncertain parameters and accident progress may be

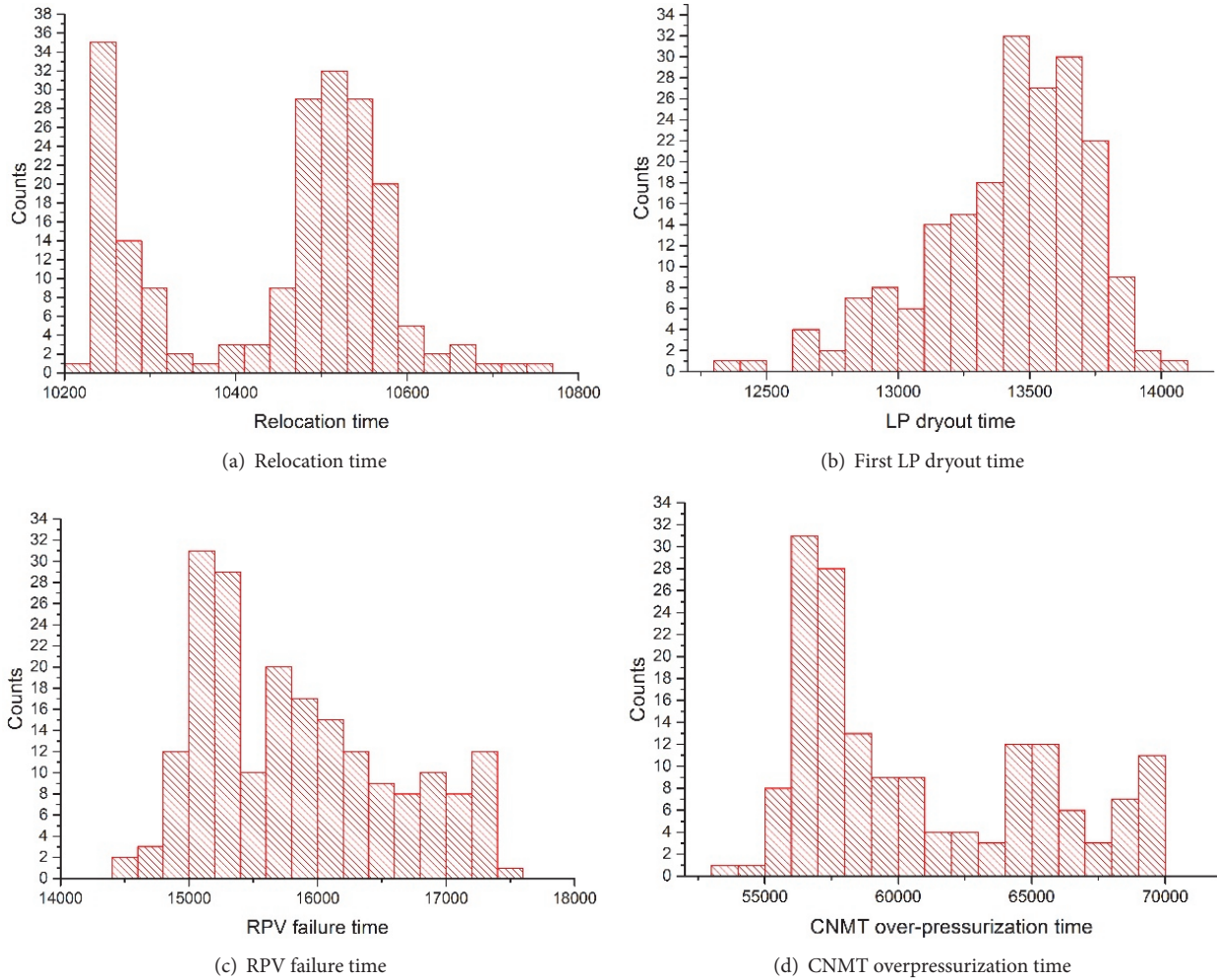


FIGURE 7: Histogram of major accident progress.

nonlinear or complex. Thus, in this study, rank regression technique was used to investigate the potential relations between in-vessel uncertainty and accident progress. The rank regression is a kind of linear regression, which uses rank values rather than original values. Using the rank values, the rank regression can capture the potential relations including nonlinear influence [17, 18]. For the rank regression results, standardized rank regression coefficient (SRRC) and partial rank correlation coefficient (PRCC) were summarized in Figure 8.

The coefficient of determination values shows how the regression model explains the relationship between input and output parameters. In this study, adjustable R square (Adj. R^2) was used for the coefficient of determination. The Adj. R^2 values of the regression model about initial melt relocations show that the in-vessel uncertainty parameters explain the potential relationships about initial melt relocation in a limited way. However, as the accident progressed, the influence of in-vessel uncertainty parameters on the regression model decreased. In cases of RPV failure and CNMT overpressurization, Adj. R^2 values were significantly low (Adj. $R^2 < 0.3$). Thus the regression model could not explain the relationship

between input and output. These results might be caused by the complex behavior of molten corium relocation. In this case, although the uncertainty parameters affected the tendency of molten corium behavior, the effect on the results can be insignificant due to the cumulative random variation.

In case of initial melt relocation, SRRC and PRCC show strong negative correlation ($r < -0.7$) between SC1141(2) and the timing of initial melt relocation. Figure 9 shows the scatter plot of relocation time versus SC1141(2). The distribution was divided into two categories by 10,400 s of the relocation time. The strong negative correlation resulted from the upper relocation time category. More cases in the upper relocation time category were observed in lower value of SC1141(2) due to the blockage effect. During the candling process, the molten core materials can be refrozen by the candling heat transfer and form the blockage. Because the lower value of SC1141(2) indicates the slower downward flow of molten core materials, the possibility of blockage formation increased with the lower value of SC1141(2). Therefore, the increment of blockage could delay the relocation time.

SRRC of first LP dryout shows that SC1141(2) and SC1131(2) were the most significant parameters affecting the

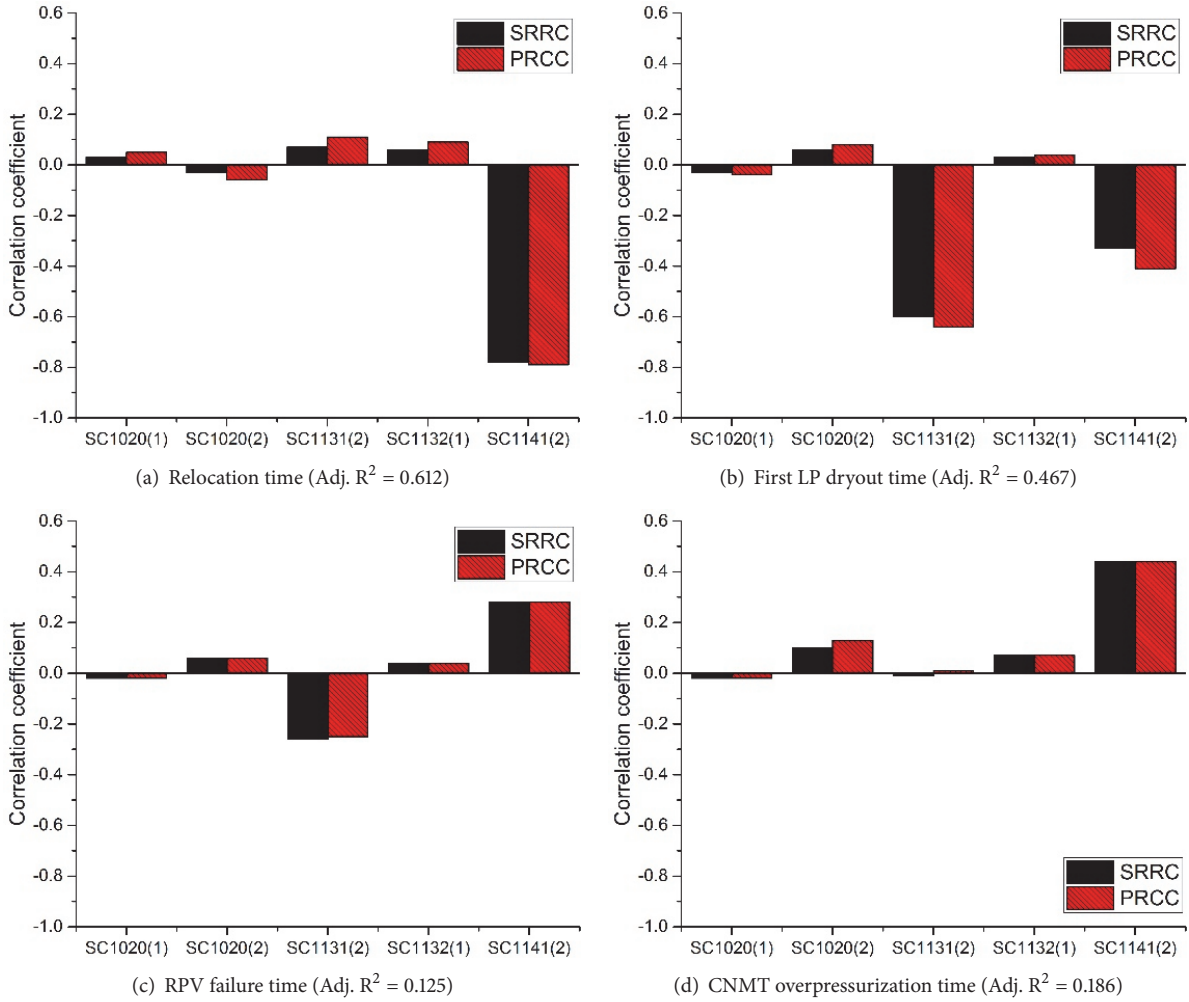


FIGURE 8: Linear regression results of accident progress.

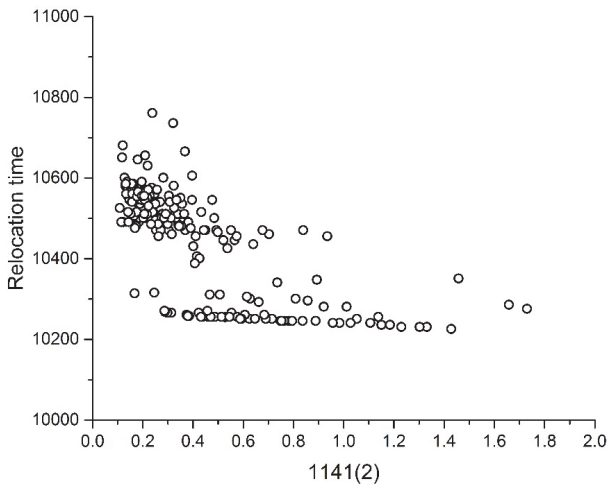


FIGURE 9: The scatter plot of relocation time versus SC1141(2).

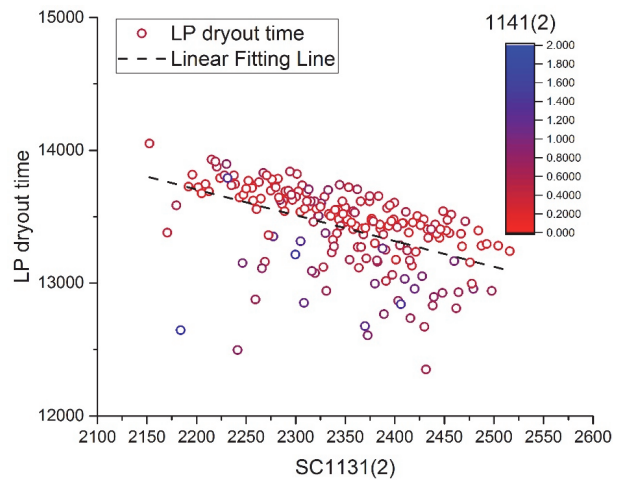


FIGURE 10: The scatter plot of first LP dryout time versus SC1141(2).

first LP dryout. SRRC and PRCC indicated moderate negative relationship ($-0.3 > r > -0.7$) between these two uncertainty

parameters and first LP dryout time. Figure 10 shows the scatter plot of first LP dryout time versus SC1131(2). Using

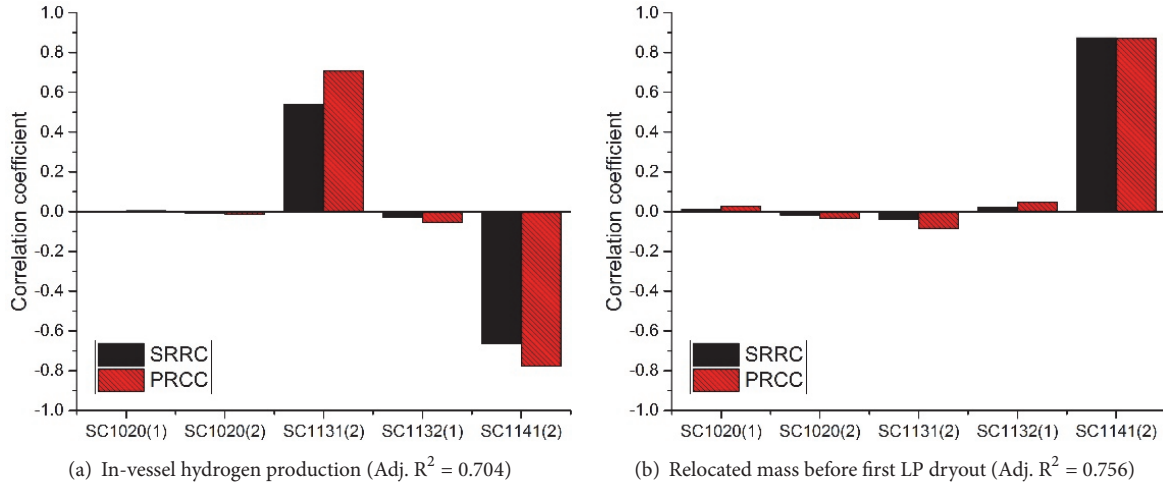


FIGURE 11: Linear regression results of potential factor about first LP dryout time.

the color scatter, the values of SC1141(2) were shown in the scatter plot. The linear fitting line shows the negative relationship between SC1131(2) and first LP dryout time. In case of SC1141(2), more blue color scatters were observed below the fitting line. However, this trend was not clear due to the number of samples below the fitting line. The hydrogen production mass and relocated mass before first LP dryout can describe the effect of SC1131(2) and SC1141(2) on first LP dryout time. Figure 11 shows the SRRC and PRCC values of in-vessel hydrogen production and relocated mass before first LP dryout. The high Adj. R^2 value (Adj. $R^2 > 0.7$) shows that the rank regression model can properly explain the relationship between uncertainty parameters and hydrogen production and relocated mass. PRCC indicated strong negative correlation between SC1141(2) and in-vessel hydrogen production and strong positive correlation between SC1141(2) and relocated mass before first LP dryout. While the lower hydrogen production reduced the total heat accumulated in the core, the higher relocated mass transferred more heat to water in LP. Therefore, the effect of SC1141(2) on first LP dryout can be reduced by the countering effect. In case of SC1131(2), only moderate positive correlation between SC1131(2) and in-vessel hydrogen production was observed. For that reason, the effect of SC1131(2) on in-vessel hydrogen production directly influenced the first LP dryout time.

4. Conclusions

To investigate the uncertainty of accident progress induced by in-vessel uncertainty parameters, uncertainty quantification was performed with regard to the timing of initial melt relocation, first LP dryout, RPV failure, and CNMT overpressurization. A total of 200 data sets of sensitivity coefficients in COR package were generated by SNAP-DAKOTA plugin using the LHS method. 5th/95th range of initial melt relocation, first LP dryout, RPV failure, and CNMT overpressurization were 10,244 s / 10,601 s, 12,831 s / 13,811 s, 14,911 s / 17,253 s, and 55,882 s / 69,272 s, respectively. The rank regression analysis was also performed to investigate the effect of in-vessel uncertainty

parameters. The regression results show that zircaloy melt breakout temperature (SC1131(2)) and molten clad drainage rate (SC1141(2)) exhibited significant influence on initial melt relocation time and first LP dryout time, respectively. Although only in-vessel uncertainty parameters among input parameters were modified, the effect on RPV failure and CNMT overpressurization time could not be described by the rank regression model. To clearly understand the effect of in-vessel uncertainty on accident progress, various regression techniques and the stochastic studies about the core behavior should be performed for the future work.

Nomenclature

| | |
|--------------|--------------------------------------|
| Adj. R^2 : | Adjustable R square |
| AFW: | Auxiliary feed water |
| C.V.: | Coefficient of variance |
| CNMT: | Containment |
| CV: | Control volume |
| DCH: | Direct containment heating |
| HPME: | High pressure melt ejection |
| HRA: | Human reliability analysis |
| LHS: | Latin hypercube sampling |
| LP: | Lower plenum |
| MCCI: | Molten corium concrete interaction |
| MFW: | Main feed water |
| P5: | 5th percentile |
| P95: | 95th percentile |
| PDF: | Probability distribution function |
| PRCC: | Partial rank correlation coefficient |
| PSA: | Probabilistic safety assessment |
| PSRV: | Pressurizer safety relief valve |
| r: | Value of coefficient |
| RCS: | Reactor coolant system |
| RCP: | Reactor coolant pump |
| RPV: | Reactor pressure vessel |
| SA: | Severe accident |
| SC: | Sensitivity coefficient |
| SDS: | Safety depressurization system |

SG: Steam generator
 SANP: Symbolic nuclear analysis package
 SNL: Sandia national laboratories
 SRRC: Standardized rank regression coefficient
 STSBO: Short term station black out.

Data Availability

The data used to support the findings of this study are available from the corresponding author upon request.

Conflicts of Interest

The authors declare that there are no conflicts of interest regarding the publication of this paper.

Acknowledgments

This work was supported by the National Research Foundation of Korea (NRF) funded by the Ministry of Science & ICT (MSIT, Korea) [Grant no. NRF-2017M2A8A4018213] and the Nuclear Safety Research Program through the Korea Foundation of Nuclear Safety (KoFONS) using the financial resource granted by the Nuclear Safety and Security Commission (NSSC) of the Republic of Korea (no. 1805001).

References

- [1] T. Sevón, "A MELCOR model of Fukushima Daiichi Unit 1 accident," *Annals of Nuclear Energy*, vol. 85, pp. 1–11, 2015.
- [2] R.-J. Park, S.-B. Kim, and H.-D. Kim, "Evaluation of the RCS depressurization strategy for the high pressure sequences by using SCDAP/RELAP5," *Annals of Nuclear Energy*, vol. 35, no. 2, pp. 150–157, 2008.
- [3] S. Lee, K. S. Ha, H.-Y. Kim, and S. J. Kim, "Validation of RCS depressurization strategy and core coolability map for independent scenarios of SBLOCA, SBO, and TLOFW," *Journal of Nuclear Science and Technology*, vol. 51, no. 2, pp. 181–195, 2014.
- [4] S. Seo, Y. Lee, S. Lee, H.-Y. Kim, and S. J. Kim, "Effectiveness and adverse effects of reactor coolant system depressurization strategy with various severe accident management guidance entry conditions for OPR1000," *Journal of Nuclear Science and Technology*, vol. 52, no. 5, pp. 695–708, 2015.
- [5] Y. Lee, W. Choi, and S. J. Kim, "Efficacy assessment of independent severe accident mitigation measures in OPR1000 using MELCOR code," *Journal of Nuclear Science and Technology*, vol. 54, no. 1, pp. 89–100, 2017.
- [6] SNL, "MELCOR Computer Code Manuals, Vol. 1: Primer and Users' Guide," SAND2015-6691R, Sandia National Laboratories, 2015.
- [7] EPRI, *MAAP4 applications guidance desktop reference for using MAAP4 software*, Electric Power Research Institute, 2010.
- [8] INEEL, "SCDAP/RELAP5-3D code manual bolome3: user's guide and input manual," Idaho National Engineering and Environmental Laboratory, 2003.
- [9] U. S. NRC, *State-of-the-Art Reactor Consequence Analyses Project: Uncertainty Analysis of the Unmitigated Long-Term Station Blackout of the Peach Bottom Atomic Power Station*, NUREG/CR-7155, SAND2012-10702P, United States Nuclear Regulatory Commission, 2012.
- [10] SNL, "Fukushima Daiichi Unit 1 Uncertainty Analysis-Exploration of Core Melt Progression Uncertain Parameters-Volume II," Tech. Rep., SAND2015-6612, Sandia National Laboratories, 2015.
- [11] J. C. Joe, R. B. Shirley, D. Mandelli, R. L. Boring, and C. L. Smith, "The Development of Dynamic Human Reliability Analysis Simulations for Inclusion in Risk Informed Safety Margin Characterization Frameworks," *Procedia Manufacturing*, vol. 3, pp. 1305–1311, 2015.
- [12] R. O. Gauntt, N. E. Bixler, and K. C. Wagner, "An uncertainty analysis of the hydrogen source term for a station blackout accident in Sequoyah using MELCOR 1.8.5," Tech. Rep. SAND2014-2210, 2014.
- [13] N. Girault and F. Payot, "Insights into iodine behaviour and speciation in the Phébus primary circuit," *Annals of Nuclear Energy*, vol. 61, pp. 143–156, 2013.
- [14] P. Hofmann et al., "ZrO₂ Dissolution by Molten Zircaloy and Cladding Oxide Shell Failure. New Experimental Results and Modeling," in *Wissenschaftliche Berichte, INVCIT(98)-P026*, 1999.
- [15] Y. Pontillon, P. P. Malgouyres, G. Ducros et al., "Lessons learnt from VERCORS tests.: Study of the active role played by UO₂-ZrO₂-FP interactions on irradiated fuel collapse temperature," *Journal of Nuclear Materials*, vol. 344, no. 1-3, pp. 265–273, 2005.
- [16] U. S. NRC, "Symbolic Nuclear Analysis Package (SNAP)," NUREG/CR-6974, 2009.
- [17] K.-I. Ahn, S.-H. Park, H.-D. Kim, and H. S. Park, "The plant-specific uncertainty analysis for an ex-vessel steam explosion-induced pressure load using a TEXAS-SAUNA coupled system," *Nuclear Engineering and Design*, vol. 249, pp. 400–412, 2012.
- [18] S. Y. Park, K.-I. Ahn, and Y. M. Song, "Uncertainty Analysis of the Potential Hazard of MCCI during Severe Accidents for the CANDU6 Plant," *Science and Technology of Nuclear Installations*, vol. 2015, pp. 1–6, 2015.

Research Article

Analysis of Steam Explosion under Conditions of Partially Flooded Cavity and Submerged Reactor Vessel

Sang Ho Kim , Seong-Wan Hong, and Rae-Joon Park

Thermal Hydraulic and Severe Accident Research Division, Korea Atomic Energy Research Institute, 989-111 Daedeok-daero, Yuseong-gu, Daejeon 34057, Republic of Korea

Correspondence should be addressed to Sang Ho Kim; sangho@kaeri.re.kr

Received 21 March 2018; Revised 21 May 2018; Accepted 6 June 2018; Published 5 July 2018

Academic Editor: Arkady Serikov

Copyright © 2018 Sang Ho Kim et al. This is an open access article distributed under the Creative Commons Attribution License, which permits unrestricted use, distribution, and reproduction in any medium, provided the original work is properly cited.

A steam explosion in a reactor cavity makes a mechanical load of the pressure pulse, which can result in a failure of the containment isolation. To prove the integrity of the containment during the ex-vessel steam explosion, the effects of water conditions on a steam explosion have to be identified, and the impulse of a steam explosion has to be exactly assessed. In this study, the analyses for steam explosions were performed for the conditions of a partially flooded cavity and a submerged-vessel in a pressurized water reactor. The entry velocity of a corium jet for the scale of the test facility was varied to simulate the two plant conditions. The TEXAS-V code was used for simulating the phases of premixing and explosion, and the load of a steam explosion was estimated based on the pressure variation. The impulse of a steam explosion under the condition of a corium jet falling into water without a free-fall height is bigger than that under a free-fall height. The fragmented mass of corium in an explosion phase and the distribution of steam fraction are the main parameters for the total load of the steam explosion. This study is expected to contribute to analyses of a steam explosion for a severe accident management strategy.

1. Introduction

The safety of a nuclear power plant is becoming increasingly important over time. The release of radioactive materials has to be prevented for the safety of the public and environment even during a core-melt accident. Immediately after the Fukushima accidents, many countries established a policy for beyond design basis and severe accidents.

Korea enacted a law regarding severe accidents in 2016. It includes the need for an analysis for the factors that can threaten the integrity of the containment after remarkable core damage. A molten fuel-coolant interaction (FCI) was specified as one of the threat factors in the notice. An ex-vessel steam explosion (SE) can occur when a reactor vessel (RV) is broken, and molten-corium falls into the water in the reactor cavity. To show the capability of maintaining the integrity of the containment for the steam explosion, the dynamic pressure from the steam explosion has to be estimated and the structural analysis for the dynamic load on the containment has to be performed.

To resolve the remaining FCI issues for light water reactors, there was a representative international cooperation program of SERENA (Steam Explosion Resolution for Nuclear Applications) in two phases. The scope of the SERENA Phase-1 Program focused on assessing the predictive capabilities of existing tools for reactor cases [1]. The SERENA Phase-1 Program concluded that one variable was not sufficient to explain the level of the loads. In addition, it was emphasized that the uncertainties on a variable distribution in premixing had to be reduced, and the complex effects of variables on steam explosion energetics had to be clarified [1]. The scope of the Phase-2 program focused on resolving the remaining uncertainties through performing complementary analytical work and confirmatory testing [2]. The program also included the reactor calculations defined as the reference cases for a boiling water reactor and a pressurized water reactor. In a comparison with the Phase-1 program, better consistency of most of the results was noticed by various models. The roles of melt fragmentation and solidification, the impact of void on the intensity of an explosion, and

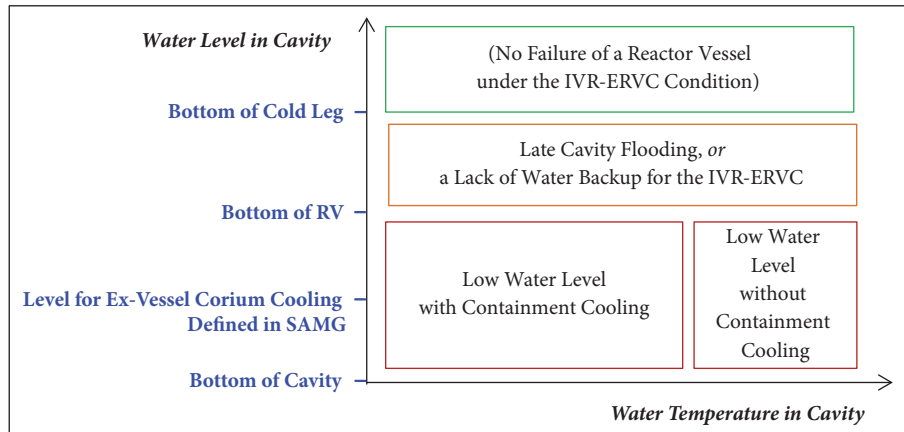


FIGURE 1: Water conditions in cavity and causes of the conditions when a reactor vessel fails.

the triggering mechanisms were emphasized as the major outcomes of the SERENA-2 program [3].

The understanding and knowledge of the overall phenomenon of steam explosion have been discussed and gathered in a recent status report on ex-vessel steam explosion [4]. Technical opinions on the variables of the scenario conditions, phenomenon model parameters, and the main properties were gathered and investigated comprehensively for each importance and status of knowledge. It had been decided by the experts to rank the key phenomena and their possible consequences at a reactor. Jet fragmentation in water, melt droplet characteristics, melt solidification, melt oxidation, fine fragmentation, and stratified configuration have been considered as being important and having medium or insufficient knowledge.

To resolve the relationship between main parameters and a steam explosion load, various researches have recently been carried out in many institutions. Li et al. studied jet breakup length and fragmentation behavior which directly affect the ultimate strength of a steam explosion [5]. The result showed that melt temperature had strong impact on fragmentation that needs to be embodied in advanced fragmentation models. Zhong et al. used a multiphase code with the volume of fluid method to simulate the earlier behavior of droplet when vapor film exited at the phases of triggering and propagation in steam explosion [6]. The paper concluded that vapor film had little effect on the hydrodynamic droplet deformation when the intensity of the pressure pulse was very high.

For an ex-vessel steam explosion load in a typical PWR cavity geometry, Moriyama and Park studied the probability distribution of steam explosion loads in terms of uncertainties in the model parameters and initial conditions [7]. Six uncertainty parameters, the melt inlet diameter and velocity, initial melt temperature, water pool depth, melt droplet diameter during premixing, and the triggering time were chosen and modeled by probability profiles. The loads were strongly correlated with the premixed mass as an intermediate variable, which depended primarily on the melt jet inlet diameter. The water depth showed nearly linear impact on the potential load. Based on the results of the

parametric analyses, a simplified method for evaluation of the steam explosion load was proposed and the results from the proposed method showed fair agreement with JASMINE code [8].

The actual initial conditions of an ex-vessel steam explosion analysis are divided into two kinds according to the procedure in a severe accident management guideline (SAMG) of each plant in Korea. First, in conventional PWRs such as the OPR1000 (Optimized Power Reactor 1000 MWe), the cavity must be filled with water to prevent a containment basemat melt-through by molten-corium concrete interaction in the cavity after a reactor vessel is ruptured. Therefore, there is a reference water level for sufficient ex-vessel coolability of the corium layer. The water is filled to a specific level below the bottom of the reactor vessel. Under this condition, the corium discharged from a reactor vessel falls freely through the air and reaches the surface of the water in the cavity; from here, this is called a “partially flooded cavity condition.” Second, in advanced PWRs such as the APRI400 (Advanced Power Reactor 1400 MWe), AP1000 (Advanced Passive 1000 MWe in Westinghouse), and SMART (System-integrated Modular Advanced Reactor), an IVR-ERVC (in-vessel corium retention through external reactor vessel cooling) strategy is adopted for cooling the corium inside a reactor vessel, resulting in protection of the integrity of a reactor vessel. The strategy is carried out by filling the cavity with water to the level of the cold leg bottom. The reactor vessel is submerged, and heat from the corium is transferred to the water outside the reactor vessel. It is a fully flooded condition in the cavity; from here, this is called a “submerged-RV condition.” Even though the IVR-ERVC strategy has sufficient safety margins after setting the condition, there is a possibility of a failure for performing the strategy. Figure 1 shows the water conditions in the cavity and the causes of the levels and temperatures of the water in the cavity when a reactor vessel fails.

The ex-vessel steam explosion is wholly dependent on cavity water conditions based on the cavity flooding procedures during a severe accident. First, the effect of the corium entry condition has to be considered under partially flooded cavity and submerged-RV conditions. An entering velocity of

a jet into water is related to the fragmentation of a melt jet in water. Second, the effects of the water levels and temperatures have to be considered in terms of a steam explosion. The water level in the cavity is a factor directly determining the amount of corium contributing to the load of a steam explosion. The water temperature is a factor needed to be considered in calculating the void fraction at each water height.

The purpose of this paper is to analyze the effects of the free-fall of corium on a steam explosion by benchmarking previous experimental cases. Two premixing experiments presenting partially flooded cavity conditions and submerged-RV conditions in the TROI (Test for Real corium Interaction with water) facility were modeled by the TEXAS-V code. The experimental results were utilized for validations of the simulations in the premixing phase. Based on the validated results in the premixing phases of the two conditions, the explosion phases were additionally calculated by the TEXAS-V code and analyzed.

2. Analysis Method

2.1. Simulation Code. The TEXAS-V code developed at the University of Wisconsin-Madison was used for simulating a steam explosion [9]. TEXAS-V has transient, three-fluid, and one-dimensional models capable of simulating fuel-coolant mixing interactions [10]. For the vapor and liquid fields of water, there are mass, momentum, and energy equations as the governing equations in the code. For the Lagrangian fuel particle field, momentum and energy equations are included in the code. Three hydraulic fragmentation models are included in the code. They are Rayleigh-Taylor instabilities (RTI), Kelvin-Helmholtz instabilities (KHI), and boundary layer stripping (BLS).

The phases of the premixing, triggering, propagation, and expansion in a steam explosion are simulated by the TEXAS-V code. After the simulation for the premixing of liquid particles and water in a defined period of time, a triggering is assumed to occur at a defined location for the simulation of a steam explosion. In other words, the defined trigger pressure is imposed on the specific water node in the code. The shock wave from the triggering pressure causes the collapse of the vapor film around each fuel particle. The fragmented corium particles are rapidly quenched owing to direct contact with water. It causes the vaporization of water around the particles. The increased amount of vapor increases the local pressure within a very short time. Finally, the increased pressure sustains the shock wave propagation to neighboring regions. The propagation and expansion phases of the steam explosion in the TEXAS-V were modeled based on this continuous process. When a void fraction is larger than the limit constant in a cell of the TEXAS-V, it is regarded that the direct contact area between the fuel particles and water is small. It means less film collapse and vapor generation. Therefore, the fragmentation rate in the propagation phase sharply decreases as a void fraction increases.

Validation of TEXAS-V has been carried out by utilizing experimental programs including FARO, KROTOS, and TROI test facilities. The TEXAS-V computer code was reviewed by the code developers and shown to be quite

capable if simulating the complete vapor explosion process from mixing to the explosion propagation and expansion [11]. Annunziato et al. found that TEXAS application to FARO and KROTOS test cases revealed reasonable prediction capabilities following the optimization of certain input parameters such as heat transfer coefficient for forced convection film boiling for quenching tests and limiting void fraction and fragmentation time for explosion tests [12]. Chen et al. also found that the melt jet leading front position and steam volume during the mixing process predicted by the TEXAS code showed good agreement with the KS-2 and KS-4 experimental data in the KROTOS facility as the coarse mixing status up to the explosion triggering time was well predicted [13]. Song et al. reviewed the capabilities and deficiencies of the fundamental models of the TEXAS-V in terms of their adequacy in a simulation of steam explosion on a reactor scale by evaluating the steam explosion model against the experimental data of KROTOS-44, FARO L-33, TROI-13, and TROI-34 [14, 15]. The experimental cases (TROI-68 and TROI-79) were used to analyze the effects of the free-fall distance on the steam explosion for a subsequent simulation of a reactor case in this paper [16, 17].

2.2. Simulation Conditions. The experiments of TROI carried out in Korea were utilized for analyzing the effects of the water level and free-fall distance on the premixing of the corium particles.

The two experiments presenting partially flooded cavity conditions and submerged-RV conditions were simulated using TEXAS-V, and the results of the experiments and codes were compared. The first experiment (TROI-68) represents the partially flooded cavity condition. Figure 2 shows the TROI facility used to simulate partially flooded reactor cavity conditions. Molten materials are released by gravity with a 1 m free-fall distance between the corium release nozzle and water surface in the test section. This condition indicates that the water level is lower than the level of the reactor vessel bottom. This can take place owing to the insufficient amount of water in carrying out the IVR-ERVC strategy or the original strategy of the ex-vessel corium cooling using the cavity flooding system as a preflooding concept.

The second experiment (TROI-79) represents the submerged-RV condition filling the cavity with the water up to the level of the cold leg. Figure 3 shows the experimental facility for the reactor-submerged conditions. As there is no free-fall of corium, the corium is directly discharged into the water in the test section. It was set for analyzing the effect of no free-fall distance between the release valve and water under the IVR-ERVC condition.

In the two experiments, the main conditions remained the same, excluding the free-fall distance of corium. Table 1 shows the initial test conditions of the TROI-68 and TROI-79. The corium consisted of 80% UO₂ and 20% ZrO₂. The temperature of the corium was tuned to be about 3,000 K. About 20 kg of corium was released to the interaction vessel. 360 kg of water in 341 K was placed in the test section below the corium release nozzle in the two experiments. The test

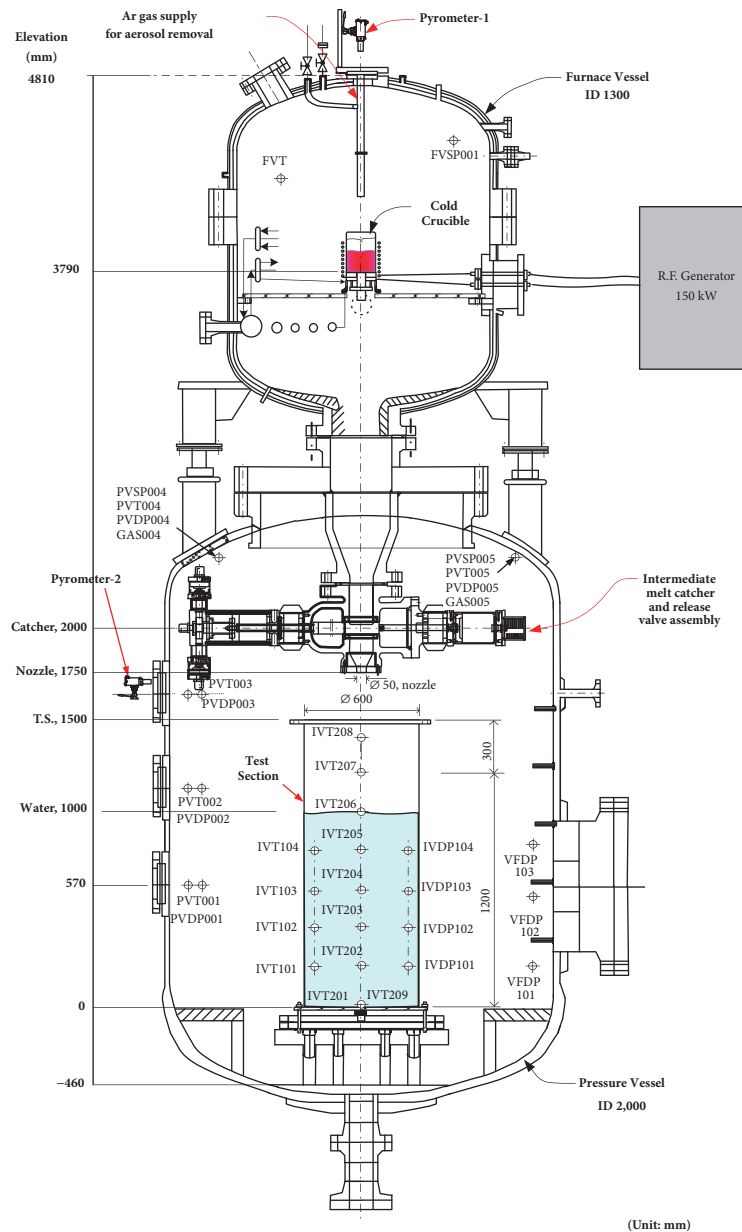


FIGURE 2: Schematics of TROI-68 experimental facility for partially flooded cavity.

section was a square water tank whose height and area were 1.0 m and 0.36 m². The detailed conditions and results of the experiments were described in the previous papers [16, 17]. In the simulations, the code input was set up according to the properties and conditions of the tests.

The results of the premixing phase in the code are compared with the experimental data in the next chapter. Based on the simulation results of the premixing phase, the cases including the explosion phases were simulated to analyze the effects of corium entry condition on the impulse of the steam explosion. The main phenomenon parameters in the sensitivity analyses are explained in Table 2. The values used for the reference case and the values in each case of sensitivity analysis are specified. The sensitivity analyses for

the premixing phases in the two experimental cases are done and explained in each subchapter.

3. Simulations for Premixing Phase

3.1. Partially Flooded Cavity Condition. First, the TROI-68 experiment for the partially flooded cavity condition is simulated by the code.

Location variations of the melt jet leading front in the condition for a partially flooded cavity are shown in Figure 4. In the TROI experiment, thermocouples were installed along the centerline of the test section for detecting the location of the melt front with time. The red-filled circles were marked in Figure 4 at each midpoint where the detected temperature

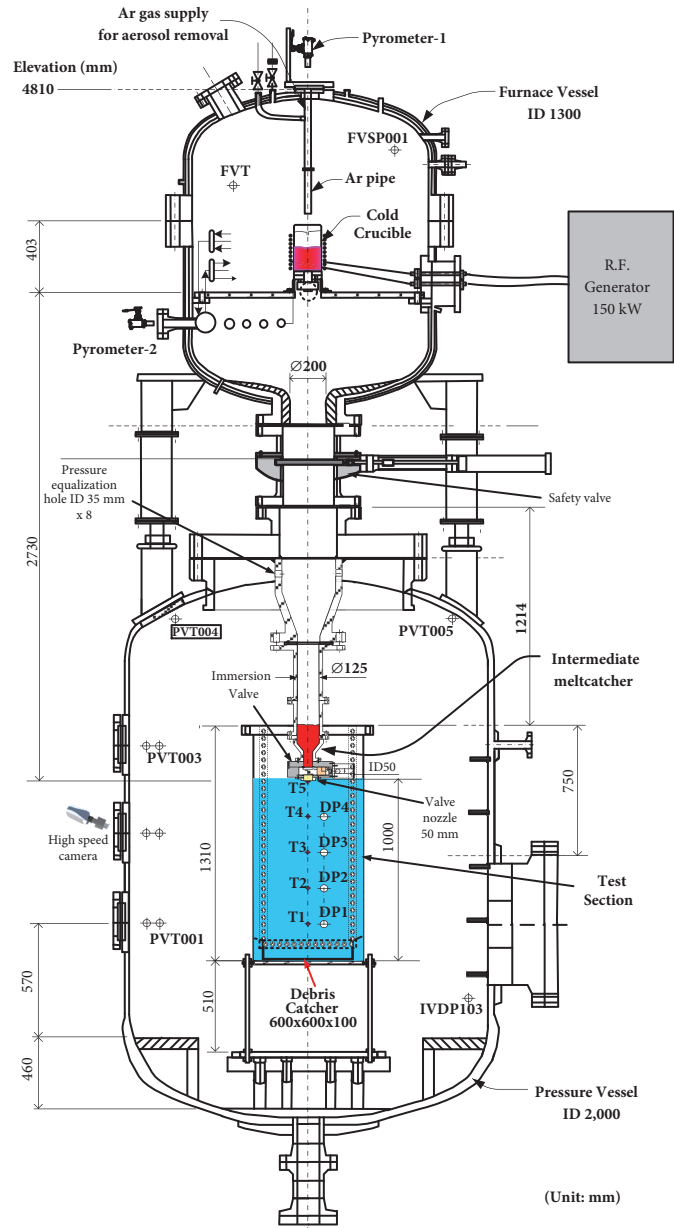


FIGURE 3: Schematics of TROI-79 experimental facility for submerged-RV.

sharply increased. In addition, as the side section of this experiment was recorded by a video camera, the location of the melt front could be observed in one direction. The results observed through the camera were marked with blue-filled squares. In the TEXAS-V simulation, the initial melt velocity at the intermediate nozzle was set to be almost zero. Owing to the acceleration through a 1 m free-fall, the entering velocity of the melt jet was 4.35 m/s at the water level. In both the experiment and simulation, the strong fragmentation from Rayleigh-Taylor instability caused by the high velocity of the melt jet resulted in the sharp decrease of the jet velocity during 0.3 s after entering the water.

A sensitivity analysis for the parameters of the premixing phase in the TEXAS-V code was performed. Figure 5 shows

the main results of the sensitivity analyses. The relative convergence criteria for liquid and gas mass equations were first checked and there was no change in the calculation results. When the coherent jet entry model with a trailing edge was applied, the melt jet and free particles were regarded to be independent of each other for fragmentation in a mesh cell. As the frontal part of the melt jet was continuously fragmented, the time for reaching the bottom was delayed. When the coherent jet entry model with a leading edge was applied, the melt jet front was fragmented by taking over the free particles. In the reference case, the fragmentation was modeled using RTI, KHI, and BLS. There was no big difference in the melt jet front location in the premixing phase when the initial and minimal bubble and droplet radius and

TABLE 1: Initial conditions in TROI tests.

| | TROI-68 | TROI-79 |
|---|--------------|-------------------------|
| Melt | | |
| UO ₂ /ZrO ₂ (wt%) | 80:20 | 80:20 |
| Temperature (maximum) (K) | 2990 | 3015 |
| Charged mass (kg) | 29.58 | 34.30 |
| Released mass (kg) | 19.18 | 22.54 |
| Plug/puncher diameter (cm) | 10.0 / 8.5 | 10.0 / 8.5 |
| Jet diameter (cm) | 5.0 (nozzle) | 5.0 (nozzle) |
| Nozzle-to-water surface distance (m) | 1 | -0.01 (below the water) |
| Test section | | |
| Water mass (kg) | 360 | 360 |
| Water pool depth (cm) | 100 | 100 |
| Cross section (m ²) | 0.36 | 0.36 |
| Initial temperature (K) | 341 | 341 |
| Pressure vessel | | |
| Initial pressure (air) (MPa) | 0.205 | 0.125 |
| Initial temperature (K) | 307 | 311 |

TABLE 2: Cases and parameters in sensitivity analysis.

| Name of Case | Description for Parameter in Sensitivity Analysis | Reference Value | Value in Sensitivity Analysis |
|---------------|---|--|---|
| REF | (Reference case) | - | - |
| Trailing Edge | Particle injection mode & break-up model flag | RTI, KHI, BLS | coherent jet entry model with trailing edge |
| Leading Edge | Particle injection mode & break-up model flag | RTI, KHI, BLS | coherent jet entry model with leading edge |
| NB-# | The Number of leading particles | 4.0 (Partially Flooded case), 1.0 (Submerged-RV case) | 1.0 – 5.0 |

KHI coefficient changed. As the number of leading particles increased, the time for reaching the bottom was delayed owing to the fragmentation on each particle being regarded as independent.

In the TROI experimental facility, four K-type thermocouples were installed to measure the water temperature at heights of 0.2, 0.4, 0.6, and 0.8 m on the side wall of the test section. When the melt jet front reached the bottom of the test section, the temperature of the water rose by about 1.0 K at the 0.4 and 0.6 m thermocouples in the experiment. On the other hand, the temperature of the water rose by 2.0 K in the code. It is the averaged value in the cell as the TEXAS-V is a one-dimensional code. Even though the center of the cell is highly heated owing to the fragmented corium particles, the heat is transferred to the whole water inside the cell. In Figure 6, the similar tendency of void fractions is shown in the TROI experiment and TEXAS-V simulation. Many small bubbles around the fragmented corium particles were observed in the experiment. The void fractions increased due to the increase of the total heat transfer area between melt particles and water by the fragmentation of the melt particles. At the time the corium reached the bottom, the void fraction in the center of the water was 0.20 in the TROI experiment and 0.24 in the TEXAS-V code. The distribution of void fractions in

the premixing phase plays a significant role in the thermal fragmentation in the propagation phase.

3.2. Submerged-RV Condition. Second, the TROI-79 experiment for the submerged-RV condition is simulated by the code.

Location variations of the melt jet leading front in the condition for submerged-RV condition are shown in Figure 7 with the results of a sensitivity analysis. In the TROI experimental facility, five thermocouples were installed at each height of the test section for detecting the location of melt jet front and measuring the velocity. There were 26 thermocouples in total. The red circles with the bars were marked by the first one, which showed the earliest temperature increase among the five thermocouples. The error bars represented the start and end of the temperature increase in the thermocouple. In the TEXAS-V simulation, the initial melt velocity at the intermediate nozzle was assumed to be the same as in the simulation for the partially flooded cavity condition.

In the sensitivity analysis, there was no difference in the results from the change of the calculation criterion of the code. The options for the fragmentation models did not affect

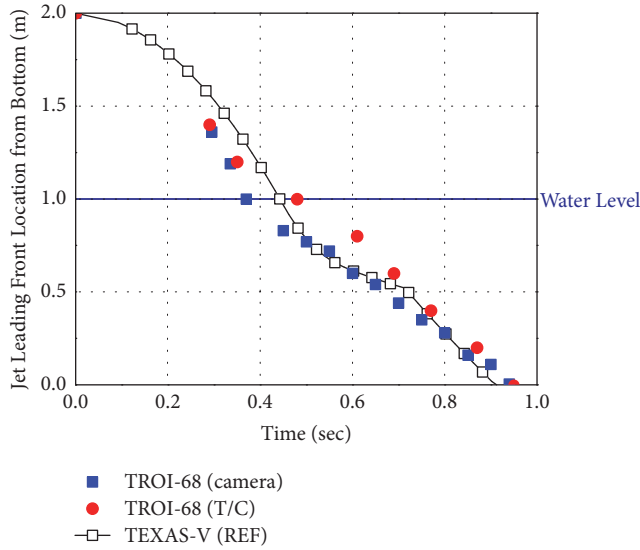


FIGURE 4: Locations of melt jet leading front in TROI experiment and TEXAS-V simulation for the partially flooded cavity condition.

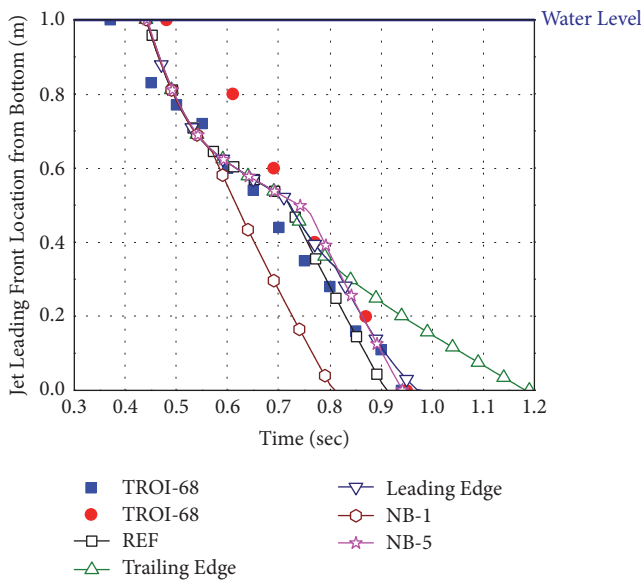


FIGURE 5: Results of sensitivity analysis for melt particle locations in partially flooded cavity condition.

the variations of the melt front locations. This is because the melt front was ahead of the free particles and fragmented during the total simulation time. In the reference case, the initially scattered particles not shown in the experiment were not simulated, unlike the case for the partially flooded cavity.

In the TROI experimental facility, four K-type thermocouples were installed to measure the water temperature at heights of 0.2, 0.4, 0.6, and 0.8 m in the test section. When the melt jet front reached the bottom of the test section (0.5 s), the increase in water temperature was 0.2 to 1.0 K in the thermocouples. Measurement of the small increase involved high uncertainty owing to the fluctuation of the detection during a short time. About 0.4 K of the

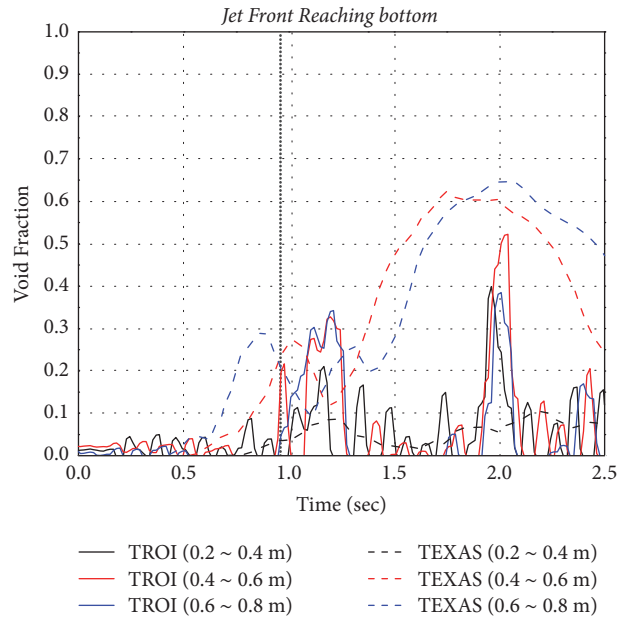


FIGURE 6: Void fractions in TROI experiment and TEXAS-V simulation for the partially flooded cavity condition.

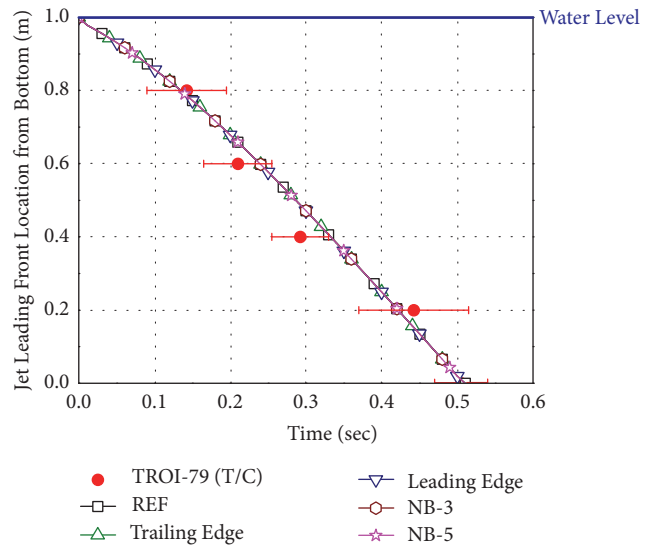


FIGURE 7: Locations of melt jet leading front in TROI experiment and TEXAS-V simulation for the submerged-RV condition with the results of sensitivity analysis.

water temperature increased at 0.5 s in the simulation. After 1.0 s from the start, about 2.0 K of water temperature increased in both the experiment and simulations owing to the continuous injection of corium into water. Figure 8 shows void fractions in the experiment and TEXAS-V simulation. The void fractions at 0.5 s were not different with the initial values in the experiment. The void fractions slightly increased in the simulation. Due to the small inertia force caused by the small initial velocity, the melt jet gradually accelerated and fell through the water as a lump. A thick vapor film around

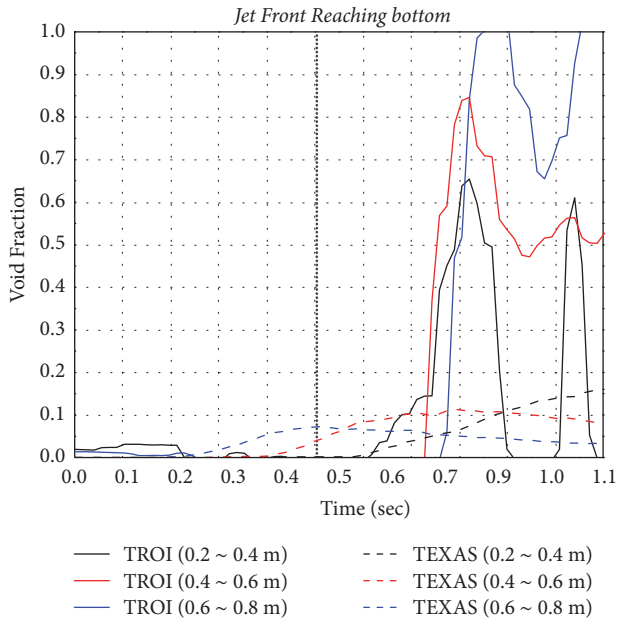


FIGURE 8: Void fractions in TROI experiment and TEXAS-V simulation for the submerged-RV condition.

the melt stream was observed in the TROI experiment. In addition, because major large steam bubbles were released over the surface of water along the stream of the melt jet in the water, the void fractions were kept low before the bottom impingement of the melt jet. At the time the jet front reached the bottom, the void fraction in the center of the water was 0.0 in the TROI experiment and 0.04 in the TEXAS-V code. After the bottom impingement of the melt jet, void fractions sharply increased at all detected points in the experiments. After 1 s from the injection of the corium, the void fraction in the center of the water was 0.52 in the experiment and 0.09 in the simulation. As the bottom impingement of the corium jet resulting in strong fragmentation was not modeled in the TEXAS-V and the weak fragmentation acted on the large particles through the water, the temperature increase of water was small, and the void fractions were kept low. This does not have any significant effect on the explosion phase owing to the assumption for the bottom contact triggering in the next chapter. For the simulation of the explosion phase, the premixing simulation finishes at the time the melt particles reach the bottom.

3.3. Comparison of Two Conditions. The simulation results for the TROI-68 and TROI-79 are compared below.

A similar tendency in the experiment and simulation for each condition is shown in the previous subchapters. The velocities at which the melt jets enter the water and the average velocities during falling through water under the two conditions are shown in Figure 9. The melt jet was accelerated during a free-fall height of 1 m in the partially flooded cavity condition. The melt jet was almost stopped in the intermediate valve and directly fell into the water. However, it took about 0.5 s for both melt jets to reach the

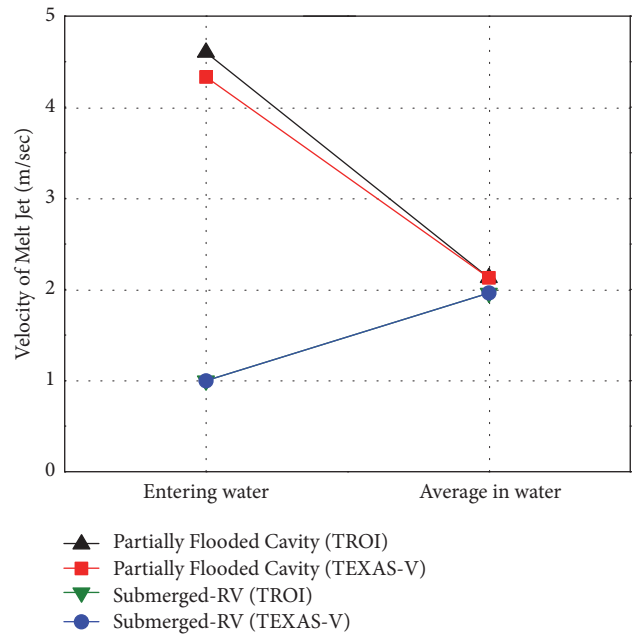


FIGURE 9: Velocities of melt front in experiments and simulations.

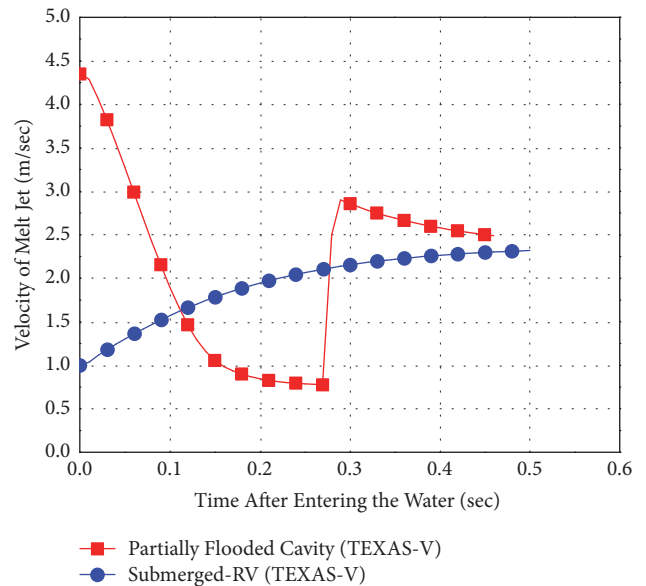


FIGURE 10: Variation of velocity of melt front through water in TEXAS-V simulation.

bottom of the water test section. This means one average velocity in the water is similar to the other. As shown in Figure 10, the melt front and the scattered free particles in the partially flooded cavity condition were fragmented from the top of the water. At 0.27 s, the following corium particle overtook the leading edge of the melt jet and started to be fragmented again. The velocity of the melt in the submerged-RV condition gradually increased in the water, as shown in Figure 10. A weak instability at the leading edge resulted in a slow decrease in acceleration. The side of the melt jet was fragmented continuously owing to the KHI.

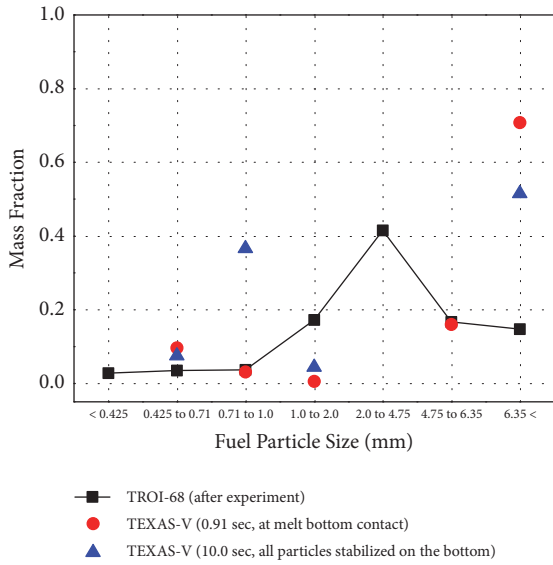


FIGURE 11: Particle size distribution in the condition for partially flooded cavity.

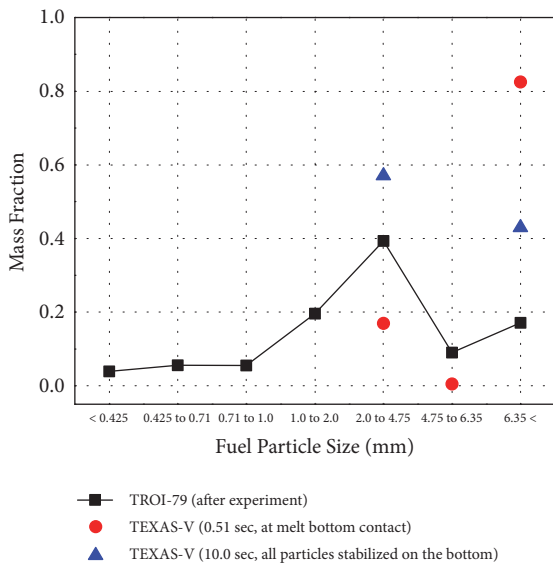


FIGURE 12: Particle size distribution in the condition for submerged-RV.

Particle size distributions under the two conditions are displayed in Figures 11 and 12. The black lines indicate the data from the TROI experiments. After performing the experiment, the debris accumulated at the bottom of the test section was collected for a postdebris analysis. Then, the debris was sieved and weighed for analyzing the particle size distribution. When comparing the experimental data in TROI-68 and TROI-79, no significant difference appeared. The fractions of the corium particle sizes in the two experiments were high in 2.0 to 4.75 mm. Red dots represent the size distribution when the melt jet reaches the bottom of the water test section during the simulations. These data at this point are used as the initial size distribution in the

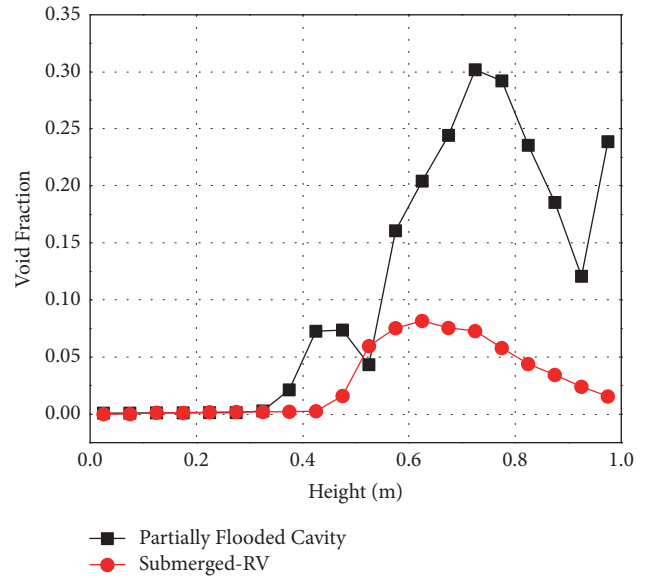


FIGURE 13: Axial distribution of void fraction at the triggering time in both cases.

simulation of the propagation phase of a steam explosion. The melt front and free particles in the partially flooded cavity condition were fragmented into much smaller sizes than those in the submerged-RV condition. Blue dots represent the size distribution of the corium particles accumulated at the bottom after the injection of all of the corium. Compared with the red dots, the portion of fragmented particles increased. The portion of particles whose size is smaller than 1.0 mm was high in the partially flooded cavity condition, while it did not appear in the submerged-RV condition. The inconsistency in the results between the experiments and the simulations at the end of the test was induced by the effect of the bottom impingement. All particles were fragmented again owing to the bottom impingement in the experiments. Even though more fragmented particles were observed before the time of melt bottom contact in the partially flooded cavity condition than in the submerged-RV condition, the similar size distributions in the two experiments were gathered by sieving the particles after the tests. These were shown in Figures 11 and 12. However, all the particles stopped at the bottom in the simulations when they reached the bottom. The fragmentation from the physical collision on the bottom was not included in the modeling of the simulations.

The axial distributions of the void fractions at the triggering times in both cases are shown in Figure 13. There were more fragmented particles in the partially flooded condition than in the submerged-RV condition as shown in the experiments and simulations. In the experiment for the partially flooded condition, more small bubbles around the corium particles were observed. The more the corium particles were fragmented into smaller particles in the TEXAS-V simulation, the more the heat transfer area between the corium particles and water increased. This caused more vaporization of water on each surface of the corium particles. On the other hand, a thick film was formed around the

surface of the melt jet under the submerged-RV condition because the melt jet stream fell into the bottom as a lump. The heat area between the corium and water in the submerged-RV condition was smaller than that in the partially flooded condition.

The variations in temperatures were not significantly shown in the results of the experiments. This can also be explained by the temperature increase of water. During the same premixing time between the melt jet and water in the two simulation cases, the temperature in the case of the partially flooded condition increased more than that in the case of the submerged-RV condition.

4. Simulations for Explosion Phase

The phases of triggering, propagation, and expansion are simulated by the TEXAS-V code based on the results of the premixing phase under the conditions of a partially flooded cavity and submerged-RV. The occurrence of the bottom triggering is assumed for simulating an ex-vessel steam explosion in a reactor cavity. Therefore, when the lowest melt particle reaches the bottom of the water test section, the calculation for the premixing phase is set to be finished. Accordingly, the defined trigger pressure is imposed on the lowest water cell in the code. The fine fragmentation rate during the explosion phase was calculated in each cell of the TEXAS-V. The void fraction and dynamic pressure were calculated under the assumption that water around each fuel particle was vaporized within a very short time of the propagation phase.

The explosion processes for the conditions of the partially flooded cavity and the submerged-RV were calculated on the basis of the premixing results described in the previous chapter. To analyze the effects of corium entry condition, only the location of the corium injection, which varied the jet velocity at the water level, was changed in the two cases.

The pressure variations calculated at the bottom of the water test section under both conditions are shown in Figure 14. The pressure peak under the partially flooded cavity condition was higher and narrower than that in the submerged-RV condition. As the independent leading particles in the partially flooded cavity condition were strongly fragmented and located at the center of the water at the time of the triggering, the bigger pressure wave was generated and propagated from the center cell. Compared with that, the particle distribution in the submerged-RV condition was quite uniform throughout the water.

The impulse is defined by integrating the calculated dynamic pressure for each time. Under the assumption that a total water above the triggering point is accelerated by a steam explosion upward in one dimension, the water velocity is calculated by a total mass of water. Finally, the kinetic energy converted from the total thermal energy of the melt can be estimated by the water mass and velocity pushed out based on the calculation method proposed in the previous study [18]. The kinetic energy calculated from the pressure variation of the steam explosion is plotted in Figure 15. The kinetic energy in the partially flooded cavity condition was 75.1 kJ, and that

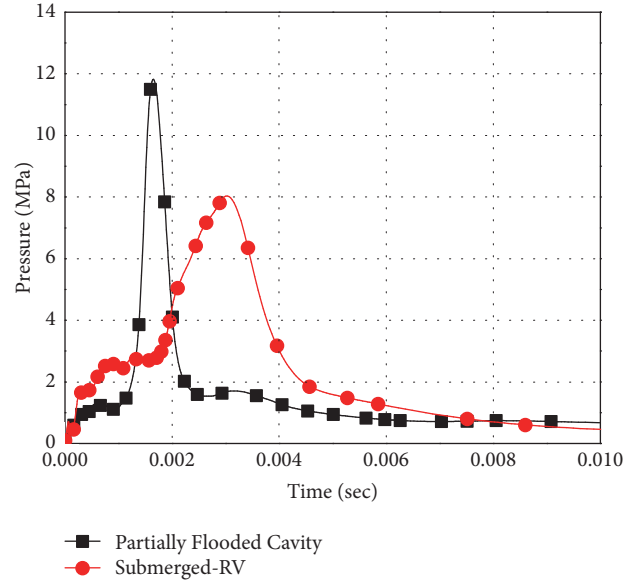


FIGURE 14: Maximum pressure calculated at the bottom of the water tank in both cases.

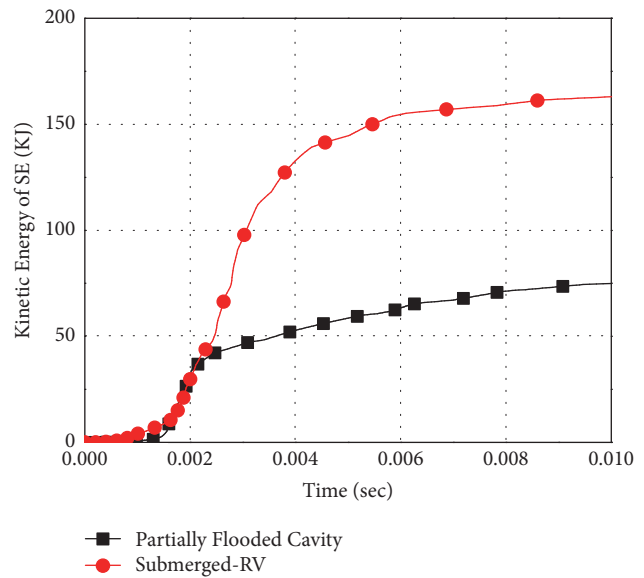


FIGURE 15: Kinetic energy calculated from the impulse of steam explosion at the bottom of the water tank in both cases.

in the submerged-RV condition was 163.0 kJ. There are two main reasons for the difference between the two values.

Firstly, a larger mass of corium was involved in calculating the total load of the steam explosion in the submerged-RV case than in the partially flooded cavity case. Figure 16 shows the finely fragmented melt mass during the propagation and expansion phases in both cases. Comparing the particle size distributions at the time of triggering shown in Figures 11 and 12, the mass fraction of particles larger than 6.35 mm in the submerged-RV case was higher than that in the partially flooded case. The mass fraction of the melt jet under water was 52.2 % in the partially flooded case, and that was 74.7

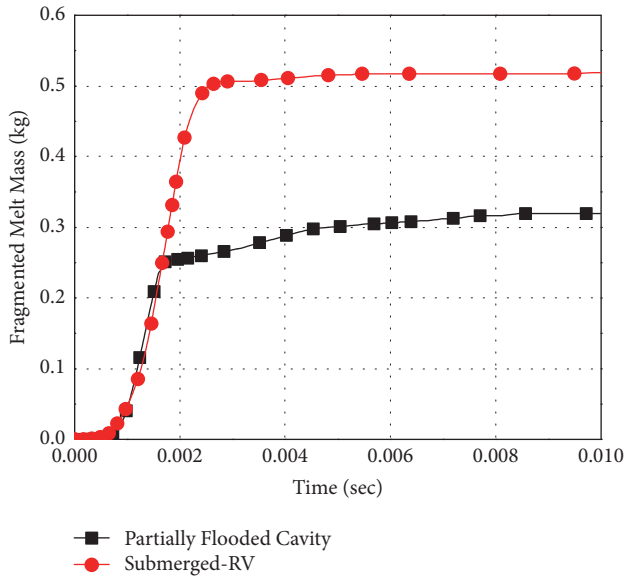


FIGURE 16: Finely fragmented melt mass during steam explosion in both cases.

% in the submerged-RV case. However, it was found that the mass mean diameter of melt particles at the end of the explosion was 1.0 mm in the partially flooded case, and that was 1.9 mm in the submerged-RV case. Therefore, the total mass of the melt particles, which were finely fragmented in the propagation phase in the submerged-RV case, was bigger than that in the partially flooded cavity. Owing to the continuous propagation of pressure wave during the sufficiently long propagation time, the surfaces of large particles were fragmented into fine particles. Vapor films formed around the finely fragmented particles resulted in the large conversion ratio of the thermal energy to the kinetic energy.

Secondly, void fractions in the partially flooded cavity case were higher than those in the submerged-RV case, as shown in Figure 13. The void fractions at higher positions than 0.55 m in the partially flooded cavity case were higher than those in the submerged-RV case and close to 0.3. When the flow regime changes from a bubbly flow to a slug or droplet flow, the surfaces of corium particles are covered by steam and the direct contact area between corium particles and liquid water decreases significantly. Less vaporization of liquid water by melt particles results in less fragmentation rate in the propagation phase. In the TEXAS-V, a range of the void fraction for the bubbly flow regime is defined. When the void fraction in a fluid cell is higher than the defined value, the generation of steam sharply decreases in the propagation phase. Under partially flooded cavity conditions, the void fractions rose owing to the heat transfer between the fragmented particles and water in the premixing phase. Because there were fewer small fragmented particles in the submerged-RV condition, the temperature and void fraction have risen to a limited extent before the melt bottom contact.

Based on the calculation method proposed by Hong et al., the conversion ratio was calculated by the total thermal energy of the melt under water and the kinetic energy from

the steam explosion [18]. The conversion ratio in the partially flooded case is 0.3% and that in the submerged-RV case is 1.0%. Even though a steam explosion is intentionally triggered regardless of the particle size distribution, and the pressure wave from the triggered cell is propagated well to adjacent cells in a one-dimensional code, the conversion ratio in the submerged-RV case is larger than the general value.

5. Conclusions

The reactor cavity of a nuclear power plant may or may not be filled with water at the time of a severe accident according to a severe accident management guideline or the accident conditions. The effects of a free-fall of corium on steam explosion were investigated in this paper. The two premixing experimental tests were simulated by the TEXAS-V code for benchmarking purposes. Based on the results of the premixing phase, the explosion phases in the two cases were simulated. A larger impulse of a steam explosion in the submerged-RV case was calculated than in the partially flooded case. There are two main reasons for this. First, more mass of corium was involved in the submerged-RV case. When a corium jet fell into water without a free-fall height, a weaker inertial force caused a smaller fragmented force in the premixing phase, compared with the case of a partially flooded cavity with a free-fall height. Larger pressure loads were calculated owing to the large sized particles fragmented during the sufficiently long propagation time. Second, as the melt jet fell through water as a lump in the case of the submerged-RV, less steam was produced than in the case of the partially flooded cavity. The distribution of void fractions was similar in both the experiments and simulations. The effect of a large bubble around a melt jet is an important element to be simulated well.

In general, the distribution of smaller corium particles results in a larger impulse of a steam explosion owing to the larger contact area between the corium and water at the end of the premixing phase. However, it was found that the impulse of a steam explosion can be larger in spite of the distribution of larger corium particles when the pressure wave is propagated well in the uniform distribution of corium particles and the low overall void fractions of water.

To analyze the actual plant conditions, the water level and temperature have to be varied in the simulations for the steam explosion. The increase in the water level will result in an increase in the corium mass involved in the explosion. However, it also implies that more particles are fragmented and solidified as the water level increases. In addition, the increase in the initial water temperature will act as a limiting value for the fragmentation during the propagation phase. However, under actual submerged-RV conditions, the water temperature can be stratified if the height of the cavity is high. The water temperature around the bottom of the reactor vessel is saturated owing to the heat transfer from the inside of the reactor vessel. On the other hand, the water temperature in the lower part of the cavity will be lower than the saturation temperature in the initial state. This can cause a larger impulse of the steam explosion owing to the low rate of solidification

of corium particles in the higher part and very low void fraction in the lower part where a steam explosion occurs.

Two steam explosion tests which were carried out with the external triggering in the same TROI facility for the conditions of partially flooded cavity and submerged-RV will be analyzed as a further study of this paper.

Data Availability

The data used to support the findings of this study are available from the corresponding author upon request.

Conflicts of Interest

The authors declare that there are no conflicts of interest regarding the publication of this paper.

Acknowledgments

This work was supported by the National Research Foundation of Korea (NRF) grant funded by the Korea government (Ministry of Science and ICT; Grant no. 2016M2C6A1004893).

References

- [1] OECD/NEA, OECD Research Programme on Fuel-Coolant Interaction Steam Explosion Resolution for Nuclear Applications - SERENA, Final Report - December 2006, NEA/CSNI/R(2007)11, 2007.
- [2] OECD/NEA, OECD/SERENA Integrated Report (Steam Explosion Resolution for Nuclear Applications), 2014.
- [3] R. Meignen, B. Raverdy, M. Buck et al., "Status of steam explosion understanding and modelling," *Annals of Nuclear Energy*, vol. 74, no. C, pp. 125–133, 2014.
- [4] OECD/NEA, Status Report on Ex-Vessel Steam Explosion: EVSE, OECD/NEA /CSNI/R(2017)15, March, 2018.
- [5] Y. Li, Z. Wang, M. Lin, M. Zhong, Y. Zhou, and Y. Yang, "Experimental Studies on Breakup and Fragmentation Behavior of Molten Tin and Coolant Interaction," *Science and Technology of Nuclear Installations*, vol. 2017, 14 pages, 2017.
- [6] M. Zhong, Y. Li, M. Lin, M. Yuan, and Y. Yang, "A Numerical Analysis Research on Earlier Behavior of Molten Droplet Covered with Vapor Film at the Stage of Triggering and Propagation in Steam Explosion," *Science and Technology of Nuclear Installations*, vol. 2014, 10 pages, 2014.
- [7] K. Moriyama and H. S. Park, "Probability distribution of ex-vessel steam explosion loads considering influences of water level and trigger timing," *Nuclear Engineering and Design*, vol. 293, pp. 292–303, 2015.
- [8] K. Moriyama and H. S. Park, "Parameter dependence of steam explosion loads and proposal of a simple evaluation method," *Nuclear Engineering and Technology*, vol. 47, no. 7, pp. 907–914, 2015.
- [9] M. L. Corradini et al., *User's Manual for TEXAS: One Dimensional Transient Fluid Model for Fuel-Coolant Interaction Analysis*, University of Wisconsin, Madison, Wis, USA, 2012.
- [10] J. Tang, *Modeling of the Complete Process of One-Dimensional Vapor Explosions [Thesis paper]*, 1993.
- [11] M. L. Corradini et al., *Fuel-Coolant Interaction Analyses with TEXAS-V Vapor Explosion Model*, University of Wisconsin, Madison, Wis, USA, 1999.
- [12] A. Annunziato, A. Yerkess, and C. Addabbo, "FARO and KROTOS code simulation and analysis at JRC Ispra," *Nuclear Engineering and Design*, vol. 189, no. 1-3, pp. 359–378, 1999.
- [13] R. Chen, J. Wang, G. H. Su, S. Qiu, and M. L. Corradini, "Analysis of KROTOS KS-2 and KS-4 steam explosion experiments with TEXAS-VI," *Nuclear Engineering and Design*, vol. 309, pp. 104–112, 2016.
- [14] H. J. Song, I. Park, and J. H. Kim, "A Coherent Methodology for the Evaluation of a Steam Explosion Load Using TEXAS-V," *Journal of the Korean Nuclear Society*, vol. 6, no. 36, pp. 571–581, 2004.
- [15] KAERI, "The Coherent Evaluation of the Steam Explosion Load by Using TEXAS-V," Korea Atomic Energy Research Institute, KAERI/TR-3066/2005, 2005.
- [16] S. W. Hong, Y. S. Na, S. H. Hong, and J. H. Song, "Fuel-coolant interaction test results under different cavity conditions," *Nuclear Technology*, vol. 196, no. 3, pp. 538–552, 2016.
- [17] Y. S. Na, S.-H. Hong, J. H. Song, and S.-W. Hong, "Fuel-Coolant Interaction Visualization Test for In-Vessel Corium Retention External Reactor Vessel Cooling (IVR-ERVC) Condition," *Nuclear Engineering and Technology*, vol. 48, no. 6, pp. 1330–1337, 2016.
- [18] S. W. Hong, "Conversion ratio of molten corium in TROI steam explosion experiment," in *Proceedings of the Transactions of the Korean Nuclear Society Spring Meeting*, Jeju, Korea, 2017.